

Experimental research of pore water pressure fluctuation on the stability of submarine slopes

A case study of the Eastern Scheldt storm surge barrier

Florentine Steijlen



Experimental research of pore water pressure fluctuation on the stability of submarine slopes

A case study of the Eastern Scheldt storm surge barrier

by

F. G. H. Steijlen

to obtain the degree of Master of Science
at the Delft University of Technology.
to be defended publicly on Monday December 16, 2019 at 16:00 PM.

Student number:	4282337
Project duration:	December 10, 2018 – December 16, 2019
Chair committee:	Dr. A. Askarinejad Delft University of Technology
Committee members:	Prof. dr. ir. M.A. Hicks Delft University of Technology
	Dr. ir. R.J. Labeur Delft University of Technology
	A. Maghsoudloo Delft University of Technology
	Ir. J.P.F.M. Janssen Rijkswaterstaat
	Ir. S.G. van den Berg Rijkswaterstaat

An electronic version of this thesis is available at <http://repository.tudelft.nl/>.

Summary

Liquefaction is a failure mechanism of a sudden loss of shear strength. Such loss is caused by the development of excess pore water pressure that reduces the effective stress to zero. The occurrence of liquefaction is preceded by instability, which occurs when the soil cannot hold the current stress state anymore. Liquefaction is a common hazard in submarine slopes. Three conditions are required to cause a liquefaction flow slide: the presence of a soil type that is susceptible to liquefaction, the presence of a critical slope geometry and an initiation mechanism.

Liquefaction slope failures are observed at the scour hole slopes that have been formed near the bed protection layer of the Eastern Scheldt barrier. The soil investigation data in this area verify the presence of soil that is susceptible to liquefaction. Furthermore, the bathymetry exposes the presence of scour holes that are relatively deep with steep slopes. Thus, two conditions to cause liquefaction slope failures are met. However, the initiation mechanism of these failures is unknown. It is expected that the turbulent water flow near the barrier plays a role in initiating liquefaction and that this flow leads to water pressure fluctuations at the bed. To confirm these expectations, insight into the coupled processes of morphology, hydraulics and geotechnics is a prerequisite.

This study aims to improve the understanding of the liquefaction initiation mechanism near the Eastern Scheldt barrier. Triaxial element tests are performed to investigate the influence of water pressure fluctuation, generated by the water flow, on the soil response. These tests represent one critical point located close to the toe and the sloping bed of a slope near the barrier. The selection of this point is based on the proximity of the stress state to the critical state line, which is determined by a Plaxis 2D finite element model. The same model is used to obtain the stress conditions for the triaxial tests consisting of a loading and unloading phase that represent the sedimentation and scouring respectively.

A second model is used to investigate the excess pore water pressure development of the selected point due to water pressure change at the bed. Multiple combinations of amplitude and frequency of the water pressure change at the bed are applied based on the ADCP (acoustic doppler current profiler) velocity data. The rate of excess pore water pressure increases with an increase in amplitude and an increase in frequency. The maximum rates of the excess pore water pressure increases are applied to the triaxial tests.

After applying the simulation of the sedimentation and scouring on the triaxial samples, the water flow above the bed is simulated by increasing the back pressure with the pre-selected maximum rates while keeping the axial load and cell pressure constant. The test results showed that the start of the decrease in deviatoric stress is earlier in time and at lower stress ratios for higher back pressure rates. Therefore, the stress ratio of the instability of the soil is expected to be lower for higher back pressure rates. Based on the axial strain data, it can be concluded that the exact point of instability cannot be defined with the triaxial setup in this research, because the displacements are slowed down due to the reduction of axial load. All in all, it is expected that the liquefaction flow slides are initiated at the lower part of the slope and that the flow velocity is influencing the stability of the soil. All in all, this research brings us a step closer to the understanding of the initiation mechanism of the liquefaction slope failures close to the Eastern Scheldt barrier.

Preface

During summer my family often stays a couple of days in the area of the Eastern Scheldt barrier. When I heard about the scour hole formation and liquefaction near the barrier by Arash, my interest in the stability of the barrier has grown stronger. Therefore, I was happy that Amin Askarinejad and Arash Maghsoudloo still had room for another master thesis project. I learned a lot during my master thesis and therefore I would like to thank all the people who supported me. First of all, I would like to thank Amin and Arash for the weekly meetings and advice. Thanks, Arash for explaining me how the triaxial setup works and for answering all my questions.

Thanks, Hans Janssen and Stefan van den Berg for introducing me to Rijkswaterstaat and helping me to think practical. Robert Jan Labeur, thank you for pointing me on the complexity of fluid mechanics and helping me with the structure of my thesis. Michael Hicks thanks for your attendance during the meetings.

I would like to thank my family and friends. Especially my sister, Annemarijn, thanks for the crash course Adobe Illustrator and your advice. Last but not least, Jeroen, thanks for reminding me that there are other things than my graduation thesis.

Florentine Steijlen
December 6, 2019

List of Figures

- 1.1 Satellite image of the Eastern Scheld storm surge barrier 5
- 1.2 Cross-sections Roompot East 2007-2019 parallel to the barrier 7
- 1.3 An overview of the report structure with the chapters and corresponding sub-questions 8

- 2.1 Borehole near the scour hole at Roompot East 12
- 2.2 Location of the cone penetration test, the boring, the density measurements and sampling for sieving at Roompot East 12
- 2.3 Grain size diagram for samples at the edge of the bed protection layer close to the deepest point of the scour hole 14
- 2.4 Bathymetry map of Roompot East of August 2018 (Google Earth Pro 7.3.2, 2019) 15
- 2.5 Cross-sections parallel and perpendicular to the barrier, through the deepest point at Roompot East in August 2018 16
- 2.6 The ADCP measurement locations on a cross-section at Roompot East 19
- 2.7 Depth-averaged velocity and water level at the deepest measurement point 19

- 3.1 Laboratory sand grain size distribution 22
- 3.2 Triaxial testing equipment 22
- 3.3 Triaxial test sample under vacuum 23
- 3.4 Pictures of consolidated soil samples at the end of the drained triaxial compression tests 24
- 3.5 Consolidated drained triaxial test results: normalised deviatoric stress versus axial strain 25
- 3.6 Consolidated drained triaxial test results: volumetric strain versus axial strain . . 25
- 3.7 Consolidated undrained triaxial test results: deviatoric stress versus mean effective stress 26
- 3.8 Consolidated undrained triaxial test results: excess pore water pressure versus axial strain 27
- 3.9 Consolidated undrained triaxial test results: normalised deviatoric stress versus axial strain 27
- 3.10 Consolidated drained triaxial test results: effective stress path and critical state line 28
- 3.11 Consolidated undrained triaxial test results: effective stress path and critical state line 28

- 4.1 Schematic picture of the model 1 phases for a slope with a 1:5 ratio 30
- 4.2 Consolidated drained triaxial test results and the determination of E^{50} 32
- 4.3 Deviatoric stress versus axial strain graphs of the experimental and Hardening Soil model consolidated drained triaxial test results with an effective confining pressure of 150 kPa 33
- 4.4 Volumetric strain versus axial strain graphs of the experimental and Hardening Soil model consolidated drained triaxial test results with an effective confining pressure of 150 kPa 34

LIST OF FIGURES

4.5	Deviatoric stress versus axial strain graphs of the experimental and Hardening Soil model consolidated drained triaxial test results with an effective confining pressure of 100 kPa	34
4.6	Volumetric strain versus axial strain graphs of the experimental and Hardening Soil model consolidated drained triaxial test results with an effective confining pressure of 100 kPa	34
4.7	Mohr circle with mobilised shear stress (τ_{mob}), maximum shear stress (τ_{max}) and Mohr-Coulomb failure line	35
4.8	Relative shear stress of model 1 for slope 1:5	36
4.9	Stress points along the slope at approximately 1 meter below the bed	37
4.10	Stress state of the selected stress points at 1 meter below the bed in a deviatoric stress versus mean effective stress plane	37
4.11	Relative shear stress for a slope geometry of 1:5, 1:3, and 1:2	38
4.12	Stress state of the selected stress points at 1 meter below the bed for slope 1:5, 1:3 and 1:2 in a deviatoric stress versus mean effective stress plane	39
4.13	Schematic picture of the model 2 phases	43
4.14	Pore water pressure versus axial strain graphs of the experimental and UBC3D-PLM model consolidated undrained triaxial test results with an effective confining pressure of 200 kPa	46
4.15	Pore water pressure versus axial strain graphs of the experimental and UBC3D-PLM model consolidated undrained triaxial test results with an effective confining pressure of 100 kPa	46
4.16	Pore water pressure versus axial strain graphs of the experimental and UBC3D-PLM model consolidated undrained triaxial test results with an effective confining pressure of 25 kPa	47
4.17	The rate of excess pore water pressure build up of combination 2 for a harmonic head at the bed with an amplitude of 0.01m and a period of 1	47
4.18	Stress history of critical point near toe with slope 1:5	49
5.1	The back pressure, pore water pressure, radial stress and axial stress versus time of the advanced triaxial tests with increasing back pressure rate	52
5.2	Effective stress paths of the advanced triaxial tests	53
5.3	The stress ratio versus rate of pore water pressure with the critical state stress ratio in red, the data points in black including the uncertainties and a fitted power function in blue	54
5.4	Axial strain versus time graphs for the advanced triaxial tests	55
5.5	Gradient of axial strain versus time for the advanced triaxial tests	55
5.6	Axial and volumetric strain versus time of the advanced triaxial tests	56
5.7	Rate of axial strain versus time of the advanced triaxial tests with a moving average of 30 points in blue	57
5.8	Axial strain and load cell (Lc) versus time of the advanced triaxial tests	58
5.9	Performance of the triaxial setup	59
6.1	The critical region of a submarine slope with ratio 1:5	62
6.2	Rotation of principal stresses in triaxial tests (Sadrekarimi, 2014)	64
6.3	Rotation of principal stresses observed in Plaxis 2D model 1	64
A.1	A general triaxial set-up	71
A.2	Theoretical undrained and drained triaxial test results of saturated sands for loose, medium and dense samples	74

LIST OF FIGURES

B.1	Cone resistance in kg/cm ² (Dinoloket, 2014)	75
B.2	Sleeve friction in kg/cm ² (Dinoloket, 2014)	76
C.1	Density measurement at point 1	77
C.2	Density measurement at point 2	78
C.3	Density measurement at point 3	79
C.4	Density measurement at point 4	80
D.1	Grain size diagram for the in situ and laboratory soil with the depth below NAP	81
F.1	Calibration of the back pressure controller and pore water pressure sensor with a digital manometer including the formulas of the trend line and coefficient of determination	84
F.2	Determination of the offsets and deformability of the triaxial setup	85
G.1	Consolidated drained triaxial test results: normalised deviatoric stress versus axial strain for low effective confining pressure ($p' = 14$ kPa)	86
G.2	Consolidated drained triaxial test results: volumetric strain versus axial strain for low effective confining pressure ($p' = 14$ kPa)	86
G.3	Consolidated drained triaxial test results: effective stress path for low effective confining pressure ($p' = 14$ kPa) with critical state line (CSL)	87
G.4	Consolidated undrained triaxial test results: excess pore water pressure versus axial strain for low effective confining pressure ($p' = 14$ kPa)	87
G.5	Consolidated undrained triaxial test results: normalised deviatoric stress versus axial strain for low effective confining pressure ($p' = 14$ kPa)	88
G.6	Consolidated undrained triaxial test results: effective stress path for low effective confining pressure ($p' = 14$ kPa) with critical state line (CSL)	88
H.1	The rate of excess pore water pressure build up for every combination of amplitude and period for the harmonic head at the bed	91
I.1	Cumulative density function of the deviatoric stress in kPa	93
J.1	The difference between the back pressure and pore water pressure versus time of the advanced triaxial tests with increasing back pressure rate	94
K.1	Normalised deviatoric stress plots versus time of the advanced triaxial tests for test 1	95
K.2	Normalised deviatoric stress plots versus time of the advanced triaxial tests to determine the point at which the deviatoric stress starts to drop	96
L.1	Effective stress ratio (p'/q) versus time for advanced triaxial tests	98
M.1	The back pressure, pore water pressure, radial stress and axial stress of the advanced triaxial tests with increasing back pressure rate and the effective stress path	99
M.2	Axial strain, volumetric strain and load cell versus time	100
N.1	Anisotropically consolidated undrained triaxial test: pore water pressure versus axial strain for $K_c=0.48$	101
N.2	Anisotropically consolidated undrained triaxial test: normalised deviatoric stress versus axial strain for $K_c=0.48$	101

LIST OF FIGURES

N.3 Anisotropically consolidated undrained triaxial test: effective stress path for $K_c=0.48102$

O.1 Instability at the end of the back pressure change triaxial tests 103

P.1 Axial strain versus time with moving average zoomed 104

List of Tables

- 2.1 Geoligival formations at Roompot East 11
- 2.2 Depth of the formations according to Deltatres and a borehole close to the scour hole 13
- 2.3 Code, coordinates, depths and date of the site investigation tests at the edge of the bed protection of Roompot East 13
- 2.4 Characteristics of the past flow slides of Roompot East from 1991 till 2010, with the location, year of occurrence, steepest slope ratio with corresponding depth, the average slope ratio with its total height and the length and width of the flow slide. 17
- 2.5 Locations of the ADCP measurement points at the deepest scour hole of Roompot East 18

- 3.1 Soil properties of the laboratory sand (Maghsoudloo, Galavi, Hicks, & Askarinejad, 2017) 21
- 3.2 Test plan for the conventional triaxial tests 23

- 4.1 Characteristics of the phases of numerical model 1: selection critical points 31
- 4.2 Initial and optimised Hardening Soil model parameters 33
- 4.3 The deviatoric stress and mean effective stress for stress points at 1 m below the bed in phase 2 of model 1 from toe to head 36
- 4.4 The deviatoric stress and mean effective stress for stress points at 1 m below the bed for slope 1:5, 1:3 and 1:2 39
- 4.5 Stress history of a critical point near the toe at 1 meter below the bed. 40
- 4.6 Water pressure (p_w) fluctuation at bed level with, $p_{w,mv}$ as the water pressure determined by the mean velocity 42
- 4.7 Characteristics of the phases of numerical model 2: pore pressure change with depth 44
- 4.8 Combinations of amplitude and period of the harmonic pore pressure fluctuation at the bed 44
- 4.9 Initial and optimised UBC3D-PLM model parameters 46
- 4.10 The maximum rate of excess pore water pressure accumulation for harmonic head fluctuations at 1 meter below the bed 48

- 5.1 Test plan with back pressure (BP) rate, B-value after saturation, void ratio after unloading (e_{au}) and relative density after unloading (RD_{au}) 51
- 5.2 List of the turning points and their characteristics for the advanced triaxial tests 54
- 5.3 The axial stain at the drop in deviatoric stress of the advanced triaxial test . . . 56

- I.1 Uncertainties of the triaxial test measurement and initial conditions with its mean value based on test 1 92
- I.2 Table of the uncertainties of the calculated triaxial test parameters with the expected value based on normal distributed input parameters of table I.1 and the equations in appendix E 93

List of symbols

ρ	density of water	kg/m^3
A	area	mm^2
B	B-value	-
c	cohesion	kPa
c_f	friction coefficient	-
C_u	uniformity coefficient	-
D	diameter	mm
D_0	initial diameter	mm
D_{60}, D_{50}, D_{10}	particle diameter related to cumulative mass percentile	mm
e	void ratio	-
e_{\max}	maximum void ratio	-
e_{\min}	minimum void ratio	-
f	frequency	Hz
F_a	axial load	kN
G_s	specific gravity	-
H	height sample	mm
H_0	initial height	mm
k	permeability	m/s
K_0, K_c	lateral earth pressure	-
k	roughness	m
l	characteristic length	m
L_c	load cell	kN
n	porosity	-
p	mean total stress	kPa
p_w	water pressure	kPa
p'	mean effective stress	kPa
φ	friction angle	°
q	deviatoric stress	kPa
RD	relative density	-
R	radius	m
t	time	s
T	period	s
u	pore water pressure	kPa
U	depth averaged velocity	m/s
u^*	shear velocity	m/s
V	volume	mm^3
V_0	initial volume	mm^3
V_{BP}	volume back pressure controller	mm^3
V_{CP}	volume cell pressure controller	mm^3
w_a	axial displacement	mm
z	water depth	m
ΔD_{avg}	average diameter change	mm
ΔV	volume change	mm^3

LIST OF SYMBOLS

ε_a	axial strain	%
ε_e	radial strain	-
η	radial strain	-
λ	wavelength	m
σ	stress or total stress	kPa
σ'	effective stress	kPa
σ'_1	major principal effective stress	kPa
σ'_3	minor principal effective stress	kPa
σ'_a	effective axial stress	kPa
σ'_r	effective radial stress	kPa
σ_1	major pinciple stress	kPa
σ_2	principal stress	kPa
σ_3	minor principal stress	kPa
σ_a	axial stress	kPa
σ_{BP}	back pressure	kPa
σ_r	radial stress	kPa
τ	shear stress	kPa
τ_0	bed shear stress	kPa
τ_{max}	maximum shear stress	kPa
τ_{mob}	mobilised shear stress	kPa
τ_{rel}	relative shear stress	-
ψ	dilation angle	°

Contents

Summary	i
Preface	ii
List of figures	vi
List of tables	vii
Symbol list	ix
1 Introduction	4
1.1 Case study: Eastern Scheldt barrier	4
1.1.1 Formation of scour holes	5
1.1.2 Monitoring and maintenance plan	6
1.2 Problem description	6
1.3 Objective and research question	6
1.4 Approach and report structure	8
2 Case study	10
2.1 Research before completion of the Eastern Scheldt barrier	10
2.2 Conditions to cause liquefaction flow slides	10
2.2.1 Condition: soil type	11
2.2.2 Condition: geometry	14
2.2.3 Condition: initiation mechanism	18
2.3 Recent studies of the submarine slopes in Zeeland	20
2.4 Conclusions	20
3 Soil characteristics	21
3.1 Materials and Methods	21
3.1.1 Materials	21
3.1.2 Methods	23
3.2 Test results and discussion	24
3.2.1 Isotropic consolidated drained test results	24
3.2.2 Isotropic consolidated undrained test results	26
3.3 Discussion and conclusion	27
4 Characterisation of local stress conditions	29
4.1 Model 1: Selection critical points	29
4.1.1 Model description	29
4.1.2 Model parameters	31
4.1.3 Parameter optimisation	32
4.1.4 Analysis calculation results of model 1	35
4.2 Model 2: Pore pressure change with depth	40

4.2.1	Water pressure fluctuation at the bed	40
4.2.2	Model description	43
4.2.3	Model parameters	44
4.2.4	Parameter optimisation	45
4.2.5	Analysis calculation results of model 2	47
4.3	Conclusions on model results	48
5	Experimental study	50
5.1	Experimental program	50
5.2	Triaxial test results and discussion	51
5.2.1	Principal stresses and pore water pressure versus time	51
5.2.2	Effective stress path	52
5.2.3	Determination turning points	54
5.2.4	Axial and volumetric strains versus time	55
5.2.5	Repeatability of the test results	58
5.2.6	Anisotropically consolidated undrained triaxial test results	59
5.2.7	Onset of instability	59
5.3	Limitations	60
5.4	Conclusions on experiments	61
6	Implications for the field	62
7	Conclusions and recommendations	65
7.1	Conclusions	65
7.2	Recommendations	66
	References	68
	References	68
	Appendices	71
A	Background	71
A.1	Triaxial compression test	71
A.2	Mechanical behaviour of saturated sands	71
B	Cone penetration test results	75
C	Density electrical measurements	77
D	Grain size distribution	81
E	Parameters triaxial test	82
E.1	Input parameters	82
E.2	Raw data	82
E.3	Calculated parameters	82
E.4	Calculated soil parameters	83
F	Calibration of the triaxial setup	84
G	Isotropically consolidated drained and undrained test results for low confining pressure	86

CONTENTS

H Excess pore water pressure results	89
I Uncertainties	92
J Graphs difference back pressure and pore water pressure versus time	94
K Turning point: drop deviatoric stress	95
L Stress ratio of the advanced triaxial tests	97
M Repeatability advanced triaxial tests	99
N Anisotropically consolidated undrained triaxial test results	101
O Observed instabilities triaxial tests	103
P Zoomed on the axial strain results	104

1 | Introduction

Liquefaction is the phenomenon of a sudden loss of soil shear strength under (semi)undrained conditions. Such loss is caused by the development of excess pore pressure leading to a reduction of effective stresses. When the effective stress reaches zero, the soil will behave like a fluid, in other words, it liquefies. Liquefaction is a common hazard in submarine slopes that consist of fully saturated, young, loosely packed, fine-grained and low-plasticity or non-plastic soils (De Jager, 2018), for example in the case of loose cohesionless sands and silts but also in the case of quick clays. Liquefaction can be initiated in these soils by a monotonic or cyclic trigger. Some triggers of liquefaction failures in submarine slopes are tidal effects, water waves, rapid sediment accumulation, water flows and earthquakes (Owen & Moretti, 2011; De Jager, 2018). The trigger events can be small and in some cases, the actual trigger is not apparent (Wilderom, 1979). Case histories have shown that liquefaction failures are often rapid, unexpected and affect large areas with large deformations (Olson, 2001), which makes the failure event hazardous. Therefore, liquefaction failure is one of the main geohazards of submarine slopes (De Jager, 2018). Other types of observed failure mechanisms in submarine slopes are shear failures and breaching which are both due to gravity loading. During breaching a steep local part of the slope retrogresses in an upward direction. In comparison with liquefaction, which occurs in loose sand and milder slopes, breaching occurs in denser soils and steeper slopes. Moreover, the time for breaching to occur is within hours to a day, while liquefaction usually does not take longer than 15 minutes (Van den Ham & Stoutjesdijk, 2014). However, breaching is often confused with liquefaction. One of the reasons is that the rate of development of the flow slide is hard to measure below the water table. Sometimes extensive field and laboratory testing campaigns are needed to define the mechanism (De Jager, 2018). Moreover, liquefaction flow slides can initiate or can be initiated by breaching (Mathijssen, de Jager, & Hooiveld, 2015) and the post-event morphology often looks similar. Both failure mechanisms are observed close to the Eastern Scheldt storm surge barrier. For this reason, the submarine slopes in this area are periodically monitored and investigated to avoid foundation failure (Wilderom, 1979; Raaijmakers et al., 2012).

This research is focusing on liquefaction failure mechanisms close to the Eastern Scheldt barrier. In this chapter, the case study will be discussed first. Next, the problem description is given followed by the objective and research question and the scope of this research. Finally, the outline is presented.

1.1 Case study: Eastern Scheldt barrier

The Eastern Scheldt barrier is a part of the Dutch Delta Works that protects several estuary mouths of the Rhine-Meuse-Scheldt delta from high water. The design of the Delta Works started after the February 1953 flood of the south-western part of the Netherlands. The consequences of this flood were catastrophic with the loss of 1,835 lives, the flooding of 140,000 hectares of land, 72,000 evacuations (Visser, 1986) and 130km of damaged levees.

The Eastern Scheldt barrier partially closes the Eastern Scheldt. The barrier is located between the islands of Noord-Beveland and Schouwen-Duiveland. It will close during severe storm conditions when the water level reaches 3m above NAP (Amsterdam Ordnance Datum). The construction of the barrier started in 1976 and the barrier was opened on 4 October 1986. The



Figure 1.1: Satellite image of the Eastern Scheldt barrier between Schouwen-Duiveland and Noord-Beveland depicted by a black square in the right bottom corner map of the Netherlands (Google Earth Pro 7.3.2, 2019; Nederland fietsland, n.d.)

estimated lifetime of this barrier is 200 years (van Velzen, Raaijmakers, & Hoffmans, 2015). The barrier extends across three islands, (Roggenplaat, Neeltje Jans and Noordland) and has three inlets; Hammen, Schaar and Roompot (figure 1.1). The length of the barrier is 9km including 5km of dams and 4km of gates with a width of 39.5m. A bed protection layer was constructed to prevent the pillars of the barrier from settlements and instabilities. The main function of this layer is to keep the erosion of the bed at a distance. Advancing erosion becomes a threat when the erosion occurs close to the barrier because undermining of the bed protection could occur. The bed protection layer has a length of 650 meters in Roompot and Hammen and 550 meters in Schaar. At 60 meters from the barrier till the edge of the bed protection, the layer consists of concrete blocks covered with steel slacks that are connected at the bottom to a geotextile. Besides the bed protection layer, a monitoring and maintenance plan was made to protect the barrier.

1.1.1 Formation of scour holes

The velocity profile at the Eastern Scheldt outlet changed due to the construction of the Eastern Scheldt barrier leading to the formation of scour holes behind the bed protection layer. The erosion causes steeper slopes, higher shear stresses in the subsoil and sometimes slope failures. Liquefaction failure could occur in loose sand; therefore soil improvement was done near the edge of the bed protection (Visser, 1986). However, the maximum depth for densification was 15 meters during the construction phase (Steenpoorte et al., 2012) and the maximum allowable scour depth, ten years after construction, was set to 25 meters below the original bed. In 1982, it was predicted that this maximum scour depth would be 30 meters. These 30 meters were assumed to be unacceptable and therefore a monitoring and maintenance plan was made (Rijkswaterstaat, 2013).

The development of the scour hole depth from 2007 till 2012 is shown in figure 1.2. The present clay layers are indicated in grey. When the scour hole reached the clay layer at a depth of 35 meters below NAP, the scouring was temporarily slowed down and expanded in the horizontal

direction. In 2012 Deltares predicted a range of the expected scour depth for 2050 (Raaijmakers et al., 2012), which was larger than expected at first. At Roompot East Deltares would expect that the potential scour depth is ranging between 40m and 85m if measures are not taken.

1.1.2 Monitoring and maintenance plan

The scour holes are monitored by executing bathymetry surveys two times a year. To protect the bed protection layer for undermining, slacks, with a density of 3000kg/m^3 , are dumped on top of the slopes, that are steeper than 1:5 (vertical:horizontal) over 5 meters (Projectteam OSK Rijkswaterstaat, 2014). The thickness of the slack layer is approximately 0.55 meter. This criterion is independent of the soil type.

From 2000 to 2012, the maintenance of the bed was not performed properly (Rijkswaterstaat, 2013). The protection layer settled and was damaged as a result of the instabilities that took place in this period. The largest instabilities took place in 2004-2005 leading to a mobilization of approximately $850,000\text{m}^3$ (van Velzen et al., 2015). A part of this volume was backfilling the scour hole. This backfilled soil was rapidly eroded later. Emergency slack dumpings, therefore, took place in 2012 (Rijkswaterstaat, 2013).

1.2 Problem description

This research is focusing on liquefaction slope failures close to the Eastern Scheldt barrier. Previous research showed that three conditions are required to cause liquefaction failure: the presence of a soil type that is susceptible to liquefaction, the presence of a critical slope geometry and an initiation mechanism (T. P. Stoutjesdijk, de Groot, & Lindenberg, 1998). Past flow slides showed that the soil near the Eastern Scheldt barrier could liquefy. Moreover, critical slopes are present because the scour hole slopes are still developing. So, the first and second condition to cause liquefaction failure are already known. However, the initiation mechanism of liquefaction flow slides is unclear. It is expected that the turbulent flow near the Eastern Scheldt barrier plays a role in initiating liquefaction flow slides (Janssen et al., 2017). One of the reasons for this expectation is that a link is observed between the maximum contraction of the flow and the depth of the scour holes. Moreover, turbulent flow creates water pressures at the bed which could generate excess pore water pressure buildups within the soil. These excess pore water pressure buildups play a major role in liquefaction failure. All in all, to confirm the initiation mechanism expectation, insight into the coupled processes of morphology, hydraulics and geotechnics is prerequisite.

1.3 Objective and research question

This research aims to improve the understanding of the liquefaction initiation mechanism near the Eastern Scheldt barrier. Furthermore, this is one of the first steps in relating the hydraulics and geotechnics of the submarine slopes near the barrier. It is expected that turbulent flow plays a role in the initiation mechanism and that this flow leads to water pressures fluctuations at the bed. Therefore, the response of the soil on water pressure fluctuations at the bed is investigated in this study. The main research question becomes:

What is the effect of water pressure fluctuations caused by the flow (hydraulic triggering) on the soil response of loose sand in submarine slopes close to the Eastern Scheldt storm surge barrier?

The main research question will be answered by an experimental study. Triaxial tests are selected for this study because a triaxial setup can simulate, control and measure the stresses that are

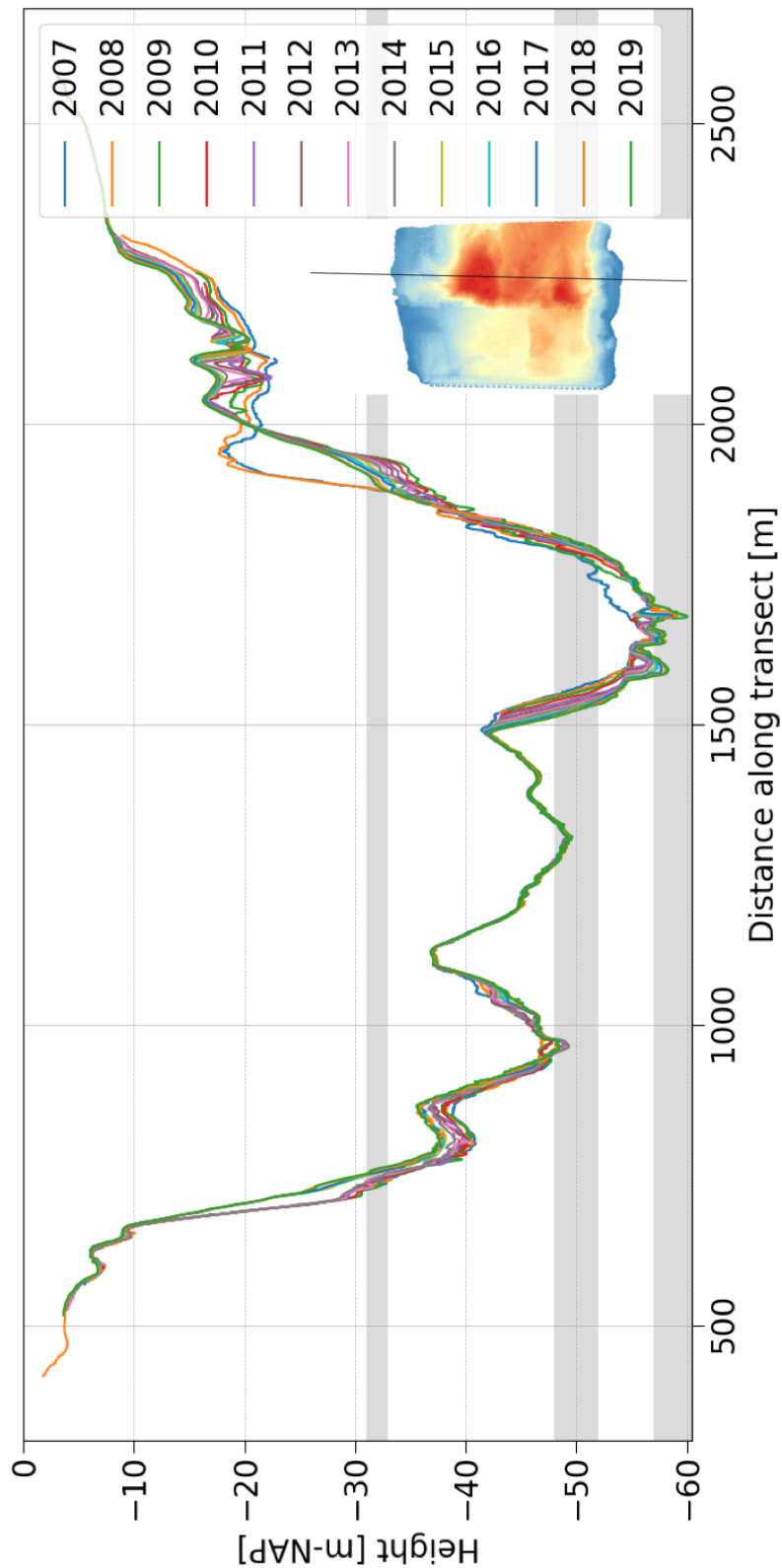


Figure 1.2: Cross-sections of Roompot East 2007-2019, with on the x-axis the distance along a transect parallel to the barrier and on the y-axis the depth below NAP in meters. The transect is depicted in the bottom corner by a black line and the deepest scour hole depths in red. The clay layers are given in grey based on (Projectteam OSK Rijkswaterstaat, 2014)

applied on a point in the field. More information about the triaxial setup and general soil behaviour of sand can be found in appendix A.

Sub-questions are formulated to answer the main research question:

1. What are the soil properties of a submarine slope near the Eastern Scheldt barrier and what is the slope geometry before failure?
2. Which part of the slope is more prone to become unstable (critical regions)?
3. What is the range of water pressure accumulation at the bed due to the water flow?
4. What are the stress conditions of a point inside the critical region?
5. What is the soil response to the hydraulic triggering in triaxial experiments?

The sub-questions are answered in chronological order because the answers of question 1 to 4 are needed to create a test plan for the experimental study that answers the last sub-question.

A critical point is assumed to be a point with a stress state that is close to the critical state of the soil, which will be elaborated in section 4.1.4.

The research focuses on the slope failure at Roompot East (figure 1.1). This location is selected because the scour hole depth is the largest and most critical in comparison with Roompot West, Hammen and Schaar.

1.4 Approach and report structure

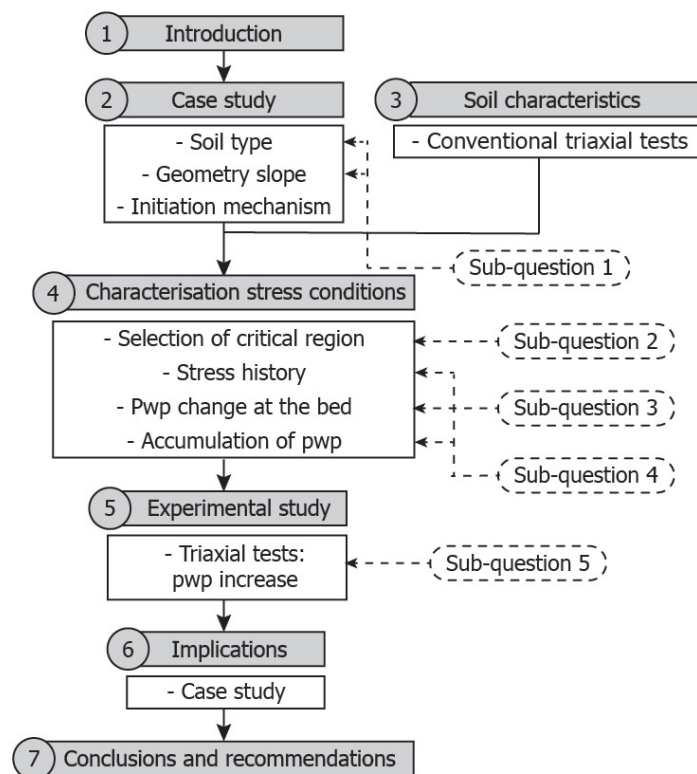


Figure 1.3: An overview of the report structure with the chapters and corresponding sub-questions

Figure 1.3 gives a graphical representation of the report structure. To answer the research question three main steps are taken: an investigation into the case study, the selection of stress

conditions by using a numerical model and an experimental study. The investigation into the case study presents a summary of the research of the flow slides in Zeeland before the construction of the Eastern Scheldt barrier and the recent studies of the submarine slopes in Zeeland. Furthermore, the conditions to cause liquefaction flow slides are presented including a selection of the site investigation data, grain size distributions, bathymetry data and flow velocity data. This study answers sub-question one and is given in chapter 2.

Sub-question 2, 3 and 4 are answered by the step: characterisation of the local stress conditions, given in chapter 4. To select critical points and their local stress conditions, Plaxis 2D is used, which is a finite element software. A finite element model is selected because such a model is able to quickly estimate the stress conditions at every point inside a slope. Model one consists of a slope, that represents a scour hole slope at Roompot East. The geometry of this slope is based on the bathymetry data and the soil properties of this model are based on the conventional triaxial test results (consolidated drained and undrained triaxial test) of the laboratory soil. These triaxial test results are presented in the soil characteristics chapter (chapter 3). A critical point inside this slope is selected and its stress history is defined. A second numerical model is used to define the excess pore water pressure buildup at a point below the bed. To define this buildup, a first approximation of the water pressure change at the bed is done.

The defined excess pore water pressure buildup is applied in the experimental study of chapter 5. The soil response to the rate of pore water pressure buildup is investigated by triaxial tests. The previous defined stress history (chapter 4) is applied to the samples after which the pore water pressure is increased. Sub-question 5 is answered in the experimental study chapter.

The relevance of the findings to the case study and the differences between the case study and the triaxial tests are presented in chapter 6, implications for the field. In the end, the conclusions and recommendations are presented, see chapter 7.

2 | Case study

This chapter gives an overview of the previous research of the flow slides of the shores and submarine slopes in Zeeland, starting with the research before completion of the Eastern Scheldt barrier in 1986. Next, the conditions to cause liquefaction flow slides are discussed, which is based on the past flow slides in Zeeland. Afterwards, the most recent studies are given. In the end, the chapter is summarized and the first sub-question is answered.

2.1 Research before completion of the Eastern Scheldt barrier

Before the construction of the Eastern Scheldt barrier (1976-1986), flow slides were already observed and investigated in Zeeland. In 1948, Koppejan et al. studied the flow slides at the shorelines in Zeeland (Koppejan, Van Wamelen, & Weinberg, 1948). Approximately 229 flow slides were registered between 1881 and 1946. Koppejan described the post-liquefaction profile of the flow slides as a gentle slope with angles of 3 to 4 degrees. Wilderom registered 1129 slope instabilities between 1800 and 1978 (Wilderom, 1979). Seventy-five per cent of the instabilities, that Wilderom investigated, was a flow slide instead of a shear failure because of their gentle slopes after failure. Only 145 flow slides were further investigated due to the availability of extended data, such as geometric features. However, these flow slides were not only initiated by liquefaction, but also by other failure mechanisms (e.g. breaching) that have the same post-failure geometry. Sometimes extensive field and laboratory testing campaigns are needed to define the failure mechanism (De Jager, 2018). It is hard to define the failure mechanism because liquefaction flow slides can initiate or can be initiated by other failure mechanisms. All in all, liquefaction flow slides were observed in Zeeland, but looking at the post-liquefaction profile of the flow slides is not enough to define the failure mechanism. Therefore, Wilderom studied the statistics of the flow slides (Wilderom, 1979). He stated that a criterion of flow slides occurring is the presence of Holocene sand with a loose state (compresses during loading) and that the presence of this sand can be an indication of the flow slide sensitive locations. Another criterion Wilderom noticed is an initial slope of 1:3 (vertical:horizontal) over a 5m slope height for liquefaction flow slides and a slope of 1:2 for shear failures. However, Silvis carried out a statistical analysis of the flow failures dataset in Zeeland and he concluded that the steepest slope angle over 5m is not the dominant factor in the formation of liquefaction flow slides. A minimum angle is crucial but not sufficient to start a flow slide. According to Silvis (1985), the occurrence of a liquefaction flow slide depends mainly on the present soils and external factors that could initiate a flow slide .

2.2 Conditions to cause liquefaction flow slides

Overall, investigating the flow slides in Zeeland resulted in three conditions that are required to cause a liquefaction flow slide.

2.2.1 Condition: soil type

The first condition is that the soil should be susceptible to liquefaction. De Jager (2018) stated that liquefaction occurs in fully saturated, young, loosely packed, fine-grained and low plastic or non-plastic soils. The soil stratigraphy, cone penetration test data, borehole data, grain size distribution and density measurements are investigated to define the susceptibility to liquefaction of the soil close to the barrier.

Soil stratigraphy

The soil stratigraphy in Zeeland is described by Koppejan (Koppejan et al., 1948) and Deltares (De Kleine, Vanhögen-Peeters, & Marges, 2012; Raaijmakers et al., 2012). The present geological formations at the Eastern Scheldt barrier area are listed in table 2.1. At the top, a Holocene sand layer is deposited, below which Pleistocene marine deposits were settled which are the Maassluis and Waalre formation. Below the Pleistocene layer is the Oosterhout formation deposited which is a Pliocene marine deposit. The soil stratigraphy as reported by Deltares is listed in table 2.1 (Raaijmakers et al., 2012) and includes the main soil characteristics. This table shows that fine-grained soils, in which liquefaction can occur, are present.

Series	Formation	Soil	Depth	Characteristics
Holocene	Naaldwijk	sand	36m	Loose, medium-fine to sometimes very coarse sands
Pleistocene	Waalre	sand	36-44m	Fluvial deposits, silty sand with alternating thin clay layers
	Maassluis	clay	44-45m	Thin clay layer
	Maassluis	sand	45-58m	Very fine to medium fine sand with grain sizes of 0.12-0.18mm (Raaijmakers et al., 2012)
Pliocene	Oosterhout	clay	58-64m	A few meters thick clay layer
	Oosterhout	sand	64m	Mainly very fine to medium fine grain sizes with intermittent shell layers

Table 2.1: Geological formations at Roompot East, with the depth below NAP (Raaijmakers et al., 2012) and some main soil characteristics

Borehole and cone penetration test data

The results of one borehole are compared with the soil stratigraphy of table 2.1. The borehole results are shown in figure 2.1 and the corresponding cone penetration test data are shown in appendix B. Information about the location and depths of these tests are given in table 2.3. This borehole is selected because it is the deepest and closest available borehole to the deepest scour hole at Roompot East in Dinoloket (Dinoloket, 2014). The position of the data collection is presented by the label "CPT" and "B" of figure 2.2.

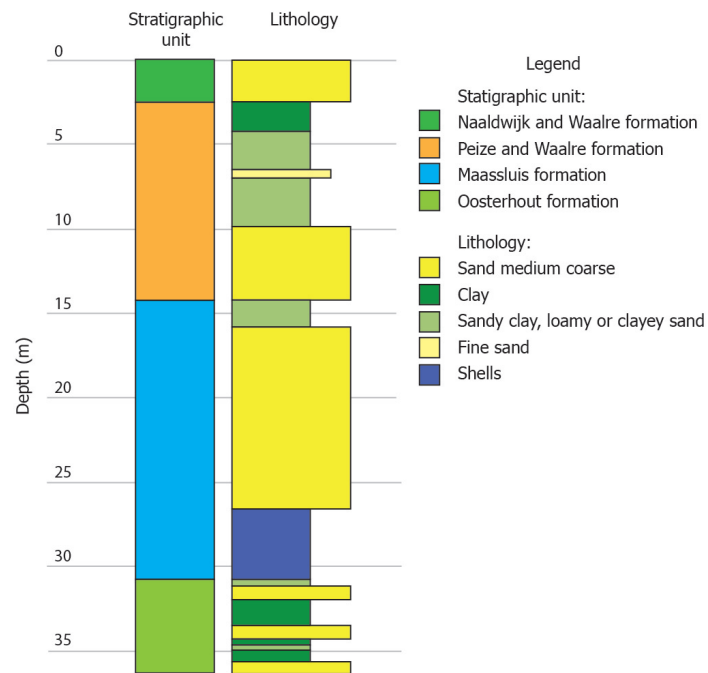


Figure 2.1: Borehole near the scour hole at Roompot East, with the ground level at 28.70 meters below NAP (Dinoloket, 2014)

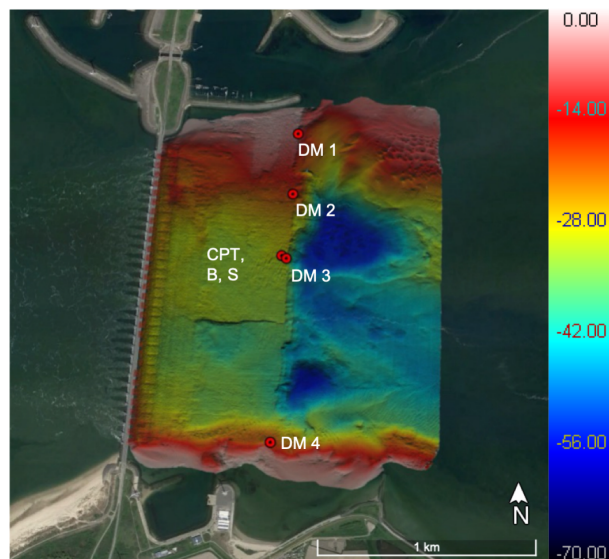


Figure 2.2: Location of the cone penetration test (CPT), the boring (B), the density measurements (DM) and sampling for sieving (S) at a bathymetry map of Roompot East with the depth below NAP and background from Google Earth Pro 7.3.2 (2019)

The boring was taken at 11-1976. In that time, the bed of the borehole was located at 28.70 meters below NAP. The first 2.45 meters consist of a Naaldwijk formation and Waalre formation. So, the Holocene deposits are positioned at lower depths at the borehole location than as reported by Deltares (table 2.1). However, the differences in the other formations are relatively small (2.2). The soil consists mainly of sand layers that are alternated by clay layers. In 2018 the bed was

eroded till 36.5 meters below NAP and reached the Waalre formation.

Formation	Depth Deltatres (m-NAP)	Depth borehole (m-NAP)
Holocene	36	28.70-31.15
Waalre	36-44	31.15-43
Maassluis	44-58	43-59.5
Oosterhout	58-65	59.5-65.2

Table 2.2: Depth of the formations according to Deltatres (Raaijmakers et al., 2012) and a borehole close to the scour hole, with the depth below NAP (Dinoloket, 2014)

Density measurements

Density measurements were taken at four points near the edge of the bed protection (figure 2.2 and table 2.3). These measurements were collected in 1978. In appendix C the test results of the electrical density measurements at Roompot East are given. The highest measured porosity was 49% (void ratio of 0.961). These density measurements show that zones with high porosities, thus low relative densities, are present near the Eastern Scheldt barrier. In addition to these zones, the recently sedimented soils are also generally loose and therefore susceptible to liquefaction.

Name	Code	GPS Coordinates		Bottom [m-NAP]	Depth [m-NAP]	Date
B, S	B42D0164	51°36'34.6"N	3°41'33.8"E	28.70	65.10	11/1976
CPT	S42D01535	51°36'34.6"N	3°41'33.8"E	28.40	38.80	09/1976
DM 1	S42D01588	51°36'53.9"N	3°41'37.7"E	7.60	35.2	09/1978
DM 2	S42D01589	51°36'44.3"N	3°41'36.5"E	30.55	38.1	09/1978
DM 3	S42D01590	51°36'34.2"N	3°41'35.0"E	7.55	38.1	09/1978
DM 4	S42D01591	51°36'6.4"N	3°41'31.6"E	25.65	36.5	10/1978

Table 2.3: Code, coordinates, depths and date of the site investigation tests at the edge of the bed protection of Roompot East

Grain size distribution

The field grain size data is coming from a boring located at the edge of the bed protection (see figure 2.2 label "S") collected at 11-1976. The grain size distribution of the soil at depth 28.70-60.57 meters below NAP is shown in figure 2.3. The soil consists mainly of sand. The D_{50} is between 0.17 and 0.2 for most of the samples, which is fine sand (0.063mm-0.2mm). Moreover, most of the samples are uniformly graded. The blue and grey sample of figure 2.3 are medium sand and coarse sand respectively. As stated by De Jager (2018), fine uniformly graded sands can be prone to liquefaction.

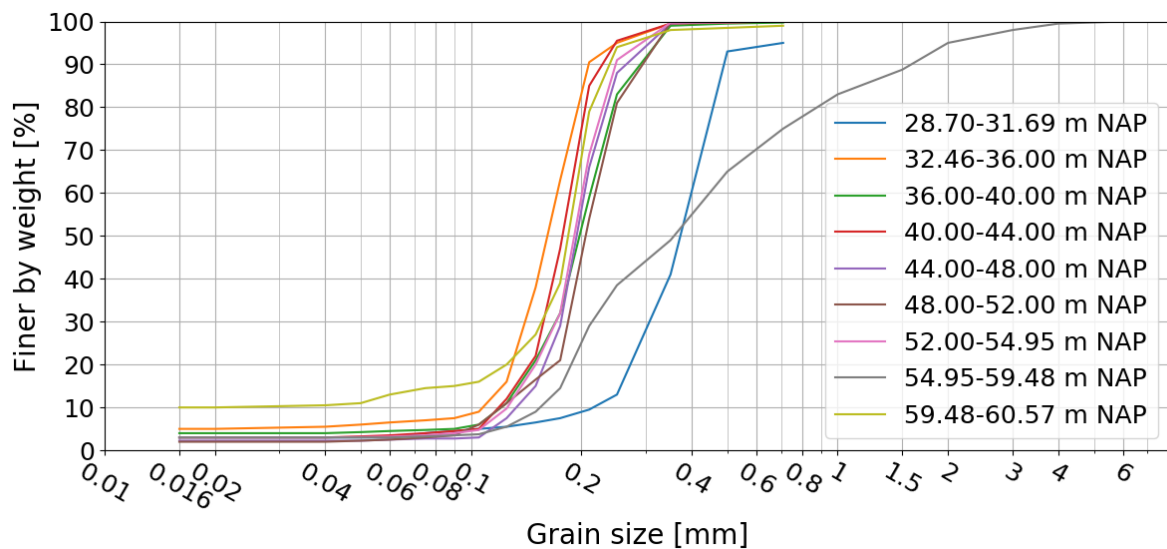


Figure 2.3: Grain size diagram for samples at the edge of the bed protection layer close to the deepest point of the scour hole (point S)

Silvis and De Groot (1995) looked into the geological information, soil investigation data, consisting of cone penetration tests, borings and in situ density tests, as well as laboratory tests including critical density tests to define susceptibility to liquefaction. They stated that Holocene sand, which has a grain size of 0.12-0.25mm, is susceptible to liquefaction when the effective stress is less than 150kPa, when the cone resistance is between 6-14MPa and when the relative density is smaller than 60%. Moreover, they stated that if the relative density is lower than 30%, the soil will certainly be susceptible to liquefaction.

The grain size distribution of figure 2.3 shows that sand is present with grains sizes between 0.12-0.25mm. The effective stress of approximately the first 15 meters is less than 150kPa. Moreover, the CPT data (Appendix B) shows that the cone resistance at this depth is between 6-14MPa. The relative density can be calculated with the minimum and maximum void ratio, but these values are unknown. All in all, according to Silvis and De Groot, the soil near the Eastern Scheldt barrier is susceptible to liquefaction.

2.2.2 Condition: geometry

The second condition for liquefaction is that the slope should be relatively steep and relatively high. Silvis and De Groot (1995) concluded that there is not a single critical combination of slope angle and height for the observed slope failures in Zeeland. The critical geometry parameters also depend on condition one, the sand characteristics. The influence of slope geometry on the occurrence of flow slides was investigated by Stoutjesdijk, De Groot and Lindenberg (1998). Their model predicts that the susceptibility to liquefaction slope failure increases as the density decreases while the slope angle and slope height increase (T. P. Stoutjesdijk et al., 1998). The bathymetry data and past slope failure data are presented in this section and confirm this statement.

Bathymetry

Bathymetry surveys are available from 1985 till 2018, two times a year. A single beam echo sounder was used up to the year 2003 and since 2004 onward, a multibeam echo sounder is

applied. The bathymetry data of Roompot East of August 2018 are shown in figure 2.4. The bathymetry map shows two deep scour holes of which the northern scour hole is the deepest. The maximum scour hole depth was 59.4 meters below NAP. The cross-section parallel to the barrier through the deepest point of the scour hole and perpendicular to the barrier and the same point are given in figure 2.5a and 2.5b respectively.

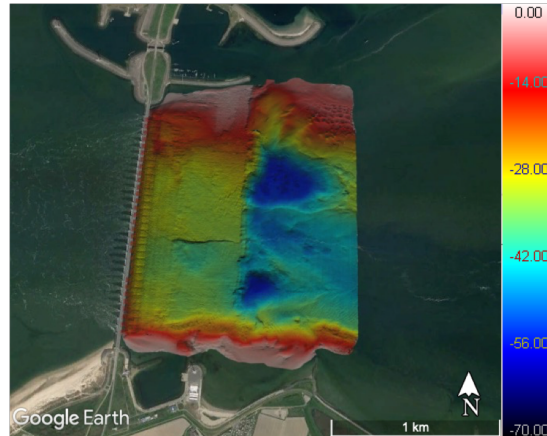
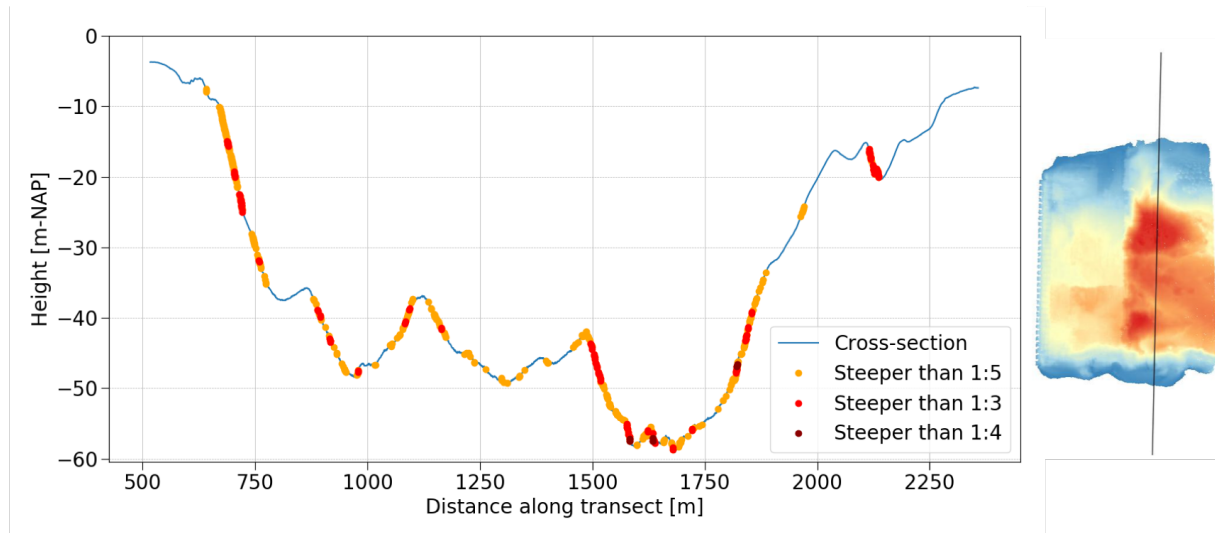


Figure 2.4: Bathymetry map of Roompot East of August 2018 (Google Earth Pro 7.3.2, 2019)

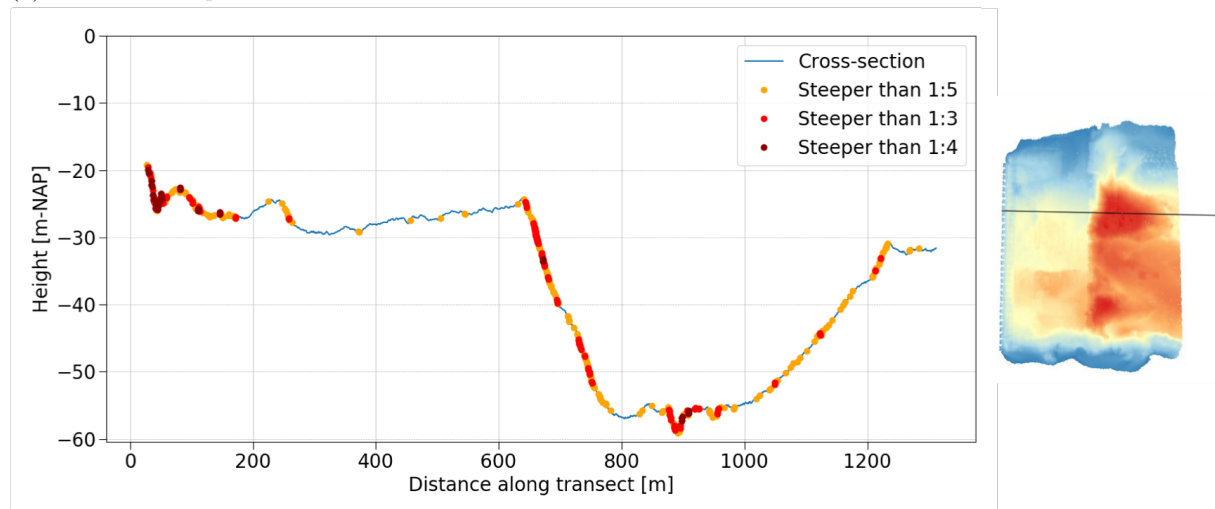
The marked parts of the cross-sections (figure 2.5) are representing the parts that are steeper than a slope corresponding to a ratio of 1:5, 1:3 and 1:2 over 1 meter distance along the transect. These plots show that the sloping bed is in general steeper than a 1:5 slope. The development of the scour holes at the cross-section parallel to the barrier shows that the scour holes are widening and becoming deeper in time (figure 1.2).

Past slope failures

A list of the slope failures between 1991 and 2011 is given in table 2.4 (T. Stoutjesdijk, Mastbergen, & De Groot, 2012). In this period, eleven instabilities were observed in the area of Roompot East. In general, the steepest slope ratio over 5 meters of the failed slopes is 1:2.2, while the average slope ratio is often smaller than 1:5. So, the average slope ratio is relatively small. Therefore, it is expected that the steepest part of the slope plays a larger role than the average slope ratio. The table of the past flow slides shows that just one flow slide occurred before 2001, so the frequency of flow slides appears to be increasing in time. One of the reasons for this increase is that there was no maintenance work in the period 2000-2012.



(a) cross-section parallel to the ESB



(b) cross-section perpendicular to the ESB

Figure 2.5: Cross-sections parallel and perpendicular to the barrier, through the deepest point at Roompot East in August 2018 with marked parts corresponding to part with slope ratios steeper than 1:5, 1:3 and 1:2 in orange, red and dark red respectively.

Nr.	Location	Year	Steepest ratio (1:x) over 5m	At depth [m-NAP]	Avg. slope [1:x]	Slope height [m]	Width [m]
1	North	1991-1992	2.1	13-18	9.4	32	200
2	South	2001-2002	1.9	37-42	6.7	50	200
3	Middle	2002-2003	1.7	45-50	4.1	28	100
4	North	2003-2004	2.1	43-48	5.3	40	120
5	South	2003-2004	2	17-22	6.4	50	120
6	North	2004-2005	1.3	29-40	6.3	44	>350
7	North	2006-2007	3.8	47-52	5.3	17	150
8	South	2007-2008	2.8	15-20	6.3	49	80
9	North	2008-2009	2.3	28-33	3.5	20	160
10	Middle	2008-2009	2.3	37-42	6.6	44	100
11	South	2009-2010	2.4	15-20	6.3	35	350

Table 2.4: Characteristics of the past flow slides of Roompot East from 1991 till 2010, with the location, year of occurrence, steepest slope ratio with corresponding depth, the average slope ratio with its total height and the length and width of the flow slide.

Slope geometry criteria of Rijkswaterstaat

Rijkswaterstaat defined scour hole geometry criteria for maintenance work of the bed. The scour hole geometry criteria over 5 meters height by Rijkswaterstaat before 2000 used to be dependent on the present soil. Maintenance work is done before the following criteria are exceeded (Rijkswaterstaat, n.d.):

Liquefiable sand	1:5
Shear failure sensitive sand	1:4
Densified sand	1:3
Pleistocene sand, without a Holocene sand top layer	1:3
Clay	1:2

In 2012, Rijkswaterstaat investigated the development of the scour holes and stated that the criterion of the 1:5 slope ratio over 5 meters height is conservative for relatively small slope heights but might be too optimistic for larger slope heights when the Zeeuwse statistics by Wilderom are taken into account (Rijkswaterstaat, 2013; Wilderom, 1979).

Rijkswaterstaat defined new criteria based on the observations near the barrier which are independent of the soil. The slope height is defined as the difference of the bottom and the edge of the channel. (Rijkswaterstaat, 2013)

Height < 40 meter	1:5
Height = 40 - 50 meter	1:6
Height = 50 - 60 meter	1:7
Height = 60 - 70 meter	1:8

Currently, the height is restricted to 40 meters. Deeper growth of the scour holes is prevented by maintenance (Janssen et al., 2018).

All in all, this bathymetry analysis shows that there is not one critical slope geometry. Moreover, the slopes have a complex geometry with changing slope ratios. At some places, the maximum

slope angle is exceeded but it is stable in time. Rijkswaterstaat is monitoring the depth of the scour holes and determined some criteria for maintenance work. At this moment, the maximum scour hole depth is approximately 36 meters. So, when the slope ratio is larger than 1:5, maintenance is done. However, the scour holes are still developing and the height of the slopes might exceed 40 meters when there is no maintenance.

2.2.3 Condition: initiation mechanism

The third condition to cause liquefaction is the presence of an initiation mechanism. Koppejan et al. (1948) reported that tidal flow, tidal water level variation and waves contribute to steepening of the slopes at the shorelines before the construction of the Eastern Scheldt barrier and that seepage pressures during falling water play a role in the triggering mechanism of flow slides. He assumed that the failures started during ebb-tide between half tide and low tide. According to Koppejan (1948), this is reasonable because the highest flow velocity in the channels occurs at half tide. Moreover, the seepage pressures are largest during the second half of ebb-tide. It is expected that the turbulent flow near the Eastern Scheldt barrier plays a role in initiating liquefaction flow slides (Janssen et al., 2017). The flow velocity ADCP (acoustic doppler current profiler) data at the North side of Roompot East approves Koppejan’s statement of the highest flow velocities that occur at half tide.

Velocity data

The flow velocities were measured with four fixed ADCP’s at the North side of Roompot East for a period of 37 days (07-06-2016 to 13-07-2016). The water velocity meters were positioned at the bottom of the deepest scour hole. The coordinates and depth are given in table 2.5 and depicted in figure 2.6. Point MP0301 was located at a shallower position, at the edge of the scour hole and in the middle of the gully. Point MP0302 was located at the deepest location of the scour hole. MP0302 was located at the steepest side slope of the scour hole at the northern scour hole slope and point MP0304 at the shallow slope side, where a large vortex was observed (Broekema, Labeur, & Uijttewaal, 2018) and flow slides. The measurements at point MP0304 were not registered.

ADCP	RD Coordinates	GPS Coordinates	Depth [m NAP]
MP0301	X = 37758, Y = 403540	51.60849 °N, 3.69458 °E	z = -45.9
MP0302	X = 37780, Y = 403718	51.61009 °N, 3.69484 °E	z = -55.5
MP0303	X = 37816, Y = 404019	51.61280 °N, 3.69526 °E	z = -31.6
MP0304	X = 37830, Y = 404128	51.61378 °N, 3.69543 °E	z = -25.6

Table 2.5: Locations of the ADCP measurement points at the deepest scour hole of Roompot East

The first current velocity measurement (bin 1) was taken 1.65 meters above the bed and the rest was positioned every half meter away from the bed. The time interval was one minute. The maximum flow velocities were measured at MP0302, at the maximum scour hole depth. Higher velocities result in the generation of higher water pressures. Therefore, MP0302 measurements at depth NAP-55.00 m were selected for this research.

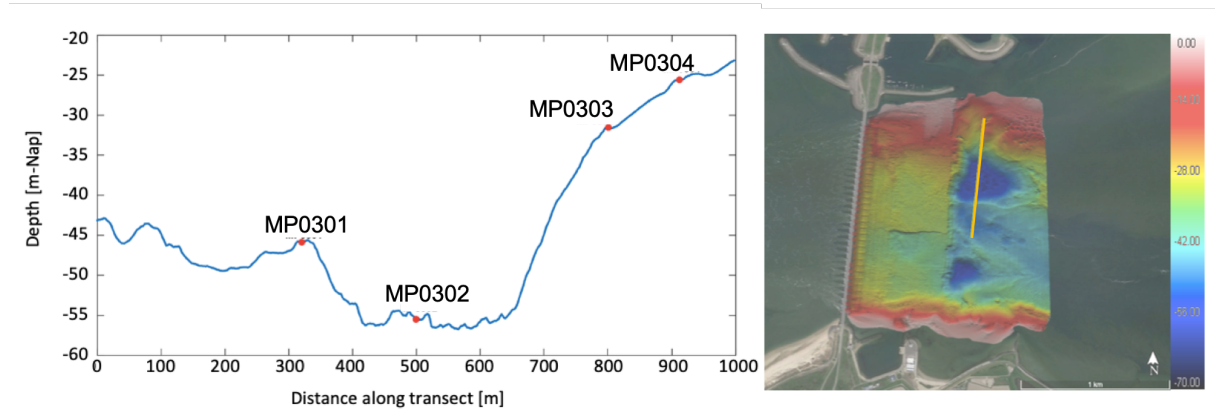


Figure 2.6: The ADCP measurement locations at a cross-section along the yellow transect, depicted at the right, that crosses the Northern scour hole at Roompot East from South to North (Google Earth Pro 7.3.2, 2019)

The velocities are converted to the direction of the tidal currents: the ebb directed flow is negative and has a direction of 294°N and the flood directed flow has a positive magnitude and is directed 114°N . The depth-averaged velocity of one day is given in figure 2.7 and shows two flood periods and two ebb periods. The water level is depicted in the same figure (figure 2.7). This figure shows that the maximum flow velocities are not exactly present at half tide but in between half tide and maximum flood. So, Koppejan's statement (1948) about the highest flow velocities occurring at half tide is questionable. However, it should be taken into consideration that the ADCP velocity measurements were not taken during a slope failure. Therefore, further research is needed to investigate the starting time of slope failure.

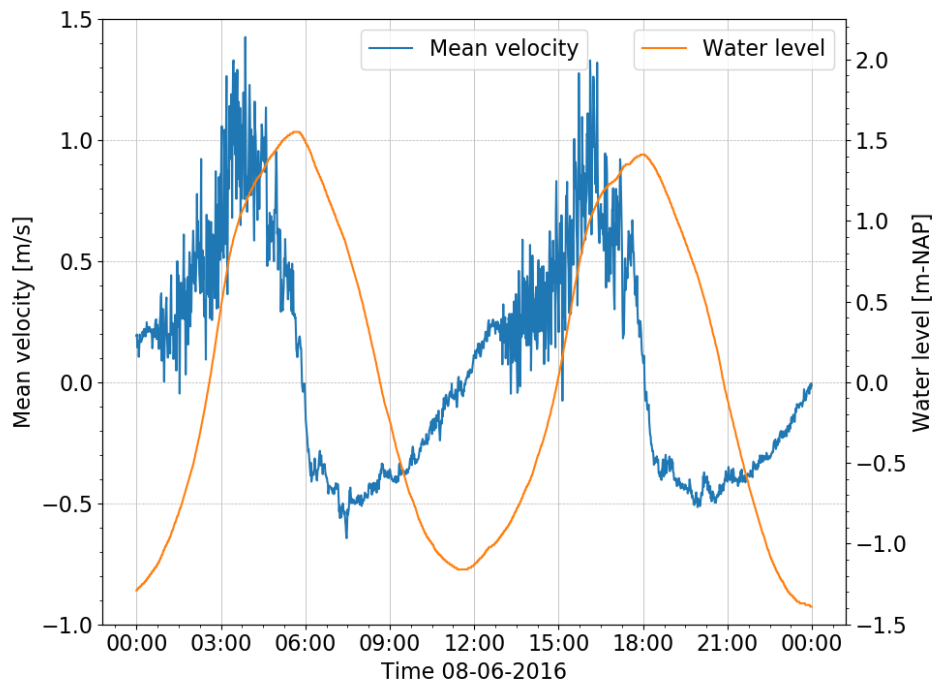


Figure 2.7: Depth-averaged velocity and water level at MP0302 (deepest point) at 08-06-2016

2.3 Recent studies of the submarine slopes in Zeeland

The bed close to the barrier has been monitored and inspections of the bed protection have been done by Rijkswaterstaat. Since the emergency maintenance works of the scour holes in 2012, Deltares and Delft University of Technology, commissioned by Rijkswaterstaat, have been investigating the flow slides, velocity profile and the influence of the maintenance methods on the stability of the bed (Janssen et al., 2017). A model with the material point method is investigated to describe the liquefaction process and breaching failure (Janssen et al., 2017). Moreover, further research has been done with the liquefaction tank into the mechanism of liquefaction slope failures and the effect of dumping slacks to stabilise the slopes. The research into the velocity profile of the Eastern Scheldt area shows high turbulent flow extending far behind the barrier (Janssen et al., 2018). The flow through the barrier has a jet-like structure and is strongly contracting while passing the barrier. The development of the scour holes was expected to end after a new morphological equilibrium was established. However, a positive feedback mechanism was observed. Broekema (2018) concluded that the lateral velocity gradients affect the horizontal contraction leading to relatively high near-bed velocities, which likely enhances erosion. Erosion leads to an even stronger horizontal contraction of the flow which in turn maintains the scouring potential (Broekema et al., 2018). The position of maximum contraction was found at the deepest points of the scour holes (Broekema et al., 2018). Therefore, a link between the flow and slope failures is expected.

2.4 Conclusions

The conditions that are required to cause a liquefaction flow slide are the presence of a soil that is prone to liquefaction, the presence of a slope that is relatively steep and high and an initiation mechanism. Previous research showed that liquefaction occurs in fully saturated, loosely packed, fine-grained and low or non-plastic soils (De Jager, 2018). The soil investigation data and grain size distributions show that liquefiable soil could be present.

The second condition is investigated by the bathymetry data and characteristics of the past flow slides. It can be approved that there is not one critical combination of slope angle and slope height. The average slope ratio of past slope failures was smaller than 1:5, but the steepest part of the slope over five meters had relatively high slope ratios (1:3 and 1:2). The bathymetry data shows that some slopes with ratios around 1:3 and 1:2 did not fail yet.

The third condition is the presence of an initiation mechanism. In 1948, it was already expected that the seepage pressures during falling water play a role in the initiation mechanism of liquefaction flow slides in Zeeland (Koppejan et al., 1948). Furthermore, previous research into the flow velocity profile of the Eastern Scheldt barrier area showed a slight increase in velocity with scour hole depth (Broekema et al., 2018). All in all, it is expected that the water flow plays a role in the initiation of liquefaction flow slides. To confirm this expectation, the influence of the currents on the behaviour of fine uniform sand in a submarine slope with a ratio of 1:5, 1:3 and 1:2 is experimentally investigated. The height and water level are 36.4 and 23 meters, respectively, which is based on the bathymetry data.

3 | Soil characteristics

This chapter describes the conventional triaxial test results which are consolidated drained and undrained triaxial compression tests. Appendix A gives some background information about these tests. The first objective of these tests is obtaining triaxial test data for the optimisation of the model parameters of the finite element models in chapter 4. The second objective of these tests is defining the critical state of the laboratory soil. In the first section, the materials are described. The available material characteristics are given in this section as well as the experimental setup that is used to perform the tests. Secondly, the methods are described including the test plan. Afterwards, the results, discussion and conclusion are reported.

3.1 Materials and Methods

3.1.1 Materials

Soil

The selected material for the triaxial tests and tests of the experimental study (chapter 5) is Geba sand which is a uniform fine silica sand. The geotechnical soil properties of the laboratory sand are given in table 3.1. The grain size distribution is shown in figure 3.1 and compared with the grain size distribution of the in situ soil in appendix D. The uniformity coefficient is calculated:

$$C_u = \frac{D_{60}}{D_{10}} \quad (3.1)$$

The average D_{60} and D_{10} quantities of the laboratory sand are 0.122 mm and 0.079 mm, respectively. The uniformity coefficient is slightly larger than 1, circa 1.54, therefore the laboratory soil is uniform and poorly graded. Because the grain size distribution of the laboratory soil is uniform, the particle segregation is assumed to be low during triaxial sample preparation. Therefore, the samples are closer to a homogeneous soil which enables reproducible tests. Moreover, this sand is also used for the liquefaction tank tests. A comparison of the laboratory soil and the soil of the case study are compared in appendix D.

Noriega (2015) used an electron microscope to analyse the grain shape. He stated that the shape of the particles is ranging from elongated to cubic and that they are in general angular round (Noriega, 2015).

Parameter	Name	Soil	Unit
Specific gravity	G_s	2.67	-
Minimum void ratio	e_{\min}	0.64	-
Maximum void ratio	e_{\max}	1.07	-
Mean particle size (50%)	D_{50}	0.11	mm
Permeability	k	4.2E-5	m/s
Cohesion	c	0.0	kN/m ²

Table 3.1: Soil properties of the laboratory sand (Maghsoudloo et al., 2017)

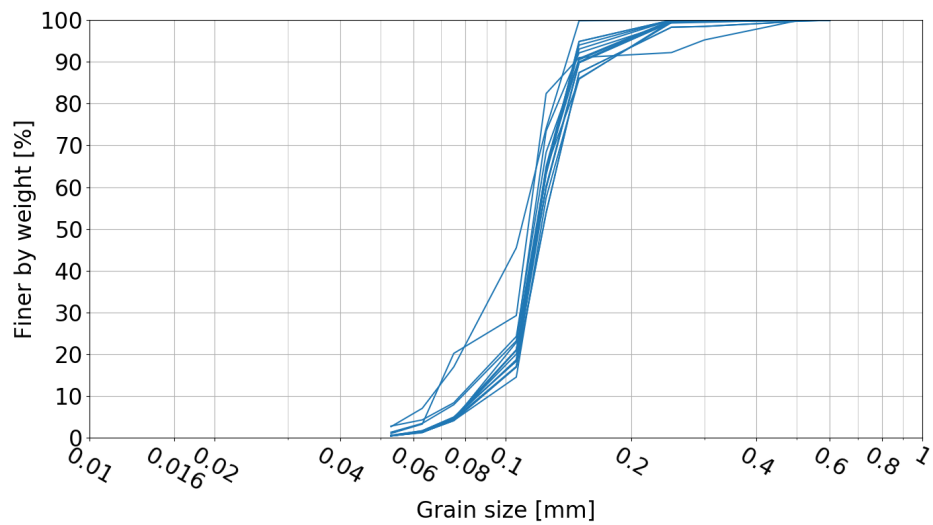


Figure 3.1: Laboratory sand grain size distribution for 16 random sample batches (Krapfenbauer, 2016)

Experimental setup

In this research, triaxial tests are strain-controlled and performed to investigate the soil response under the development of excess pore water pressures. One GDS load frame-based triaxial testing system is used with a submersible 1kN load cell and back pressure and cell pressure volume controllers, figure 3.2. The axial displacement is measured by a linear variable displacement transducer (LVDT). In Appendix E the used triaxial input values, raw data and calculated parameters are listed with their symbols and formulas. The accuracy of the setup for pressures is $\pm 1\text{kPa}$ and for volume is $\pm 300\text{mm}^3$ (Muraro, 2019). The calibration of the controllers is given in appendix F and the uncertainties in appendix I.

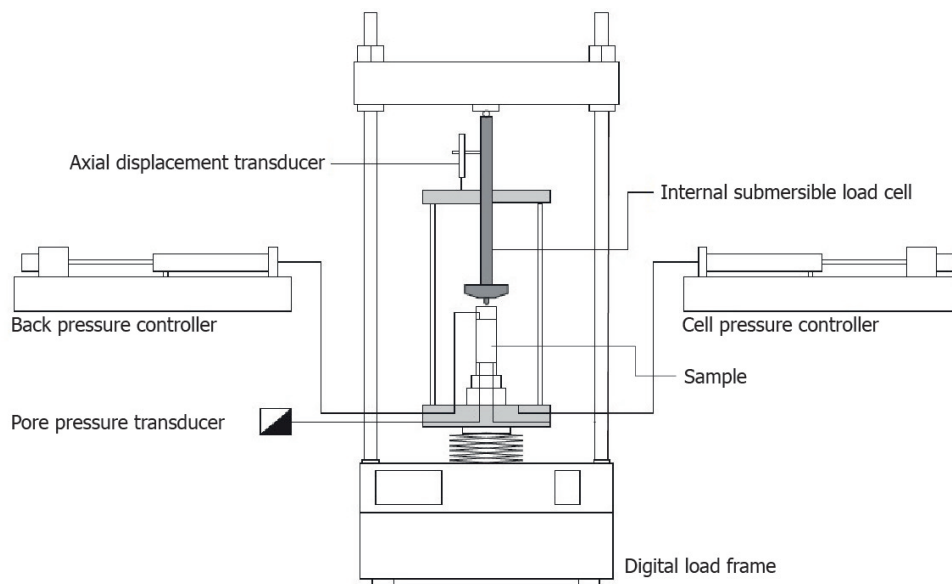


Figure 3.2: Triaxial testing equipment based on Muraro, 2019

3.1.2 Methods

In this chapter, the critical state of the laboratory soil and its soil behaviour under drained and undrained conditions is defined. Therefore, three consolidated drained triaxial tests and three consolidated undrained triaxial tests are performed with different effective confining pressures to define the location of the critical state line. Two isotropic consolidated tests, one drained and one undrained are performed at low confining pressure (14kPa) to approve the critical state line. For performing the triaxial tests, the manual of soil laboratory testing by Head and Epps is used (Head & Epps, 2014).

Test plan isotropic consolidated triaxial compression tests		
Test nr.	Drained/undrained	Eff. confining pressure(s) [kPa]
1,2,3	Drained	25, 100 and 200
4,5,6	Undrained	75, 100 and 150
7	Undrained	18.8
8	Drained	18.8

Table 3.2: Test plan for the conventional triaxial tests

Sample preparation

The triaxial samples are prepared by a modified wet pluviation technique. A syringe is used to prepare the sample. This preparation technique is assumed to be most suitable for preparing relatively loose fully saturated samples that are reproducing the conditions of river deposits. The samples are enclosed by a rubber membrane with a thickness of 0.25mm at the sides and by 2 filter papers and 2 porous stones at the top and bottom. They are prepared inside a mould with a diameter of 50 mm and a height of 110 mm, so the samples have a height to diameter ratio of approximately 2:1. A syringe is used to prepare the sample, to be sure that the sand does not get into contact with air. After preparation, vacuum (-5kPa) was applied to the sample which made it possible for the sample to stand by itself (figure 3.3).



Figure 3.3: Triaxial test sample under vacuum

Test procedure

After installation of the samples in the triaxial apparatus, the samples are fully saturated to achieve a minimum Skempton's B value of 0.95. The saturation phase consists of B-checks and saturation stages. During the B-check the cell pressure increases under drained conditions and during the saturation stages, the back pressure was increased with a magnitude of 10kPa difference with the cell pressure. The void ratio after preparation is referred to as the initial void ratio e_i . The soil was consolidated isotropically under the predefined effective confining pressures of table 3.2. The relative density after consolidation is between 23% and 31%. After consolidation, the samples are sheared by increasing the axial force with a loading velocity for the strain rate of 0.2 mm/min.

3.2 Test results and discussion

The test results are shown and discussed in this chapter. The results of the isotropically consolidated undrained and drained triaxial tests at low confining pressure are given in appendix G.

3.2.1 Isotropic consolidated drained test results

The consolidated drained triaxial test results are given in figure 3.5 and figure 3.6. Figure 3.4 shows pictures of the failed drained soil samples. At constant radial stress (σ_r) the mode of failure is a barrel for relatively low densities, a shear band for higher densities and a fracture for relatively high density soil samples (Desrues, 2004). The mode of failure changes from fracture to shear band to barrelling with an increase in confining pressure. The soil samples of figure 3.4 all have a barrelling failure mode except for figure 3.4a representing the consolidated drained test with a confining pressure of 75kPa. The confining pressure is low in comparison with the other drained tests and the density is 1%-2% larger, but this falls within the accuracy of the relative density measurements. Due to the failure mode, this sample is expected to be dense instead of loose. A sample that is loose and susceptible to liquefaction, would have a barreling failure mode.

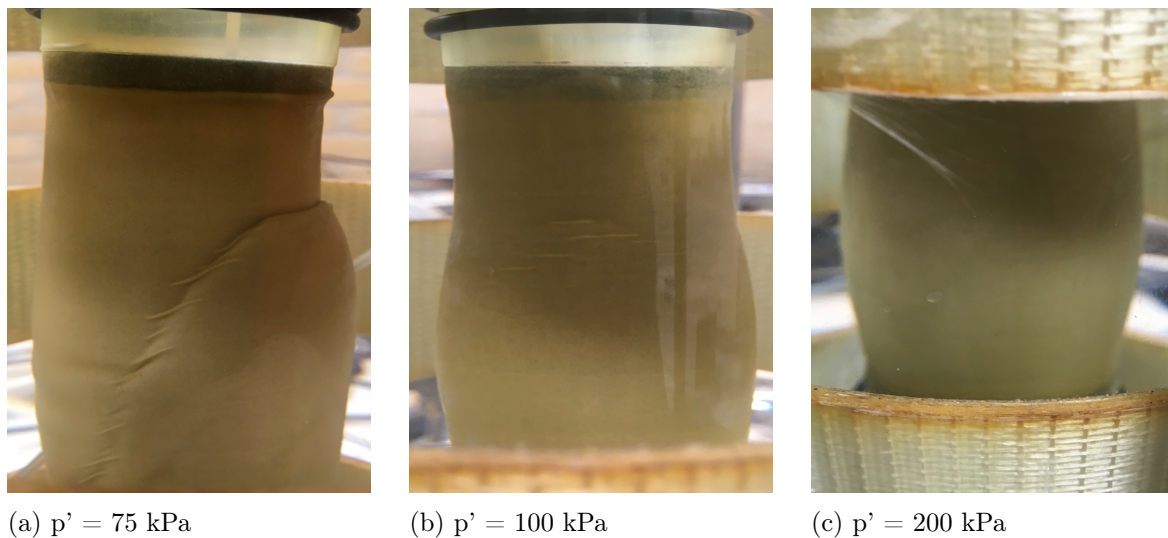


Figure 3.4: Pictures of consolidated soil samples at the end of the drained triaxial compression tests for corresponding effective confining pressures

The normalised deviatoric stress versus axial strain graph for the triaxial drained test results is given in figure 3.5. The tests with an effective confining pressure of 75kPa and 100kPa have a peak stress. The volumetric strain versus axial strain graphs show compression at the start of the test for strains smaller than 3% and is followed by dilation with increasing axial strain. The dilation angle of the tests with effective confining pressure of 100kPa and 150kPa seems identical, because the slope during expansion is equal until circa 10% axial strain.

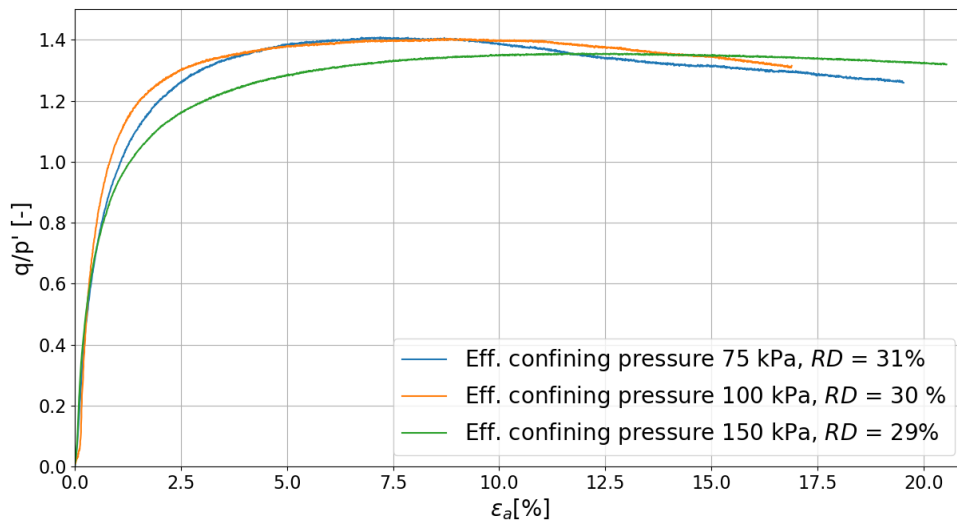


Figure 3.5: Consolidated drained triaxial test results: normalised deviatoric stress versus axial strain, with the relative density after consolidation

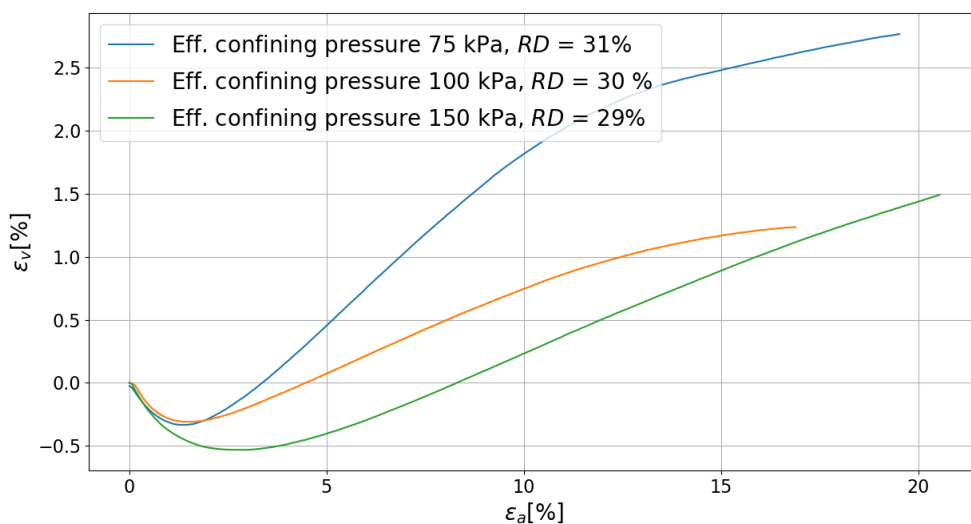


Figure 3.6: Consolidated drained triaxial test results: volumetric strain versus axial strain, with the relative density after consolidation

3.2.2 Isotropic consolidated undrained test results

The consolidated undrained triaxial test results are given in figure 3.7-3.9. The effective stress path of the undrained triaxial tests is given in figure 3.7. First, the mean effective stress is decreasing until a transformation point is reached. After this point, the mean effective stress is increasing with increasing deviatoric stress. The excess pore water pressure versus axial strain graphs (figure 3.8) show compression at relatively low axial strains with an increase in pore water pressure. When the excess pore water pressure turns negative the samples are dilating. From figure 3.9 it is not clear if the critical state is reached because the normalised deviatoric stress is slightly increasing. Moreover, the tests stopped at relatively low axial strains because the maximum allowable load was reached, which was 0.95 kN.

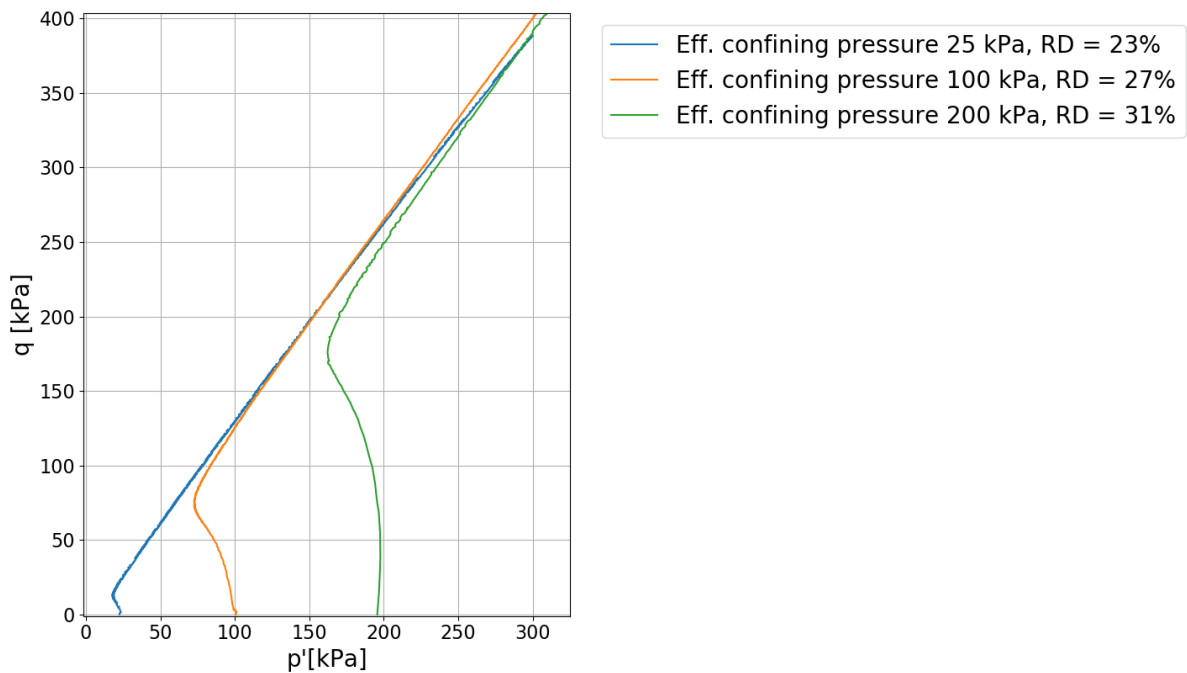


Figure 3.7: Consolidated undrained triaxial test results: deviatoric stress versus mean effective stress, with the relative density after consolidation

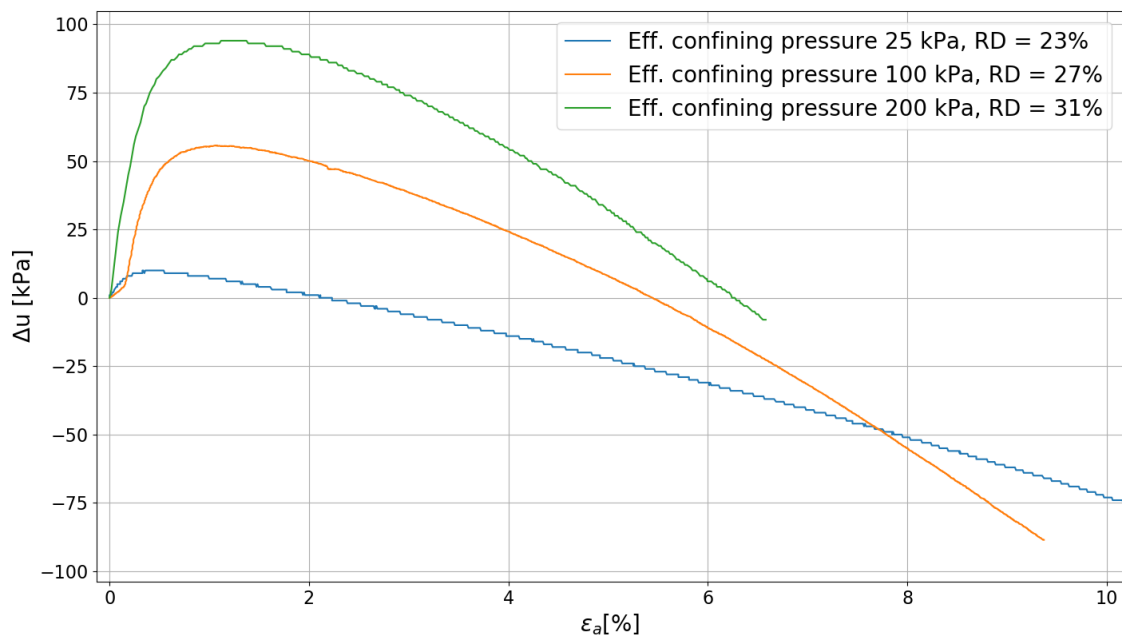


Figure 3.8: Consolidated undrained triaxial test results: excess pore water pressure versus axial strain, with the relative density after consolidation

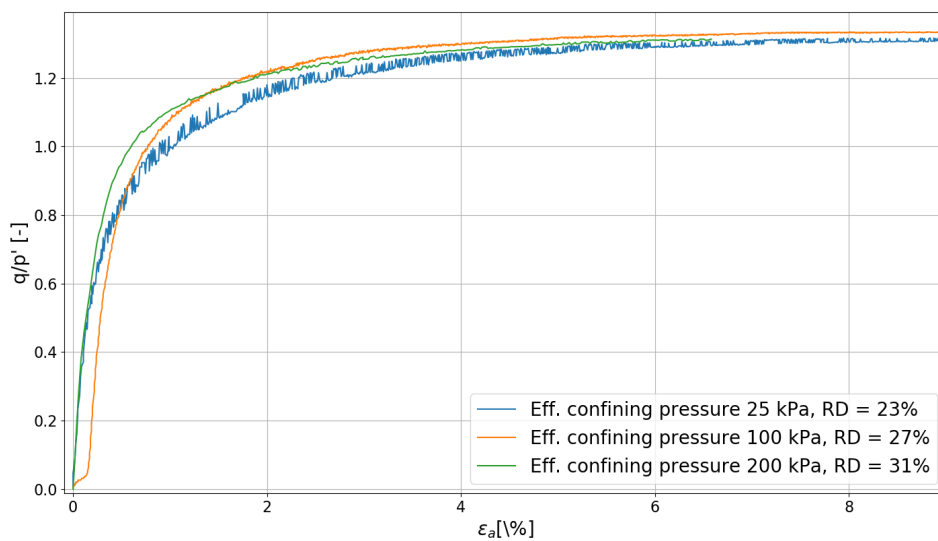


Figure 3.9: Consolidated undrained triaxial test results: normalised deviatoric stress versus axial strain, with the relative density after consolidation

3.3 Discussion and conclusion

Based on the undrained triaxial test results the critical state cannot be determined accurately. However, in combination with the drained triaxial test results and the observations at the end of the test (figure 3.4), the critical state can be defined. The normalised deviatoric stress versus axial strain graphs for the drained tests show that the critical state is reached because the normalised deviatoric stress is almost constant. Due to barrelling of the sample (figure 3.4), the

area correction to calculate the deviatoric stress is probably inaccurate (Jefferies & Been, 2016). This could be a reason why the deviatoric stress slightly drops. Moreover, the drained test with a confining pressure of 75kPa is behaving denser than expected because the failure mode has a shear plane. Therefore, this test is not taken into account for defining the critical state line. The critical state line is shown in figure 3.10 and 3.11 and has a inclination of 1.287. So, the critical friction angle is 33° which is calculated by equation 4.6. The triaxial test results of this chapter are used to optimise the input parameters for the finite element models of chapter 4.

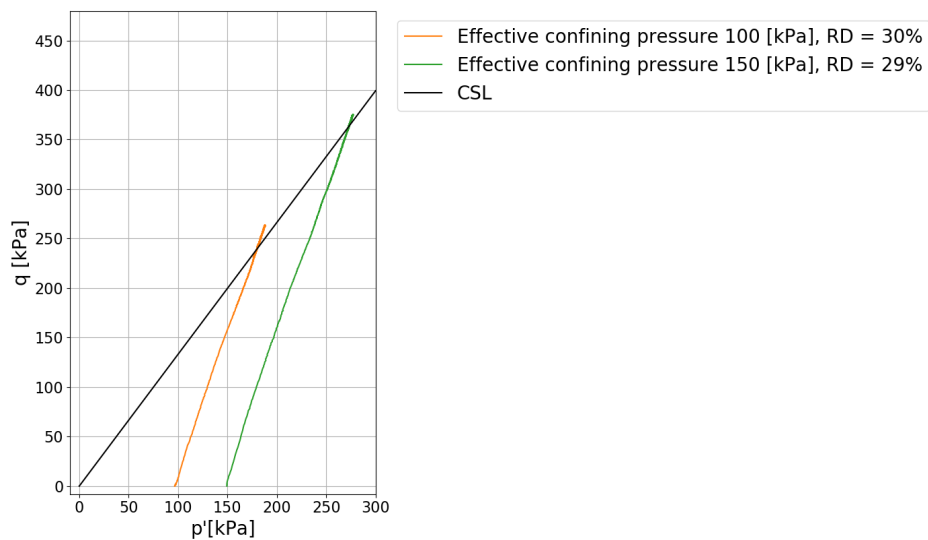


Figure 3.10: Consolidated drained triaxial test results: effective stress path with critical state line (CSL) and relative density after consolidation

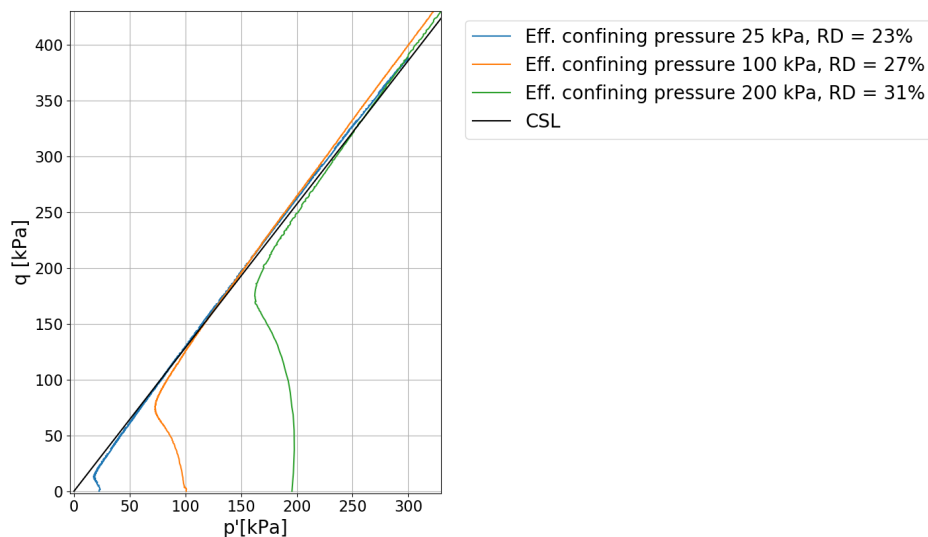


Figure 3.11: Consolidated undrained triaxial test results: effective stress path with critical state line (CSL) and relative density after consolidation

4 | Characterisation of local stress conditions

The characterisation of the local stress conditions is done in order to design the test plan and to obtain the stress conditions for the experimental study (chapter 5). To achieve these goals finite element models are analysed in Plaxis 2D because this software can quickly estimate the stress conditions of every point inside a soil geometry.

Static and dynamic analysis are performed with Plaxis 2D modelling. The hardening soil model, model 1, is applied in the static analysis to simulate the stress history and to define the critical points within a slope. Three slopes with a ratio of 1:5, 1:3 and 1:2 and a height corresponding to the maximum measured depth below NAP (59.4 meters below NAP) are selected to investigate further. This selection is based on the findings of the case study chapter (chapter 2).

The UBCSand PLM model is used in the dynamic analysis to model the accumulation of excess pore water pressure with depth in one-dimensional space. The pore pressure changes, due to currents, propagate as waves downwards. The soil influences the amplitude, duration and frequency of the pore pressure waves. This phenomenon is investigated with model 2. First, an approximation of the water pressure change at the bed due to currents is done by a conversion of the velocity data (section 2.2.3). Afterwards, the water pressure change is implemented in Plaxis 2D. In the end, the calculation results of the model are used to define the rate of accumulation of pore water pressure at the depth of the critical point that is defined by model 1.

Both numerical models are analysed in this chapter and elaborated in separate sections. The first section starts with a model description, followed by the model parameters, the parameter optimisation and the analysis of the calculation results. The second section starts with the water pressure fluctuation at the bed followed by the same elements as the first section. In the end, the conclusions are given including the answers on sub-question 2, 3 and 4.

4.1 Model 1: Selection critical points

The purpose of model 1 is to answer sub-question 2: "Which part of the slopes is more prone to become unstable (critical regions)?" and partly sub-question 4: "What are the stress conditions of a point inside the critical region?".

4.1.1 Model description

Model 1 consists of two phases. A schematic overview of the geometry of model 1 is given in figure 4.1. Phase 1 is the initial phase that represents the bed near the edge of the bed protection before erosion started (figure 4.1a). This initial phase is modelled as a horizontal bed. Phase 2 has a sloping bed and represents the bed after scouring occurred (figure 4.1b). It is modelled as an excavation of the initial phase. The slope is a two-dimensional submarine slope with a linear sloping bed, although a slope in the field has multiple slope angles (see subsection 2.2.2). The slope of model 1 has a ratio of 1:5, is 182 meters long and 36.4 meters high. The results of the slopes with ratio 1:3 and 1:2 are discussed in section 4.1.4. The maximum depth below NAP is 59.4 meters. The water table above the bed at the head of the slope is 23 meters. The average

water level is selected because the stress history of the bed is investigated which is a long term process.

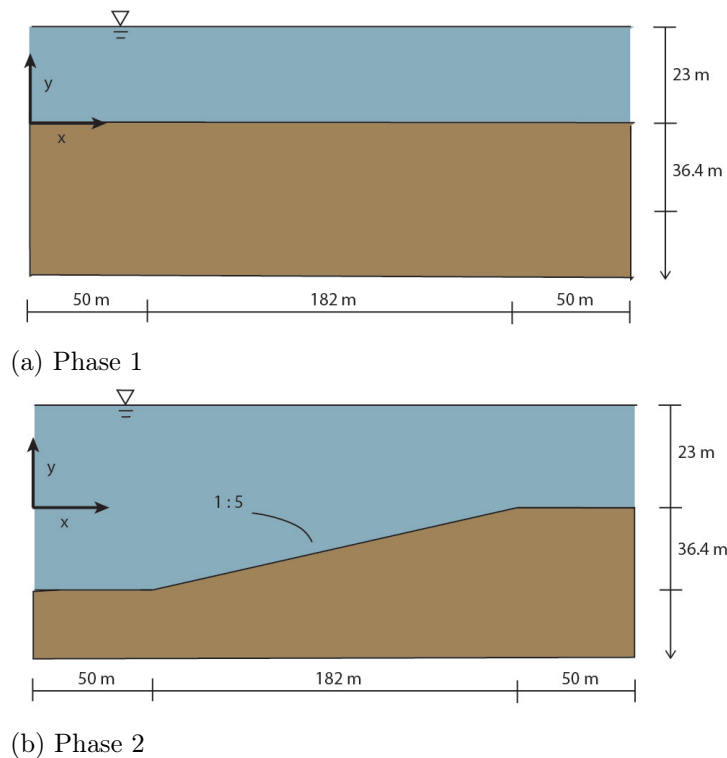


Figure 4.1: Schematic picture of the model 1 phases for a slope with a 1:5 ratio

The characteristics of the phases of model 1 are presented in table 4.1. A Hardening Soil model is applied, because this soil model is well suited for unloading situations (Brinkgreve, 2018a). The model contains 15-node elements with a non-uniform mesh. Relatively small element sizes are selected for the zones with stress conditions that lay closer to the critical state line in a stress path plot. The boundaries can be defined by an iterative process; starting with boundaries far from the slope and decreasing the boundary distances just before the changes in stresses are going to be significant. However, the boundaries are only checked instead of optimized by an iterative process. The X_{\min} boundary and the X_{\max} boundary are located at 50 meters from the toe and head of the slope, respectively. Afterwards, the stresses are compared with a model with boundaries far away from the slope. The changes are assumed to be insignificant. The bottom boundary Y_{\min} is set far away from the slope (at -195 meters), to be sure that the bottom boundary is not influencing the failure mechanism.

The results of model 1 are used for two purposes. First, the critical points within the slope are defined. Secondly, the stress history of these points is obtained from this model. The critical points are selected by analysing the relative shear stresses (equation 4.3). These points are positioned closer to the critical state line and therefore minor stress changes could lead to instability or failure. The stress history of a critical point is defined by the stress changes of phase 1 to phase 2.

Model 1: Selection critical points			
Calculation type		Phase 1	Phase 2
		K_0 procedure	Plastic
Deformation boundary condition	X_{MIN}	normally fixed	normally fixed
	X_{MAX}	normally fixed	normally fixed
	Y_{MIN}	fully fixed	fully fixed
	Y_{MAX}	free	free
Groundwater flow boundary condition	X_{MIN}	closed	closed
	X_{MAX}	open	open
	Y_{MIN}	closed	closed
	Y_{MAX}	open	open

Table 4.1: Characteristics of the phases of numerical model 1: selection critical points

4.1.2 Model parameters

The parameters of the Hardening Soil model are listed in this section and coming from the Plaxis material models manual (Plaxis, 2019b). The initial input parameters are based on the drained triaxial test results, correlations from literature and default values.

The failure parameters as in the Mohr-Coulomb soil model are:

- c : (Effective) cohesion [kN/m²]
- φ : (Effective) angle of internal friction [°]
- ψ : Angle of dilatancy [°]
- σ_t : Tension cut-off and tensile strength [kN/m²]

The cohesion and friction angle are 0°(table 3.1) and 33°(chapter 3) respectively. The angle of dilatancy has an order of magnitude of: $\psi = \phi - 30^\circ = 3^\circ$ (Plaxis, 2019b).

The basic parameters for soil stiffness are:

- E_{50}^{ref} : Secant stiffness in standard drained triaxial test [kN/m²]
- E_{oed}^{ref} : Tangent stiffness for primary oedometer loading [kN/m²]
- E_{ur}^{ref} : Unloading/ reloading stiffness (default $E_{ur}^{ref} = 3 * E_{50}^{ref}$)
- m : Power for stress-level dependency of stiffness [-]

The consolidated drained triaxial tests (chapter 3) are used to define the initial parameters for soil stiffness. The drained triaxial test results with an effective confining pressure of 75kPa are not taken into account, because this test shows a denser response than the tests with a confining pressure of 100kPa and 150kPa.

The secant stiffness, also know as the triaxial loading stiffness, E^{50} , is equal to the tangent of the line going through the origin and the points with $q = q_{max}/2$, see the solid black and grey line of figure 4.2 and the dotted lines for the $q = q_{max}/2$ values. The E^{50} for a confining pressure of 100kPa is 18557kN/m² and the E^{50} for a confining pressure of 150kPa is 20806kN/m².

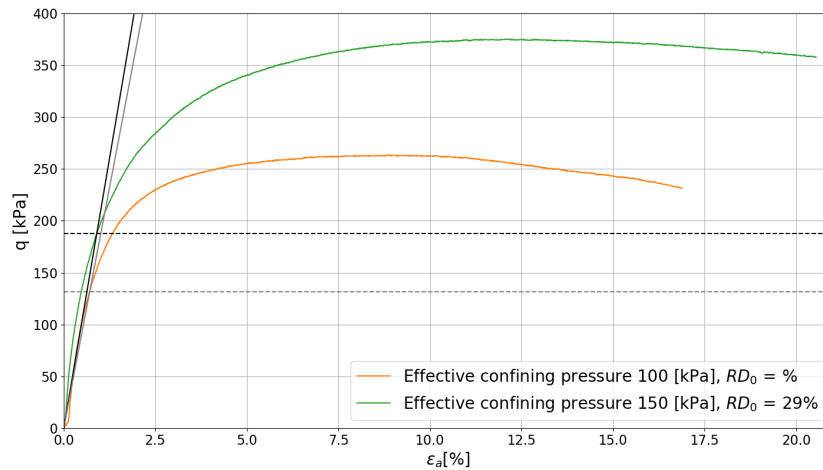


Figure 4.2: Consolidated drained triaxial test results and the determination of E^{50}

The oedometer loading stiffness, E^{oed} , is determined with the correlation $E_{oed} = (1 - 1.5) * E_{50}$ for normally consolidated sands, coming from previous studies by Schanz and Vermeer (1998). The triaxial unloading stiffness, E^{ur} , is determined with the correlation: $E_{ur} = (4 - 5) * E_{oed}$ (Schanz & Vermeer, 1998). The E_{oed}^{ref} is then equal to E_{50}^{ref} , which is 18557 kPa. The E_{ur}^{ref} is $4 * E_{50}^{ref}$, which gives 74228 kPa.

The rate of stiffness dependency in stiffness behaviour (m) is calculated according to (Brinkgreve, 2018b):

$$\frac{E_{50}^{(1)}}{E_{50}^{(2)}} = \left(\frac{\sigma_3'^{(1)}}{\sigma_3'^{(2)}} \right)^m \Rightarrow m = \frac{\ln(E_{50}^{(1)}/E_{50}^{(2)})}{\ln(\sigma_3'^{(1)}/\sigma_3'^{(2)})} \quad (4.1)$$

$$m = \frac{\ln(20806/18557)}{\ln(150/100)} = 0.3 \quad (4.2)$$

The magnitude of m is normally 0.5 for sands (Brinkgreve, 2018b).

The default parameters are used for the advanced parameters. The advanced parameters are:

- ν_{ur} : Poisson's ratio for unloading-reloading (default: $\nu_{ur}=0.2$)
- p^{ref} : Reference stress for stiffnesses (default: $p^{ref} = 100 \text{ kN/m}^2$) [kN/m^2]
- K^{NC0} : K^0 -value for normal consolidation (default: $K_0^{NC} = 1 - \sin\phi$) [-]
- R_f : Failure ratio q_f/q_a (default: $R_f = 0.9$) [-]
- $\sigma_{tension}$: Tensile strength (default: $\sigma_{tension} = 0$) [kN/m^2]
- c_{inc} : As in Mohr-Coulomb model (default: $c_{inc} = 0$ [kN/m^3])

4.1.3 Parameter optimisation

The Hardening Soil model is examined at element level with the "SoilTest" tool of Plaxis. The experimental test results are compared with the triaxial test results of Plaxis with the initial model parameters. The drained triaxial tests with effective confining pressures 100kPa and 150kPa are used to define and optimise the Hardening Soil model parameters. The results of the parameter optimisation are given in table 4.2. The consolidated drained triaxial test results of the experiments, initial model parameters test results and the optimised model parameters

test results are given in figure 4.3-4.6. The best fit between the Plaxis triaxial test results and experimental test results was sought.

The differences between the optimised and initial model parameters tests results of the deviatoric stress versus axial strain graphs are relatively small. The maximum deviatoric stress peaks of the experiments are not coming back in the model results. Moreover, a better fit was found between the tests with an effective confining pressure of 150kPa than an effective confining pressure of 100kPa.

Parameter	Initial	Optimised	Unit
c	0.0	0.0	kN/m^2
φ	33	33	$^\circ$
ψ	3	3.8	$^\circ$
σ_t	4	4	kN/m^2
E_{50}^{ref}	18557	18560	kN/m^2
$E_{\text{oed}}^{\text{ref}}$	18557	22000	kN/m^2
$E_{\text{ur}}^{\text{ref}}$	74228	90000	kN/m^2
m	0.3	0.6	-

Table 4.2: Initial and optimised Hardening Soil model parameters

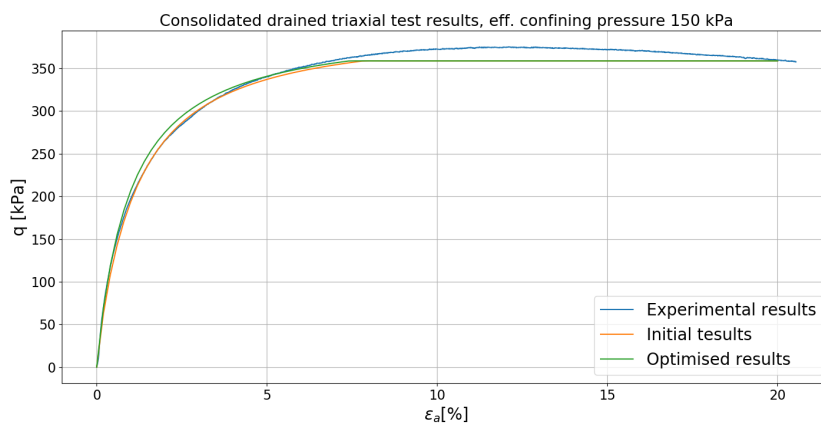


Figure 4.3: Deviatoric stress versus axial strain graphs of the experimental and Hardening Soil model consolidated drained triaxial test results with an effective confining pressure of 150 kPa

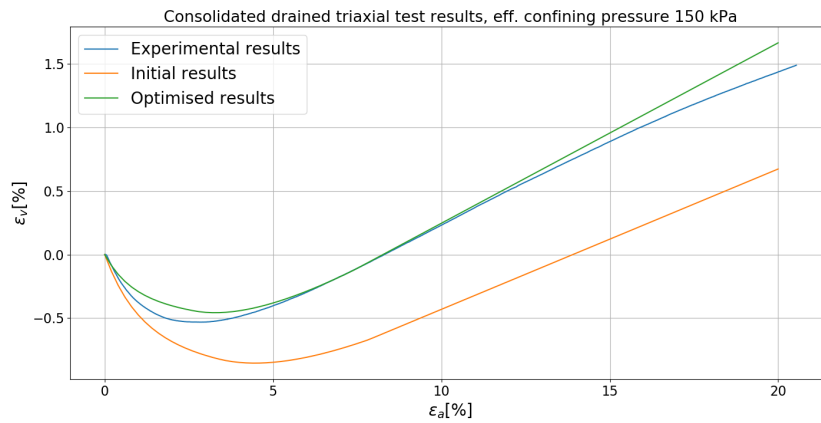


Figure 4.4: Volumetric strain versus axial strain graphs of the experimental and Hardening Soil model consolidated drained triaxial test results with an effective confining pressure of 150 kPa

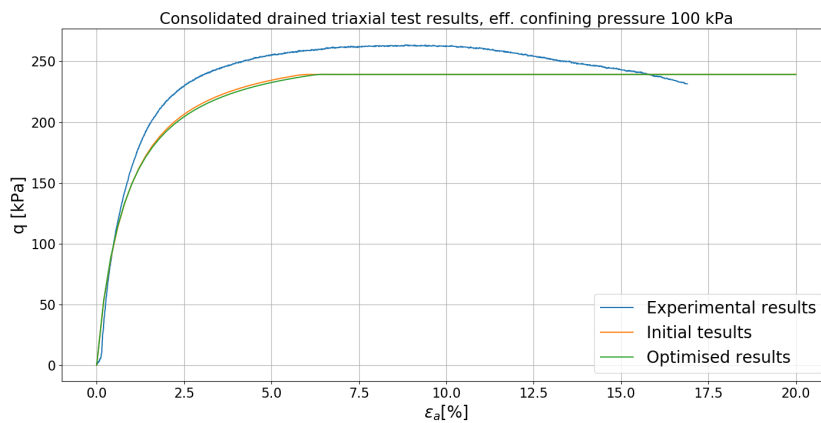


Figure 4.5: Deviatoric stress versus axial strain graphs of the experimental and Hardening Soil model consolidated drained triaxial test results with an effective confining pressure of 100 kPa

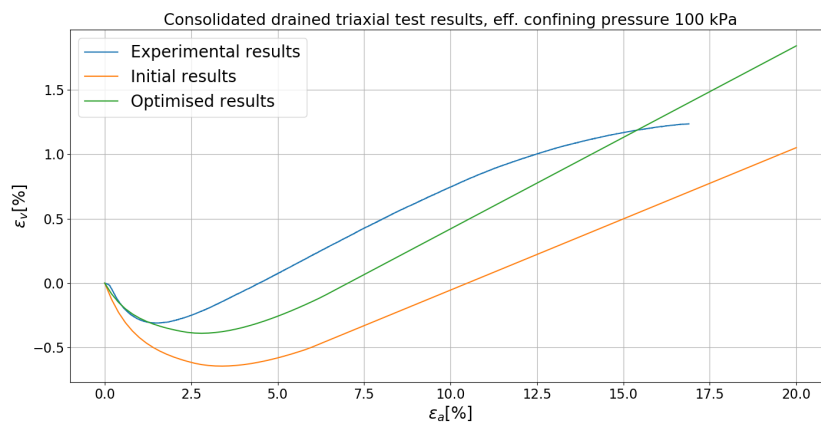


Figure 4.6: Volumetric strain versus axial strain graphs of the experimental and Hardening Soil model consolidated drained triaxial test results with an effective confining pressure of 100 kPa

4.1.4 Analysis calculation results of model 1

The calculation results consist of relative shear stress plots and the stress conditions for a situation with a horizontal bed and a situation after erosion. To select the critical region of a submarine slope, the relative shear stresses are analysed which is an expression of the proximity to the failure line. The relative shear stress (τ_{rel}) is given by (Plaxis, 2019a):

$$\tau_{rel} = \frac{\tau_{mob}}{\tau_{max}} \quad (4.3)$$

Where τ_{mob} is the mobilised shear stress, which is the radius of the Mohr circle and τ_{max} is the maximum shear stress, which is the radius of the Mohr circle with the same centre (M) that touches the failure line (figure 4.7). The results of the relative shear stress are given in figure 4.8.

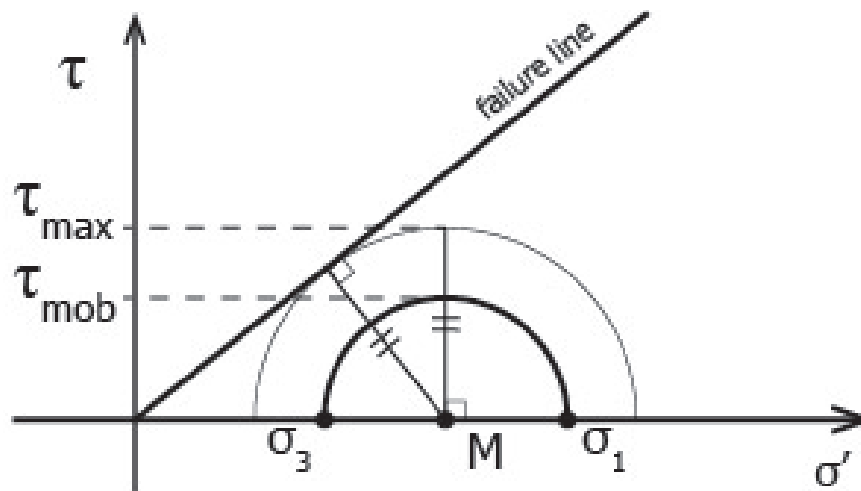


Figure 4.7: Mohr circle with mobilised shear stress (τ_{mob}), maximum shear stress (τ_{max}) and Mohr-Coulomb failure line

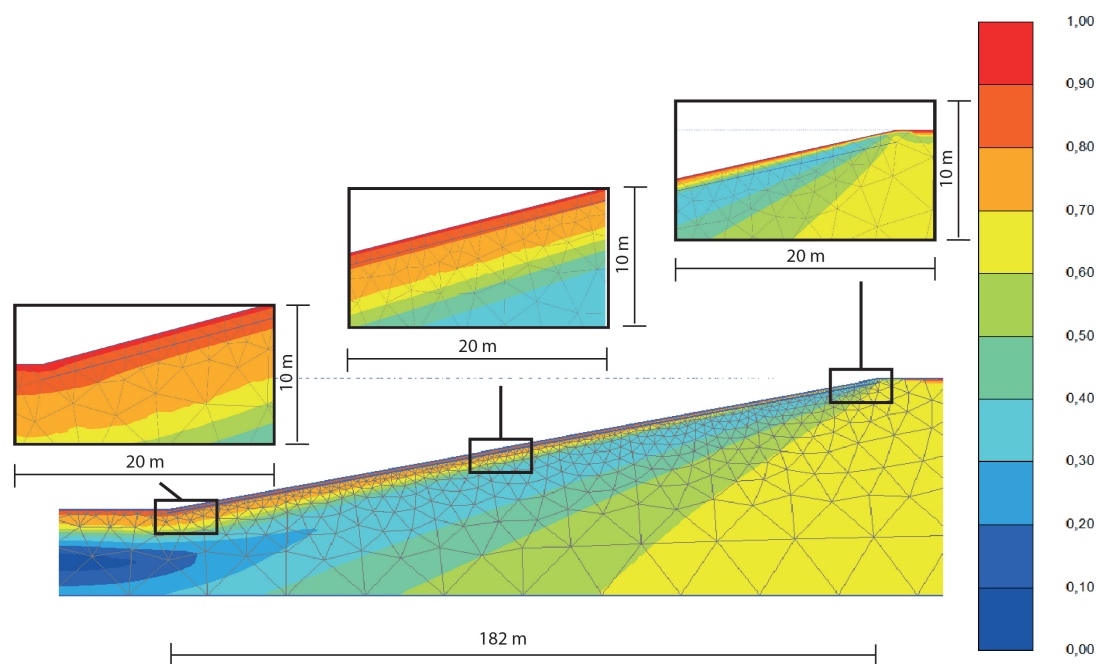


Figure 4.8: Relative shear stress of model 1 for slope 1:5

The relative shear stress is between 0.90 and 1.00 close to the surface (dark red zone). The edges of the 0.90-1.00 zone near the toe are located at the bed and 0.5 meters below the bed. Near the top, these edges are located at the bed and 0.05 below the bed. At 1 meter below the bed, the relative shear stress is between 0.80 and 0.90 from the toe to the centre of the slope. Figure 4.8 shows that the zone with relatively high relative shear stresses (between 0.80-1.00) is decreasing from the toe to the top of the slope. At 1 meter below the bed, near the top, the relative shear stress is between 0.60 and 0.30. The stress conditions of 5 points at 1 meter below the bed are given in table 4.3, with their position in figure 4.9 and their stress states in figure 4.10. The mean effective stress versus deviatoric stress graph shows that the deviatoric stress and mean effective stress are decreasing from points at 1m below the bed from toe to top. The relative shear stress is also decreasing except for the point closest to the top. Moreover, the stress states of the lowest three points are much alike, with a maximum difference of 3kPa.

Characteristics and stress conditions of the stress points at 1 m below the sloping bed						
Stress point nr.	X [m]	Y [m]	Depth [m-bed]	q [kPa]	p' [kPa]	τ_{rel} [-]
19114	51.8	-37.0	1.00	14.8	18.3	0.857
18684	95.7	-28.3	1.02	13.0	16.8	0.816
17793	141.5	-19.7	0.98	11.8	15.7	0.787
19228	187.9	-9.8	1.02	10.0	14.4	0.724
19195	209.8	-5.4	0.97	5.6	11.2	0.532
19151	230.3	-1.3	0.97	3.6	6.2	0.542

Table 4.3: The deviatoric stress and mean effective stress for stress points at 1 m below the bed in phase 2 of model 1 from toe to head

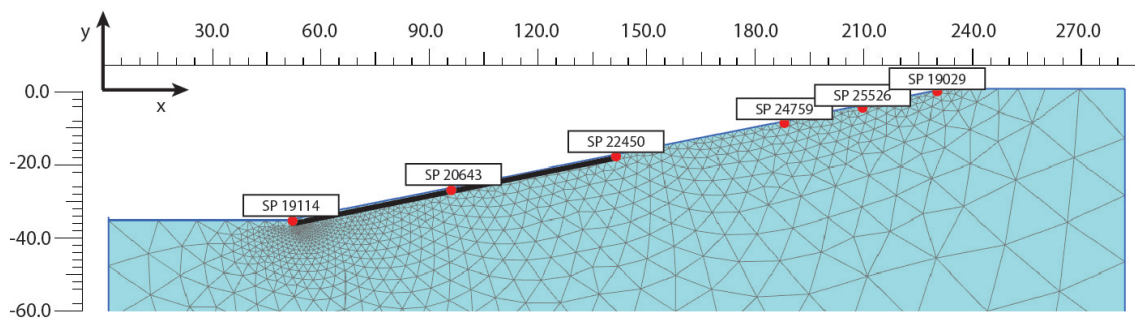


Figure 4.9: Stress points along the slope at approximately 1 meter below the bed

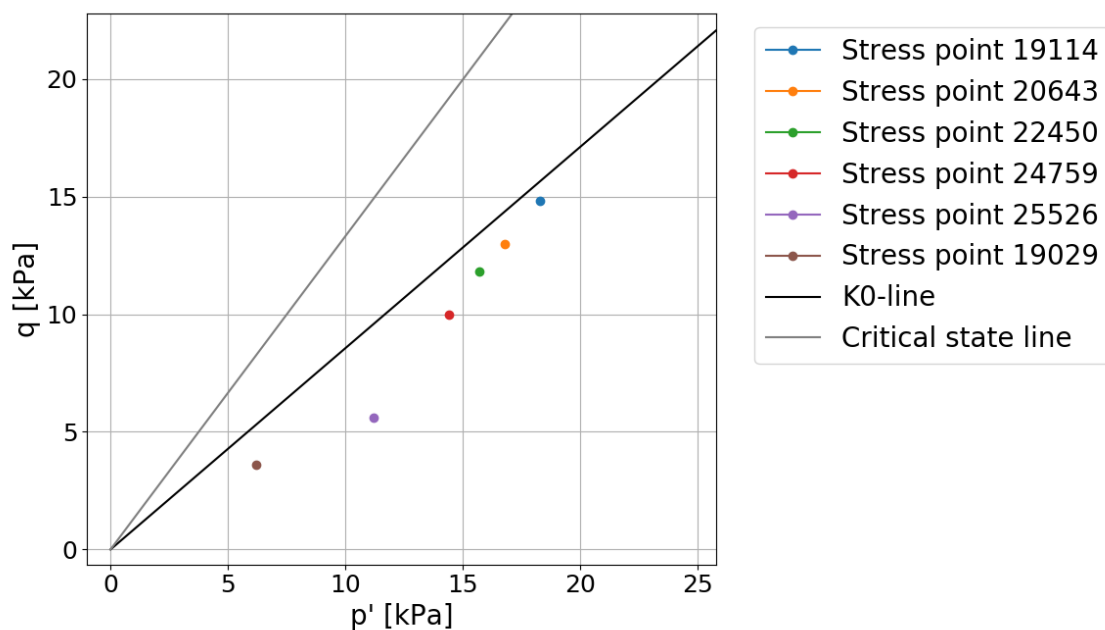


Figure 4.10: Stress state of the selected stress points at 1 meter below the bed in a deviatoric stress versus mean effective stress plane

The selected critical region is depicted in figure 4.9 by a red line. This critical zone is the zone between the toe and centre point of the slope and has a height of 1.7m near the toe and 0.8 at the centre. So, the thickness of the critical region is decreasing from toe to the centre. Because the critical region near the toe is larger than uphill, the critical point is chosen near the toe (nr. 19114).

Moreover, the selection of the critical point is also dependent on the experimental setup conditions. The accuracy of the triaxial test pressure controllers is ± 1 kPa and the setup is less accurate for low pressures. This is another reason why a critical point at 1 meter below the bed is selected.

The largest flow velocities were measured at the deepest point of the scour hole, therefore it is also expected that the pore water pressure fluctuation and seepage pressure are the largest at the deepest point of the slope, so near the toe. Model 2 will show what the influence is of water pressure fluctuation on the excess pore water pressure build-up is.

Discussion model 1

The selected slope ratio, 1:5, is the limit of executing maintenance work (section 2.2.2). However, in the field, also steeper slopes are present that are not failed yet, as shown in section 2.2.2. Therefore, also steeper slopes are modelled in Plaxis, with a ratio of 1:3 and 1:2. The relative shear stress plots are given in figure 4.11. The stress states of the points at 1 meter below the bed near the toe are given in figure 4.12 and table 4.4. The stress conditions of these points are assumed to be relatively similar, with a maximum difference in deviatoric stress of 2.8kPa and a mean effective stress difference of 2.9kPa. This is one of the reasons why solely slope 1:5 is analysed further. However, the relatively high relative shear stress regions are increasing with an increase in slope angle. So, this phenomenon could play a major role in an eventual liquefaction failure of the whole slope, where the instability of 1 point could result in a progression of instabilities.

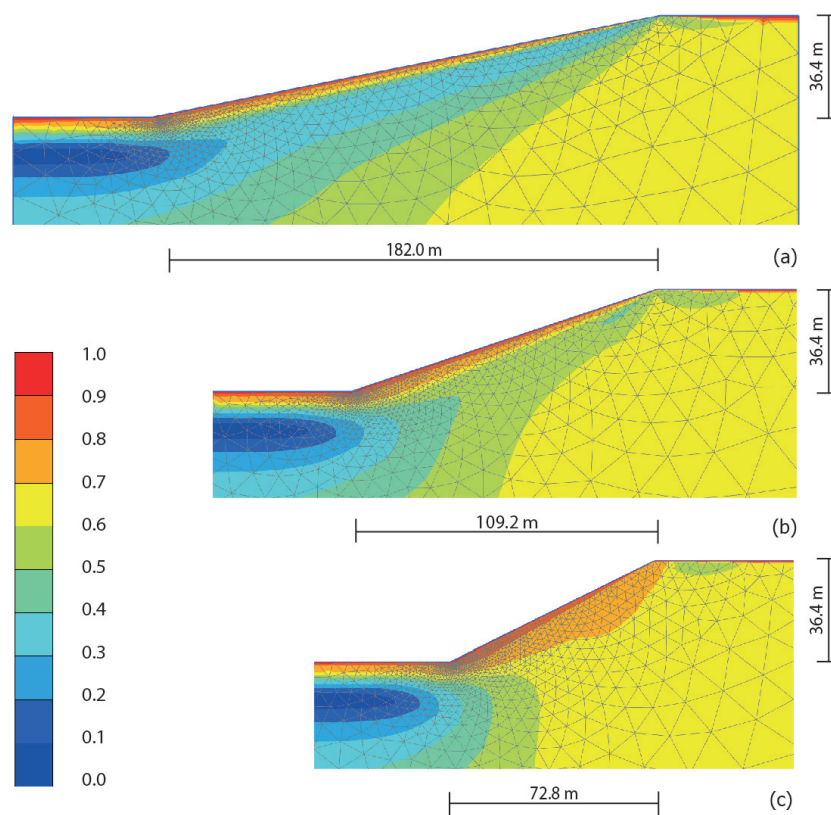


Figure 4.11: Relative shear stress for a slope geometry of 1:5 (a), 1:3 (b) and 1:2 (c) (vertical:horizontal)

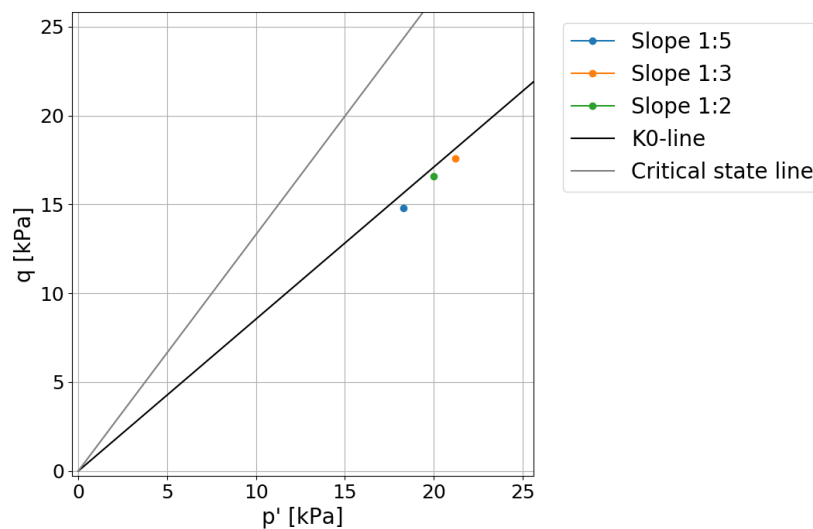


Figure 4.12: Stress state of the selected stress points at 1 meter below the bed for slope 1:5, 1:3 and 1:2 in a deviatoric stress versus mean effective stress plane

Characteristics and stress conditions of the stress points at 1 m below the sloping bed						
Stress point nr.	X [m]	Y [m]	Depth [m-bed]	q [kPa]	p' [kPa]	τ_{rel} [-]
19114	51.8	-37.0	1.00	14.8	18.3	0.857
29352	123.9	-37.1	1.03	17.6	21.2	0.884
31933	159.1	36.9	0.97	16.6	20	0.885

Table 4.4: The deviatoric stress and mean effective stress for stress points at 1 m below the bed for slope 1:5, 1:3 and 1:2

The stress conditions of the critical point 19114 of slope 1:5 are presented in table 4.5. This table shows that the orientation of principal stresses is changing during excavation. The principal stress direction of phase 1 is 0° , which can be simulated with a triaxial compression test. Phase 2 has a principal stress direction of 74.5° . This stress direction cannot be applied with a conventional triaxial test, and can only apply a principal stress direction of 0° (compression test) or 90° (extension test). In this research, the deviatoric stress and mean effective stress values are applied to simulate the stress conditions in a conventional triaxial test setup. However, a hollow cylinder triaxial test could be used to investigate the influence of change in principal stress direction on the test results of the experimental study.

Stress point 19114, element 1593, X = 51.762, Y = -37.047			
Parameter	Unit	Phase 1: Horizontal bed	Phase 2: Slope
σ_1	kN/m ²	919.077	623.679
σ_2	kN/m ²	745.552	623.679
σ_3	kN/m ²	745.552	608.908
p'	kN/m ²	202.922	18.284
p	kN/m ²	803.394	618.755
q	kN/m ²	173.525	14.771
τ_{rel}	-	0.687	0.857
principal stress direction	°	0	74.5

Table 4.5: Stress history of a critical point near the toe at 1 meter below the bed.

4.2 Model 2: Pore pressure change with depth

A critical point is selected with model 2 and the stress history of this point is defined. The following step is to obtain the change in pore water pressure that is generated by the currents at the selected critical point. To perform this step, an estimation of the range of water pressure at the bed is obtained first. The water pressure fluctuation is assumed to be fluctuating harmonically in time. Therefore, frequencies of the water pressure fluctuation are selected. Afterwards, multiple combinations of amplitude and frequency of the water pressure fluctuation at the bed are applied as top boundaries of model 2 and the accumulations of excess pore water pressures are investigated.

In the end, the third sub-question: "What is the range of water pressure accumulation at the bed due to the water flow?" and the fourth sub-question: "What are the stress conditions of a point inside the critical region?" are answered.

4.2.1 Water pressure fluctuation at the bed

A first approximation of the water pressure fluctuation at the bed, that is generated by the water flow on top of the bed, is obtained by an empirical formula. The root mean square of the water pressure (p_w) is given by (Detert et al., 2004):

$$rms(p_w) = C\tau_0 \quad (4.4)$$

With,

$$\begin{aligned} C &= \text{constant} && [-] \\ \tau_0 &= \text{bed shear stress} && [N/m^2] \end{aligned}$$

Experimental studies to the interaction between turbulent open channel flow and flow close to the bed were done by Vollmer and Kleinhans (2007) and Detert et al. (2004) (Vollmer & Kleinhans, 2007) and (Detert et al., 2004). These studies gave a C-value between 0.5 and 5.0 with an average of 3.0. One of the studies was the experimental study of Detert et al (2004). They did measurements in an open channel flume and investigated the influence of an oscillating water level on a nearbed gravel layer. Detert et al. concluded that the mean root square of the pressure variation was: $rms(p_w) = 3.2 * \tau_0$ and that the maximum pressure variation is: $max(p_w) = 18 * \tau_0$.

The bed shear stress is proportional to the shear velocity (u_*) or depth-averaged velocity (U):

$$\tau_0 \sim \rho u_*^2 \sim c_f \rho U^2 \quad (4.5)$$

With,

ρ	= Density of water (997 kg/m ³)	[kg/m ³]
u^*	= Shear velocity	[m/s]
U	= Depth-averaged velocity	[m/s]
c_f	= Friction coefficient	[-]

An approximation of the shear velocity can be obtained by fitting a logarithmic velocity profile to the measured vertical velocity profiles from the ADCP data (section 2.2.3). However, in this study, the bed shear stress is obtained by the depth-averaged velocity and a friction coefficient (c_f) is estimated. The depth-averaged velocities at the deepest ADCP measurement point of 2016 are applied (section 2.2.3). A White-Colebrook formula is used to estimate the friction coefficient (Uijttewaal & Labour, 2019). When the bed is assumed to be rough and ripples are present, a first estimation of the friction coefficient can be determined with:

$$\frac{1}{\sqrt{c_f}} = 5.75 \log \left(\frac{12R}{k} \right) \quad (4.6)$$

With,

R	= Radius (water depth)	[m]
k	= Roughness	[m]

The surface roughness is assumed to be in the order of centimeters. The water depth is approximately 23 meters. This gives a friction coefficient of 10^{-4} . The bed shear stress is approximately 10^{-3} kPa for a maximum mean average velocity of 1.56 m/s. Above empirical formulas give an approximation of the order of magnitude of the water pressure fluctuation, which is between 10^{-2} for the root mean square of the water pressure variation and 10^{-1} kPa for the maximum water pressure variation.

Frequency of the water pressure fluctuation at the bed

The water pressure at the bed is assumed to be fluctuating harmonically in time. A frequency of the water pressure fluctuation is estimated and will be implemented in model 2 to investigate the excess pore water pressure buildup. The measured water flow on top of the bed is a combination of for instance wave-induced currents, tides and vortices which consists of a whole spectrum of frequencies. The measurement interval of the ADCP is 1 min, while the vortices have a frequency in the order of seconds. Therefore, an approximation of the range of frequencies is selected. It is expected that the largest pressures are related to the largest flow velocities and to the largest vortices, which have a wavelength of the present water depth. The frequency of these vortices is given by:

$$f = \frac{U}{\lambda} \quad (4.7)$$

With,

U	= Depth-averaged velocity	[m/s]
λ	= Wavelength	[m]

The wavelength is assumed to be equal to the water depth above the bed protection layer where the formation of the eddies takes place, which is 23 meters. The depth-average velocity is assumed to be in between 2.0 and 2.5 m/s, resulting in a frequency of approximately 0.1 Hz. The maximum frequency cannot be determined with 1-minute velocity data. Therefore, the maximum frequency is assumed to be 1 Hz, which is 10 times larger than the expected minimum frequency.

Discussion estimation water pressure fluctuation

A first approximation of the water pressure fluctuation at the bed is assumed to be in the order of 10^{-2} to 10^{-1} kPa. However, the mean averaged flow velocity is used to define this water pressure at the bed, while the maximum velocities are more relevant to this research because most of the time the extreme situations lead to slope instabilities.

The bed shear stresses are determined by a White-Colebrook type of formula which is valid for a uniform flow at a flat bed, but the effect of bed ripples, a sloping bed and oscillatory flow is unknown. Moreover, Broekema stated that the bed shear stresses are larger than expected because of vertical flow attachment and enhanced contraction (Broekema et al., 2018).

The water pressures at the bed due to the currents has statistical features. The critical flow velocities for slope stability are dependent on the soil response. Therefore, multiplications of the water pressures at the bed are implemented in this research. A list of the combinations of water pressure magnitude at the bed and selected periods ($T = 1/f$) are given in table 4.6.

Water pressure fluctuation at bed level			
Nr.	Characteristic	Amplitude p_w [kPa]	Period p_w [s]
1	1x $p_{w,mv}$	0.1	10
2	1x $p_{w,mv}$	0.1	1
3	10x $p_{w,mv}$	1.0	10
4	10x $p_{w,mv}$	1.0	1
5	100x $p_{w,mv}$	10.0	10
6	100x $p_{w,mv}$	10.0	1
7	1000x $p_{w,mv}$	100.0	10
8	1000x $p_{w,mv}$	100.0	1

Table 4.6: Water pressure (p_w) fluctuation at bed level with, $p_{w,mv}$ as the water pressure determined by the mean velocity

Not only the magnitude of the water pressure at the bed is debatable, but also the selected frequencies. It is assumed that the turbulent flow plays a major role in slope stability near the Eastern Scheldt barrier. This flow has a spectrum of frequencies which could be determined by the inverse Fourier transformation when the logging time is smaller than the period of the flow. So, velocity measurements with a logging time of seconds should be used to give a better approximation of the range of frequencies.

Moreover, the water pressure at the bed is expected to change in time but is assumed to be constant in space. In reality, the horizontal velocity profile in the scour holes is more complex as investigated by Broekema et al. (2018).

The maximum water table is defined with the ADCP data. This is probably not the exact maximum water table, because extreme weather conditions and the position of the moon and sun are not taken into account.

All in all, the water pressure fluctuation at the bed is simplified but for a first analysis of the influence of currents on the behaviour of soil, it is sufficient. However, this uncertainty should be taken into account in the next parts of this thesis.

4.2.2 Model description

The hydro-mechanical coupled behaviour is investigated with model 2. Model 2 is a one-dimensional model consisting of a 20 meters high soil column with a 61.1 meters water column on top (1.7m above NAP). The water column height is the maximum measured water level increase during flood, measured by the ADCP sensor at 59.4 meters below NAP (section 2.2). The combination of water pressure amplitude and period of table 4.6 are applied on the top boundary of the soil column (Y_{MIN}) by fluctuating the hydraulic head (figure 4.13 and table 4.8). The model consists of two phases: one with a constant water table and one with a time-dependent harmonic head (figure 4.13). Model 2 contains 15-node elements with a medium-sized mesh. A UBC3D-PLM soil model is implemented which is an effective stress elastoplastic model that is capable of simulating the generation of pore pressure in undrained behaviour and liquefaction behaviour. The boundaries of model 2 are presented in table 4.7. The model is one-dimensional because it is assumed that the excess pore water pressure can be expelled only in the vertical direction. Moreover, the water pressure change at the bed is considered to be constant in the horizontal plane.

The calculation results of this model are used to define the rate of accumulation of pore water pressure at the depth of the critical point that is defined with model 1.

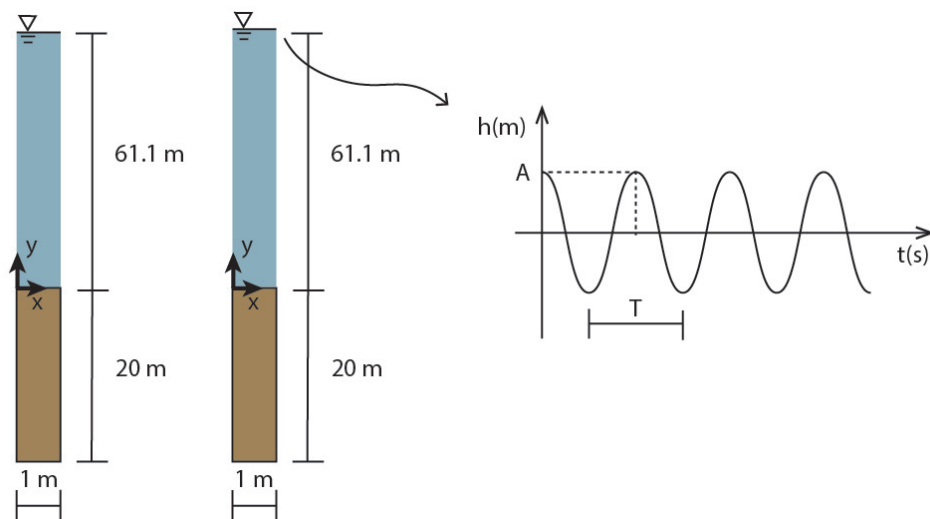


Figure 4.13: Schematic picture of the model 2 phases with A is the amplitude and T is the period of the harmonic hydraulic head fluctuation

Model 2: Pore pressure change with depth			
		Phase 1	Phase 2
Calculation type		K_0 procedure	Fully coupled flow deformation
Deformation boundary condition	X_{MIN}	normally fixed	normally fixed
	X_{MAX}	normally fixed	normally fixed
	Y_{MIN}	fully fixed	fully fixed
	Y_{MAX}	free	free
Groundwater flow boundary condition	X_{MIN}	closed	closed
	X_{MAX}	closed	closed
	Y_{MIN}	open, seepage	open, seepage
	Y_{MAX}	open	open, time-dependent head

Table 4.7: Characteristics of the phases of numerical model 2: pore pressure change with depth

Combination of harmonic head fluctuations at the bed		
Number	Amplitude [m]	Period [s]
1	0.01	10
2	0.01	1
3	0.1	10
4	0.1	1
5	1.0	10
6	1.0	1
7	10.0	10
8	10.0	1

Table 4.8: Combinations of amplitude and period of the harmonic pore pressure fluctuation at the bed based on table 4.6

4.2.3 Model parameters

The parameters of the UBC3D-PLM model are listed below (Plaxis, 2019b).

The stiffness parameters are:

- k_B^{*e} : Elastic bulk modulus factor [-]
- k_G^{*e} : Elastic shear modulus factor [-]
- k_G^{*p} : Plastic shear modulus factor [-]
- me : Rate of stress-dependency of elastic bulk modulus [-]
- ne : Rate of stress-dependency of elastic shear modulus [-]
- np : Rate of stress-dependency of plastic shear modulus [-]
- p_{ref} : Reference pressure [kN/m²]

The strength parameters are:

- φ_{cv} : Constant volume friction angle [°]
- φ_p : Peak friction angle [°]
- c : Cohesion [kN/m²]
- σ_t : Tension cut-off and tensile strength [kN/m²]
- f^{dens} : Densification factor [-]

f^{Epost} : Post-liquefaction factor [-]

The advanced mode parameters are:

R_f : Failure ratio [-]

$(N_1)^{60}$: SPT value [-]

f^{dens} : Densification factor [-]

f^{Epost} : Post-liquefaction factor [-]

To get a first-order approximation of the model parameters for the UBC3D-PLM model, empirical formulas are applied. The stiffness modulus factors can be calculated with the normalised N_{SPT} value, $(N_1)_{60}$ for the generic initial calibration. Because the $(N_1)_{60}$ is unknown, the following approximation with relative density RD (in %), which is equal to 30%, can be used (Plaxis, 2019b):

$$(N_1)_{60} \approx \frac{RD^2}{15^2} = \frac{30^2}{15^2} = 4 \quad (4.8)$$

The minimum $(N_1)_{60}$ value for the model is 5, therefore this minimum value is used as input value for the model. However, the elastic and plastic modulus factors are calculated with a $(N_1)_{60}$ value of 4.

The proposed equations for the generic initial calibration are the following (Plaxis, 2019b):

$$k_G^{*e} = 21.7 * 20 * (N_1)_{60}^{0.3333} = 688.9 \quad (4.9)$$

$$k_B^{*e} = 0.7 * k_G^{*e} = 482.2 \quad (4.10)$$

$$k_G^{*p} = k_G^{*e} * (N_1)_{60}^2 * 0.003 + 100 = 133.1 \quad (4.11)$$

The index parameter m_e , n_e and n_p are calibrated by curve fitting, the range of these values is 0 - 1 (Plaxis, 2019b). The suggested default values were used for the generic initial calibration, which are $m_e = n_e = 0.5$ and $n_p = 0.4$.

The critical friction angle is 33° , as described in section 3.1.1. Soil characterisation. The peak friction angle is derived by:

$$\phi_p = \phi_{cv} + \frac{(N_1)_{60}}{10} + \max(0; \frac{(N_1)_{60} - 15}{5}) = 33.4 \quad (4.12)$$

4.2.4 Parameter optimisation

The UBC3D-PLM model is examined at the element level to evaluate whether similar soil responses can be reproduced as observed in triaxial tests. A proper way to extract the parameters for the UBC3D-PLM model is by using cyclic triaxial or cyclic direct simple shear tests (Plaxis, 2019b). In this case, only data from drained and undrained triaxial tests are available. The validation of the UBC3D-PLM model is accomplished by using the element test tool in the Plaxis software and by comparing the results with the available pore pressure versus axial strain undrained triaxial test results. The initial model parameters and the optimised model parameters are given in table 4.9 and the optimised model parameters test results are given in figure 4.14-4.16.

Parameter	Initial	Optimised	Unit
k_B^{*e}	482.2	532.8	-
k_G^{*e}	688.9	425.0	-
k_G^{*p}	133.1	971.3	-
me	0.5	0.6	-
ne	0.5	0.3	-
np	0.4	0.6	-
φ	33	33	$^\circ$
φ_p	33.4	34.5	$^\circ$

Table 4.9: Initial and optimised UBC3D-PLM model parameters

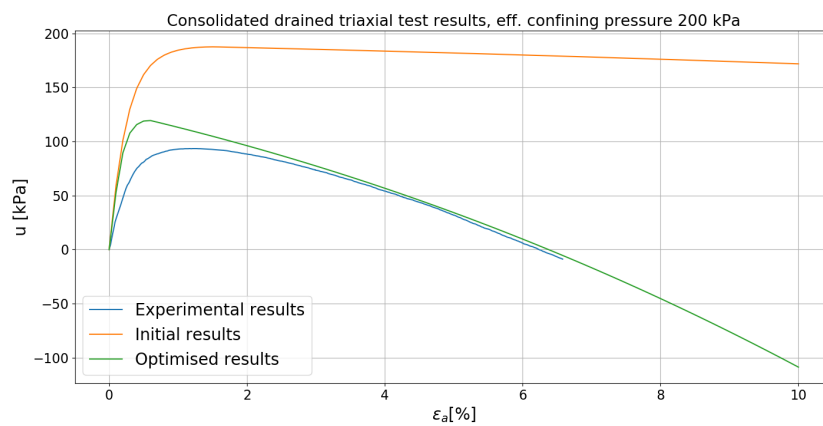


Figure 4.14: Pore water pressure versus axial strain graphs of the experimental and UBC3D-PLM model consolidated undrained triaxial test results with an effective confining pressure of 200 kPa

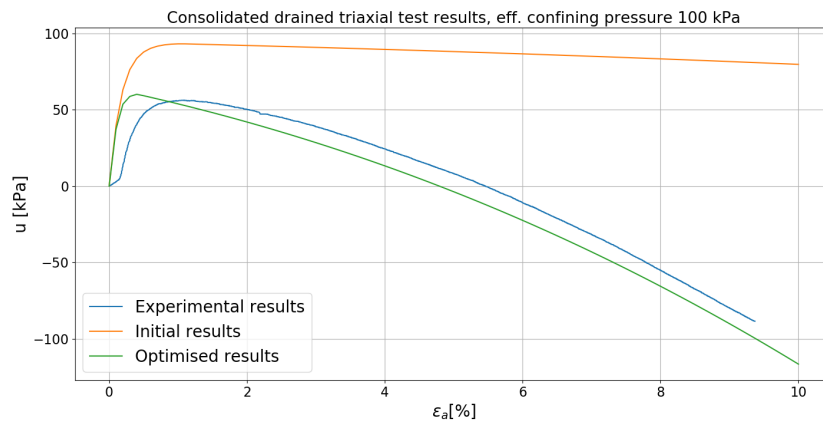


Figure 4.15: Pore water pressure versus axial strain graphs of the experimental and UBC3D-PLM model consolidated undrained triaxial test results with an effective confining pressure of 100 kPa

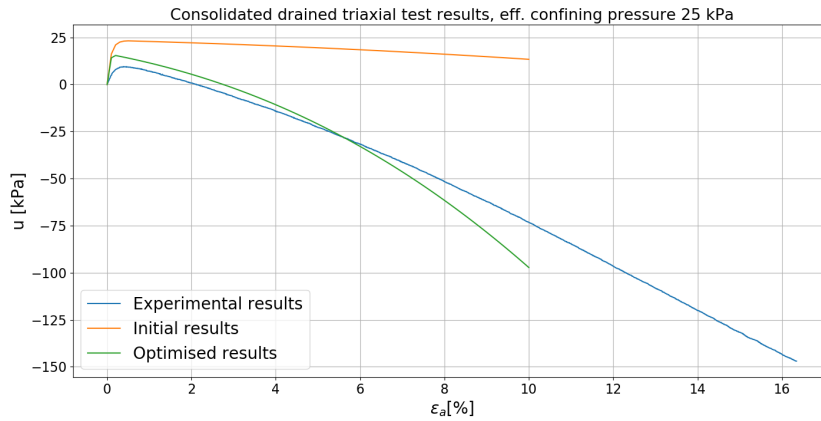
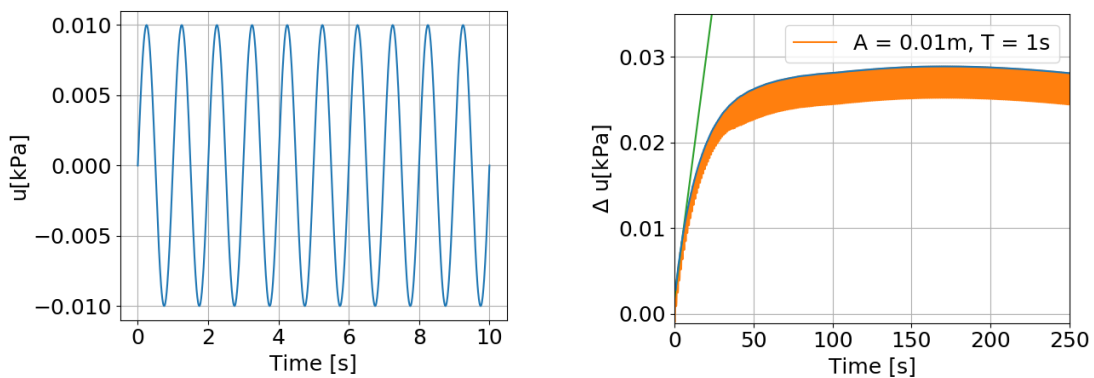


Figure 4.16: Pore water pressure versus axial strain graphs of the experimental and UBC3D-PLM model consolidated undrained triaxial test results with an effective confining pressure of 25 kPa

4.2.5 Analysis calculation results of model 2

The maximum rate of the excess pore water pressure build-up is defined. The steady-state pore water pressure at 1mm below the bed is 621kPa. The excess pore water pressure at 1 meter below the bed versus time graph for combination 2 (figure 4.17a) is given in figure 4.17b in orange. The results of the additional combinations are given in figure H.1 of appendix H. In this research, the build-up is simplified as a linear increase while the build-up in excess pore water pressure is non-linear in reality due to non-linear consolidation. During consolidation, the porosity of the soil changes. The blue line is going through the maxima of the orange harmonic fluctuation (figure 4.17b). The maximum pore pressure increase is assumed to be the tangent of the line through the first and fifth point of the blue line in figure 4.17b. The results of the maximum rate of excess pore water pressure increase show that the rate of excess pore water pressure is increasing with a decreasing period and increasing amplitude are given (table 4.10).



(a) Water pressure at bed level versus time

(b) Excess pore water pressure at 1 meter below the bed versus time with the maximum rate in green, fluctuation in orange and maximum buildup in blue

Figure 4.17: The rate of excess pore water pressure build up of combination 2 for a harmonic head at the bed with an amplitude of 0.01m and a period of 1

Max. rate of pwp. accumulation of harmonic head fluctuations at 1m below the bed			
Number	Amplitude [m]	Period [s]	Δu [kPa/s]
1	0.01	10	0.00005
2	0.01	1	0.0014
3	0.1	10	0.0005
4	0.1	1	0.0112
5	1.0	10	0.0030
6	1.0	1	0.0866
7	10.0	10	0.0220
8	10.0	1	0.5069

Table 4.10: The maximum rate of excess pore water pressure accumulation for harmonic head fluctuations at 1 meter below the bed

4.3 Conclusions on model results

Model 1 answers the sub-question: "Which part of the slope is more prone to become unstable (critical regions)?". The critical elements are considered to have a relative shear stress between 0.8 and 1.0. The critical region of these elements is located close to the sloping bed and the region is larger at the deepest part of the slope. Therefore, a critical soil element was selected close to the toe of the slope, at 1 meter below the sloping bed. A slope with a 1:5 ratio is selected to investigate further because the differences in stress conditions of a point near the toe are relatively small.

Sub-question: "What is the range of water pressure accumulation of the bed due to the water flow"? is answered as well. An empirical correlation of bed shear stress and water pressure is applied to obtain a first approximation of the order of magnitude of water pressures at the bed. The bed shear stress is defined by the averaged flow velocity at the deepest ADCP measurement point. This point is selected because previous research into the flow velocity profile of the Eastern Scheldt barrier area showed a slight increase in velocity with scour hole depth (Broekema et al., 2018). So, an averaged flow velocity is applied to define the water pressure while the extreme values are expected to be significant for initiating instabilities. Therefore multiplications of the water pressures at the bed are implemented in the finite element model.

Moreover, sub-question: "What are the stress conditions of a point inside the critical region?", can be answered with model 1 and 2. The selected point is located at 1 meter below the sloping bed.

First, at time $t = 0$, a the point is located at the bed:

$$\begin{aligned} t &= t_0 \\ u &= 601 \text{ kPa} \\ p' &= 0 \text{ kPa} \\ q &= 0 \text{ kPa} \end{aligned}$$

Second, a sedimentation phase takes place:

$$\begin{aligned} t_0 &\rightarrow t_s \\ u &= 601 \text{ kPa} \\ p' &= 618.7 \text{ kPa} \\ q &= 18.3 \text{ kPa} \end{aligned}$$

Afterwards, an excavation was done:

$$\begin{aligned} t_s &\rightarrow t_e \\ u &= 601 \text{ kPa} \\ p' &= 618.8 \text{ kPa} \\ q &= 18.3 \text{ kPa} \end{aligned}$$

The excavation is representing erosion and scour development.

The stress history of the selected critical point is presented by a stress path plot, figure 4.18. The stress path starts in the origin. Then, the stress path is following the K0-line, after which the unloading starts that results in a stress state just below the K0-line.

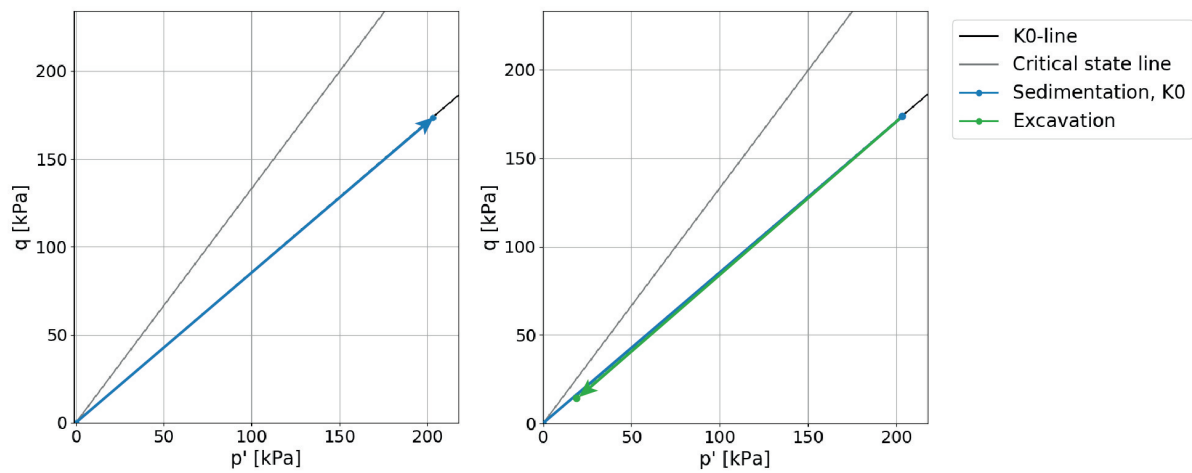


Figure 4.18: Stress history of critical point near toe with slope 1:5

The last stage is when the soil is subjected to currents. The currents are simulated by a harmonically time-dependent water pressure change at the bed. The maximum rates are defined in table 4.10. The results of this chapter are applied in the experimental study.

5 | Experimental study

This chapter elaborates on the experimental part of this thesis. Triaxial experiments are selected for the experimental study because all the field stresses can be simulated and controlled in this setup. The main goal of these tests is to get more insight into the soil behaviour of sand that is subjected to pore water pressure accumulation. In particular, the instability of the soil is investigated. Because the occurrence of liquefaction flow slides is preceded by the occurrence of an instability (Molenkamp, 1989).

First, the experimental program is reported, including the test plan. The test plan is based on the static and dynamic analysis performed with Plaxis 2D of chapter 4. Advanced triaxial tests are done in which the back pressure is increased linearly with the predefined rates of chapter 4. This increase in back pressure is representing the build-up of pore water pressure due to the currents at the scour holes near the Eastern Scheldt barrier. The materials of the experimental study are already discussed in chapter 3. Second, the test results are presented and discussed. At the end of this chapter, the conclusion is given and the last sub-question is answered (section 1.3). The uncertainties of the triaxial test measurements are given in appendix I.

5.1 Experimental program

The triaxial tests of this study are advanced triaxial tests in comparison to the conventional triaxial tests. In these tests, the pore water pressure is gradually increased by the back pressure controller, while the setup is trying to sustain the axial load and radial stresses to attain quasi-steady constant deviatoric stress path tests. The pore water pressure is gradually increased to endeavour the stress conditions representative of those in situ. The location of the critical state line is checked by an anisotropically consolidated undrained conventional triaxial test.

The triaxial tests are performed with the aforementioned experimental setup of the soil characterisation tests (subsection 3.1.1). Moreover, the tested soil, sample preparation method and saturation stage are equivalent to those of the soil characterisation tests. The saturation phase is followed by a docking phase, in which the base is raised until the top cap is touching the load cell piston.

The stress history is applied to the advanced triaxial test samples by three stages. After saturation, the effective stress is 10 kPa and the normal stresses are increased under drained conditions until the K_0 -line is reached ($K_0 = 0.46$). The next stage represents the sedimentation in the field by loading the triaxial sample while following the K_0 -line in q - p' space under drained conditions. The last stress history stage is representing the erosion and formation of the scour holes in the field which is simulated by unloading the sample under drained conditions until the stress state is reached that was selected in chapter 4, for a K_c of 0.48 ($q = 14.8$ kPa and $p' = 618.8$ kPa).

The stress history stages are followed by the shearing phase of the constant shear tests. In this phase, the back pressure is linearly increased until the sample fails. During the shearing phase, the triaxial setup is trying to recover the axial force by adjusting the base height to a constant value. The triaxial setup is trying to keep the cell pressure constant as well. The applied back pressure rates are shown in the test plan (table 5.1) that is based on the maximum pore water pressure accumulation rates of chapter 4. For one back pressure rate, three tests were done to

investigate the reproducibility of the tests.

Advanced triaxial test plan				
Nr.	BP rate [kPa/s]	B-value [-]	e_{au} [-]	RD_{au} [%]
1	0.0014	0.96	0.955	27
2	0.0030	0.96	0.949	28
3	0.0112	0.93	0.964	25
4	0.0220	0.93	0.972	23
5	0.0866	0.92	0.969	23
6	0.0866	0.97	0.982	21
7	0.0866	0.96	0.946	29
8	0.5069	0.96	0.970	23

Table 5.1: Test plan with back pressure (BP) rate, B-value after saturation, void ratio after unloading (e_{au}) and relative density after unloading (RD_{au})

After the constant shear tests, an undrained triaxial test was performed in addition to the undrained triaxial tests of the soil characterisation (chapter 3) to check the position of the critical state line. This undrained triaxial test was an anisotropically consolidated triaxial test for an effective confining pressure of 18.8 kPa and a stress ratio of 0.787 (q/p').

5.2 Triaxial test results and discussion

5.2.1 Principal stresses and pore water pressure versus time

The measured stresses, including the back pressure, pore water pressure, radial stress and axial stress, are plotted versus time in figure 5.1. The back pressure is increased linearly for 6 different rates. The graphs show that the back pressure (σ_{BP}), which is measured at the top, and pore water pressure (u), which is measured at the bottom, are overlapping, except for test 2 and 6. The differences between the back pressure and pore water pressure are discussed and plotted versus time in appendix J. One of the reasons for the deviation of the back pressure and pore water pressure of test 2 could be inhomogeneity of the sample or an incorrect offset.

At the start of the test, the back pressure and pore water pressure are increasing at the given rate until a point is reached at which the setup is not able to continue the increase of back pressure anymore. Then, the differences in pore water pressure and axial stress are expected to be too small, resulting in an increase in cell pressure.

At the start of the test, the cell pressure is set constant, but during the linear increase in back pressure, the cell pressure (σ_r) is slightly increasing for test 3, 4, 6 and 8. Moreover, the increase is larger for higher back pressure rates. However, the total increase is relatively small (< 3 kPa). The development of stresses and pore water pressure is divided into three parts, which will be discussed later.

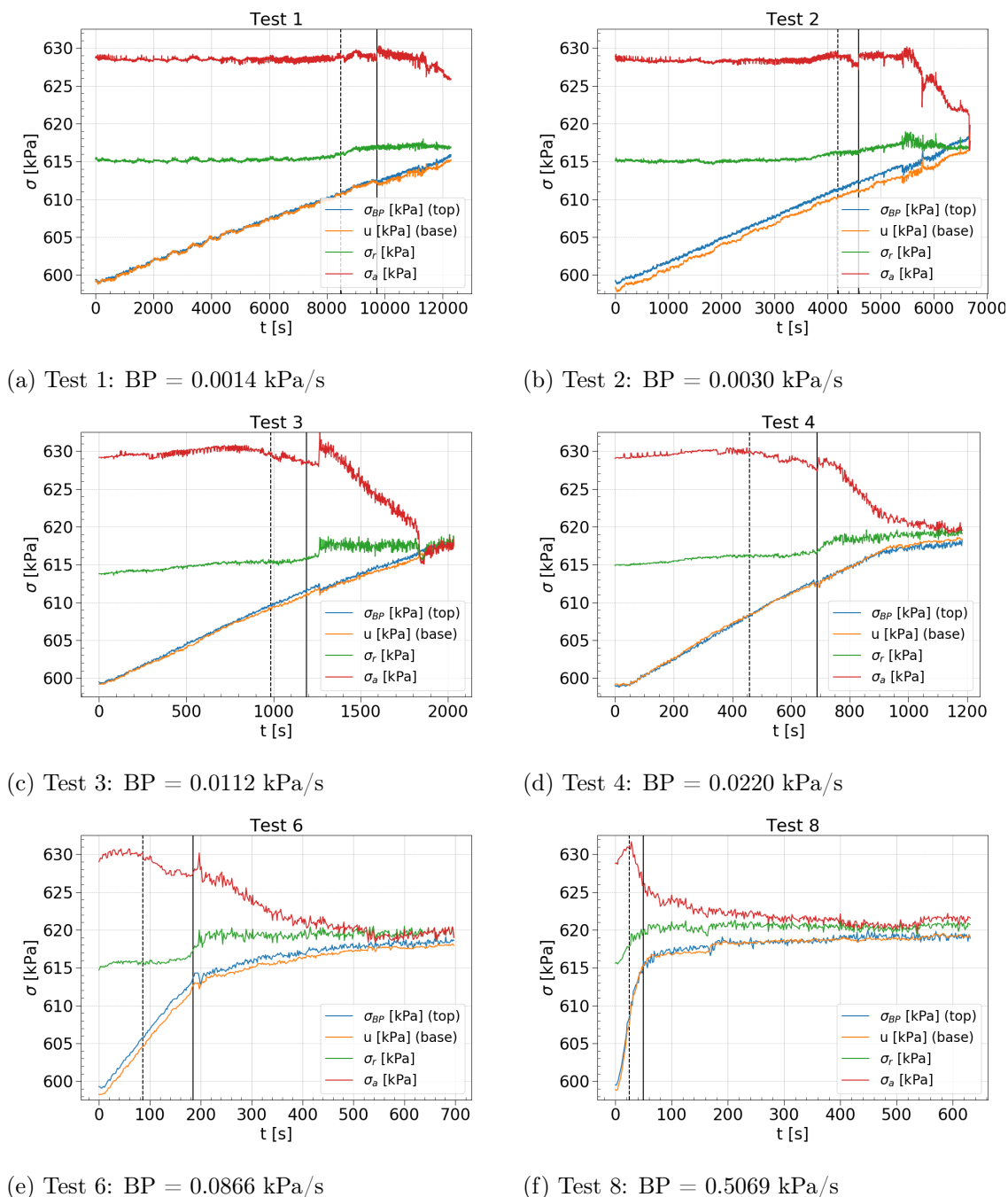


Figure 5.1: The back pressure, pore water pressure, radial stress and axial stress versus time of the advanced triaxial tests with increasing back pressure rate. The dotted black line is presenting the point at which the deviatoric stress drops and the solid black line is the first point of rapid deformation.

5.2.2 Effective stress path

The effective stress paths are presented in figure 5.2. The direction of the stress paths is from maximum mean effective stress to the minimum value. The mean effective stress is decreasing while the pore water pressure is increased by the back pressure controller. The interesting stress path parts are the paths with constant deviatoric stress and the point at which the deviatoric

stress is decreasing. At this turning point, which is depicted by a star (see appendix K), it is expected that the load cannot be carried by the sample anymore. If this expectation can be confirmed will be discussed with the strains versus time graphs. After this turning point, the back pressure is still increasing and the triaxial setup is trying to sustain the radial stress and axial force at the start of the test. So, after the drop in deviatoric stress, the controllers are influencing the measured response.

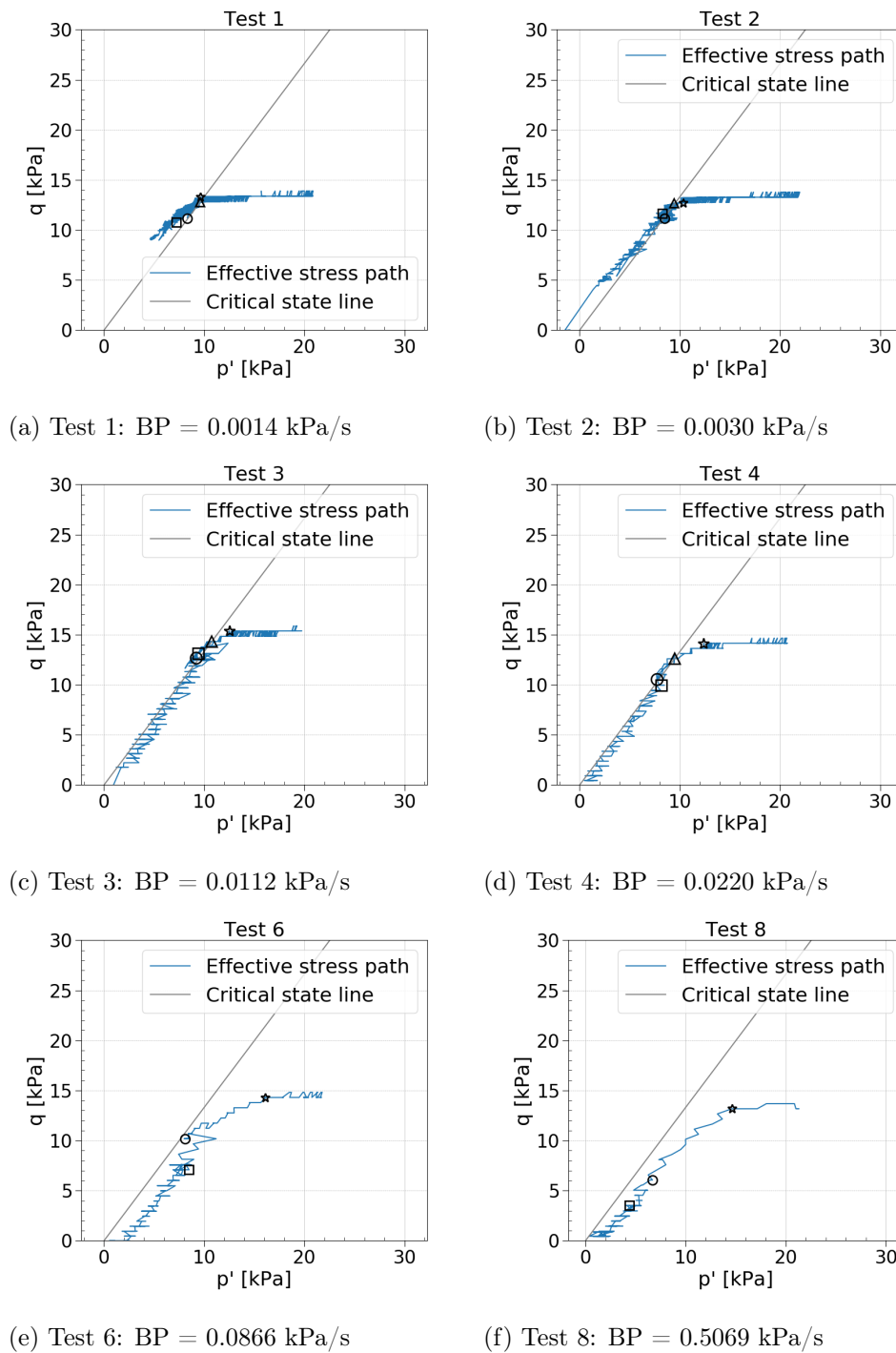


Figure 5.2: Effective stress paths of the advanced triaxial tests

5.2.3 Determination turning points

Multiple turning points are determined for the triaxial test data. Some points are based on the axial strains and some are based on the load cell measurements. A list of the selected points is given in table 5.2. Each of these points is discussed in this section.

Symbol	Characteristic
☆	Point of the drop in deviatoric stress
△	Point of reaching the critical state stress ratio (M)
○	First point of formation of rapid strains
□	Second point of formation of rapid strains

Table 5.2: List of the turning points and their characteristics for the advanced triaxial tests

The point that is depicted by a black star is the point at which the deviatoric stress starts to drop. Appendix K elaborates on the selection of these points. The stress states at this turning point are plotted versus the pore water pressure ratio in figure 5.3. The uncertainties of appendix I are taken into account. The uncertainty of the test with a back pressure rate of 0.0866kPa/s is smaller than the other tests because this test is repeated two times. A power function is plotted through the results ($y = 0.7737x^{-0.088}$) indicating a decrease in stress ratio for an increase in pore water pressure rate. It seems like the test results are going to an asymptote for increasing pore water pressure rate.

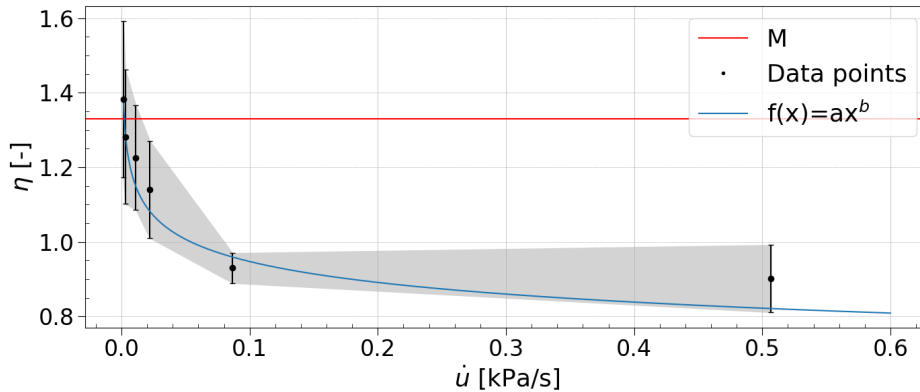


Figure 5.3: The stress ratio versus rate of pore water pressure with the critical state stress ratio in red, the data points in black including the uncertainties and a fitted power function in blue

Another turning point is selected by looking at the critical state line. A point is defined at which the critical state line is reached or crossed for the first time. This point is defined by the stress ratio ($\eta=q/p'$) versus time graphs and depicted by a triangle (appendix L). Sample 1, 2 3 and 4 are passing the M line, which is the stress ratio of the critical state line, while test 7 and 8 are not even touching the line. Test 3 and 4 show data gaps due to 0 deviatoric stress.

The other two turning points are selected based on the axial strains, as shown in figure 5.4. This figure presents a faster increase in axial strain for higher back pressure rates and relatively low axial strains ($< 2\%$). The graphs show 2 sharp increases in axial strain for every test, which is best noticeable in the results of test 1 and test 2 of figure 5.4. After the last sharp increase, the rate of axial strain is equal and constant for all tests. The rate of axial strain is determined by

a gradient function of numpy. This function uses the central differences method to calculate the gradient as presented in figure 5.5. The onset of rapid deformation is defined by the gradient of the axial strain versus time data. This data shows that the base of the setup is controlled by a feedback control system with fixed step sizes. If the measured load cell value is too high then the base is lowered to assure a decrease in axial load. In these graphs, two zones are determined in grey and white. Deformation starts when the data points will pass the first grey zone (0.0 to 0.0050%/s gradient), which is depicted by a circle in the following plots. When the rate of axial strain will pass the white zone (0.0050%/s to 0.0284%/s gradient), the maximum rate of axial strain is reached, which is depicted by a square in the following graphs.

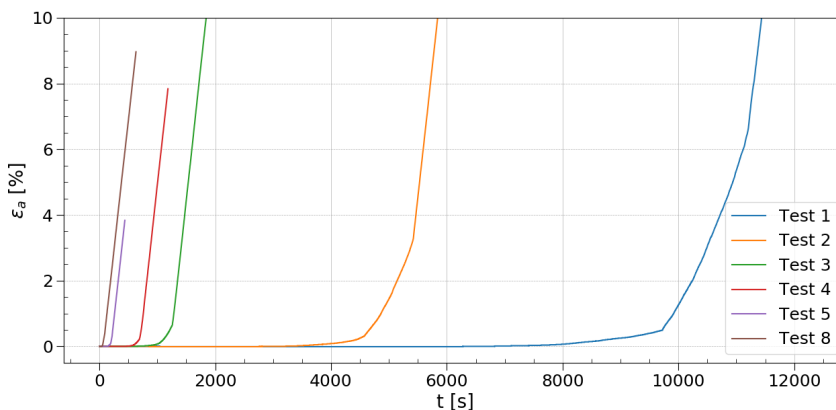


Figure 5.4: Axial strain versus time graphs for the advanced triaxial tests

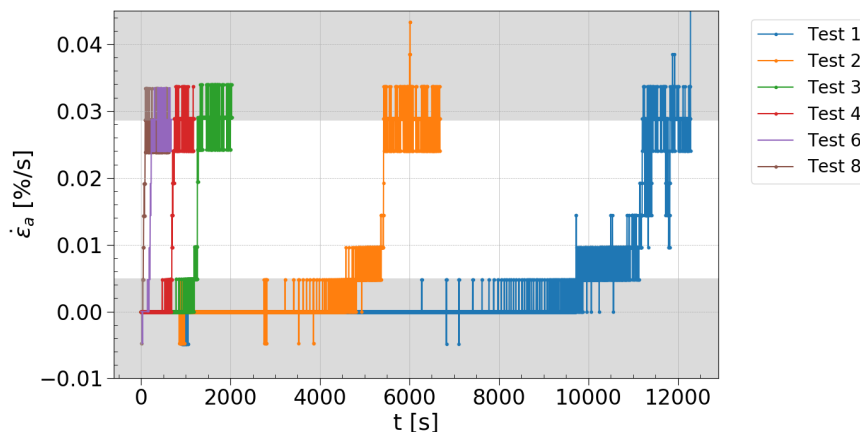


Figure 5.5: Gradient of axial strain versus time for the advanced triaxial tests

5.2.4 Axial and volumetric strains versus time

The axial strains and volumetric strains are plotted against time in figure 5.6 including the predefined turning points. The axial and volumetric strains are calculated taking the strains after unloading as zero axial strain. The turning points of rapid strains (circles and squares) are exactly located on the points where the sharp increases are located. The critical state ratio is reached earlier than the sharp increases of axial strain except for test 6. The samples are dilating during the back pressure increase. The axial strains corresponding to the turning points of the drops in deviatoric stresses, indicated by stars are listed in table 5.3. The measured axial strains

at the drop in deviatoric stresses are assumed to be negligible. It appears that the load cell is not capable of preserving the axial load. A minor displacement will already lead to a decrease in axial load which results in a decrease in deviatoric stress.

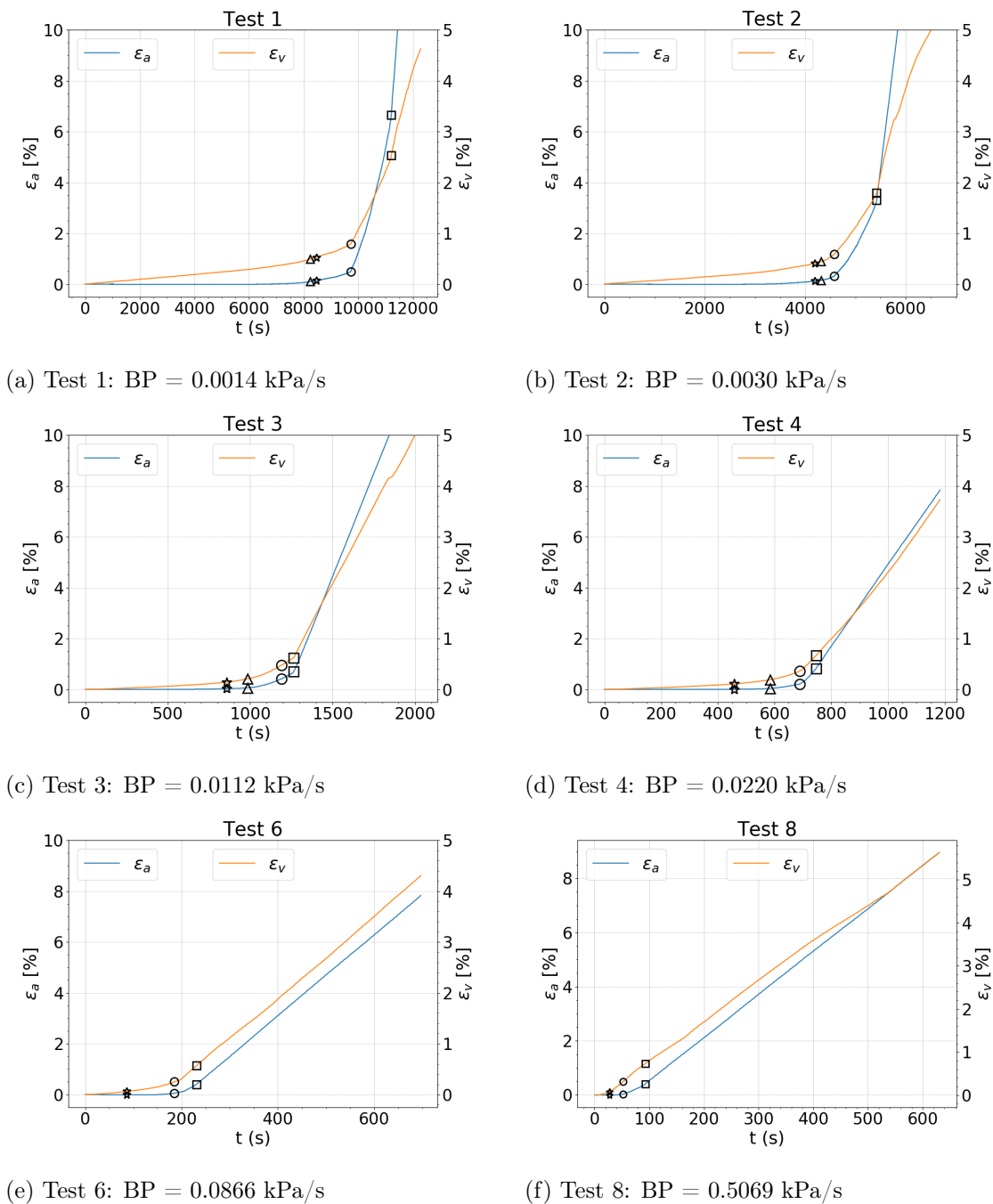


Figure 5.6: Axial and volumetric strain versus time of the advanced triaxial tests

Test	1	2	3	4	5	6	7	8	
$\dot{\epsilon}_v$	0.0014	0.0030	0.0112	0.0220	0.0866	0.0866	0.0866	0.5069	kPa/s
ϵ_a	0.14	-0.14	0.03	0.00	0.00	-0.01	-0.01	-0.01	%

Table 5.3: The axial stain at the drop in deviatoric stress of the advanced triaxial test

Figure 5.7 shows the rate of axial strain versus time with the defined turning points and a moving average calculated for 30 measurement points. After reaching the "star" point, the axial strain rate is increasing, but a turning point between the start of the decrease in deviatoric stress and rapid increase indicated by a circle cannot be defined. It seems, by looking at the grey line, that the rate of increase is going in steps of 0.005 %/s this is equivalent to approximately 0.5 mm/s.

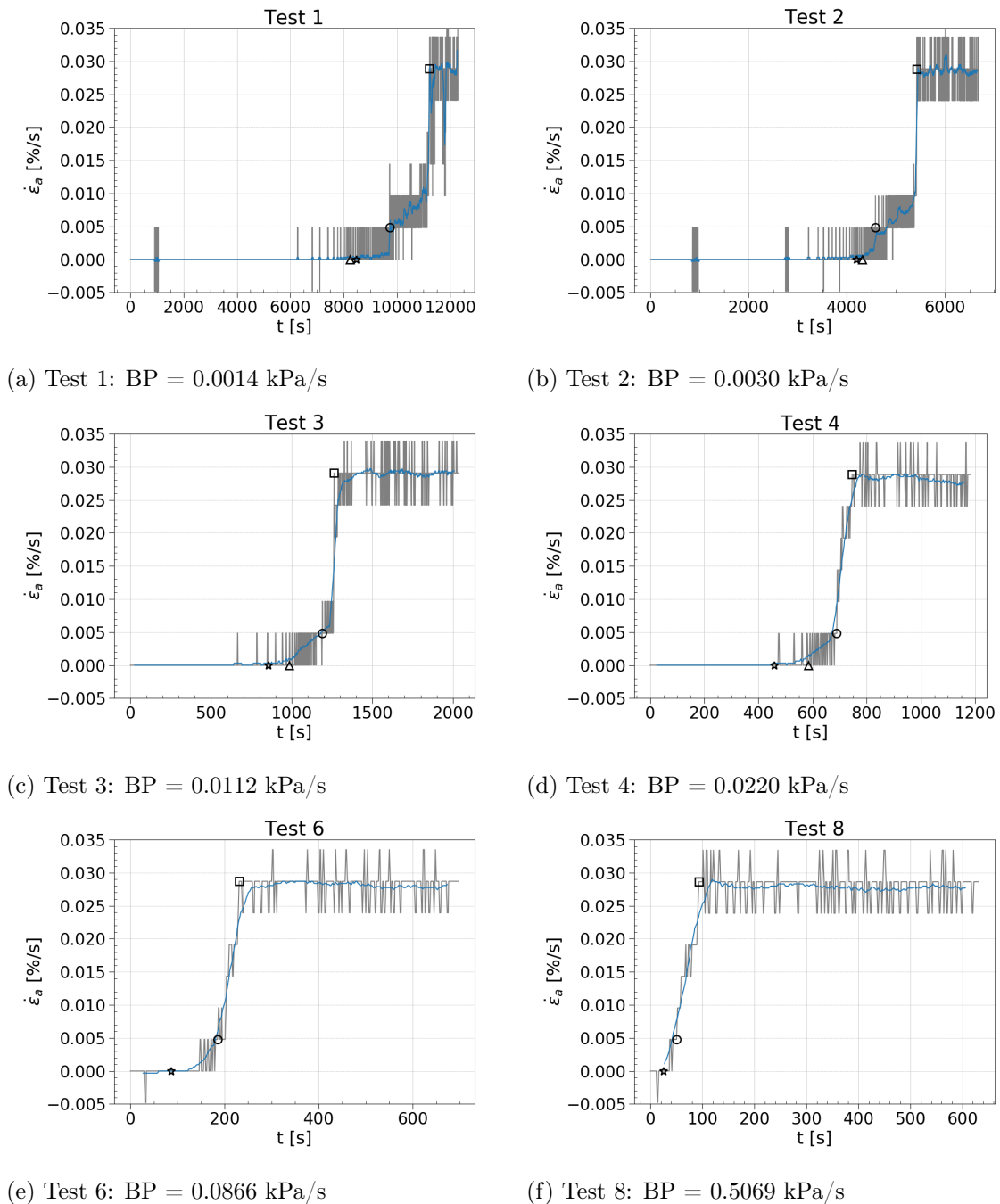


Figure 5.7: Rate of axial strain versus time of the advanced triaxial tests with a moving average of 30 points in blue

The steps of axial strain rate can be explained by the load cell. The load cell has an accuracy of 0.001kN (appendix I) which is equal to approximately 0.52kPa on the sample surface. The

base of the setup is responding on the load cell measurements, so the accuracy of the axial displacements are depending on the load cell accuracy.

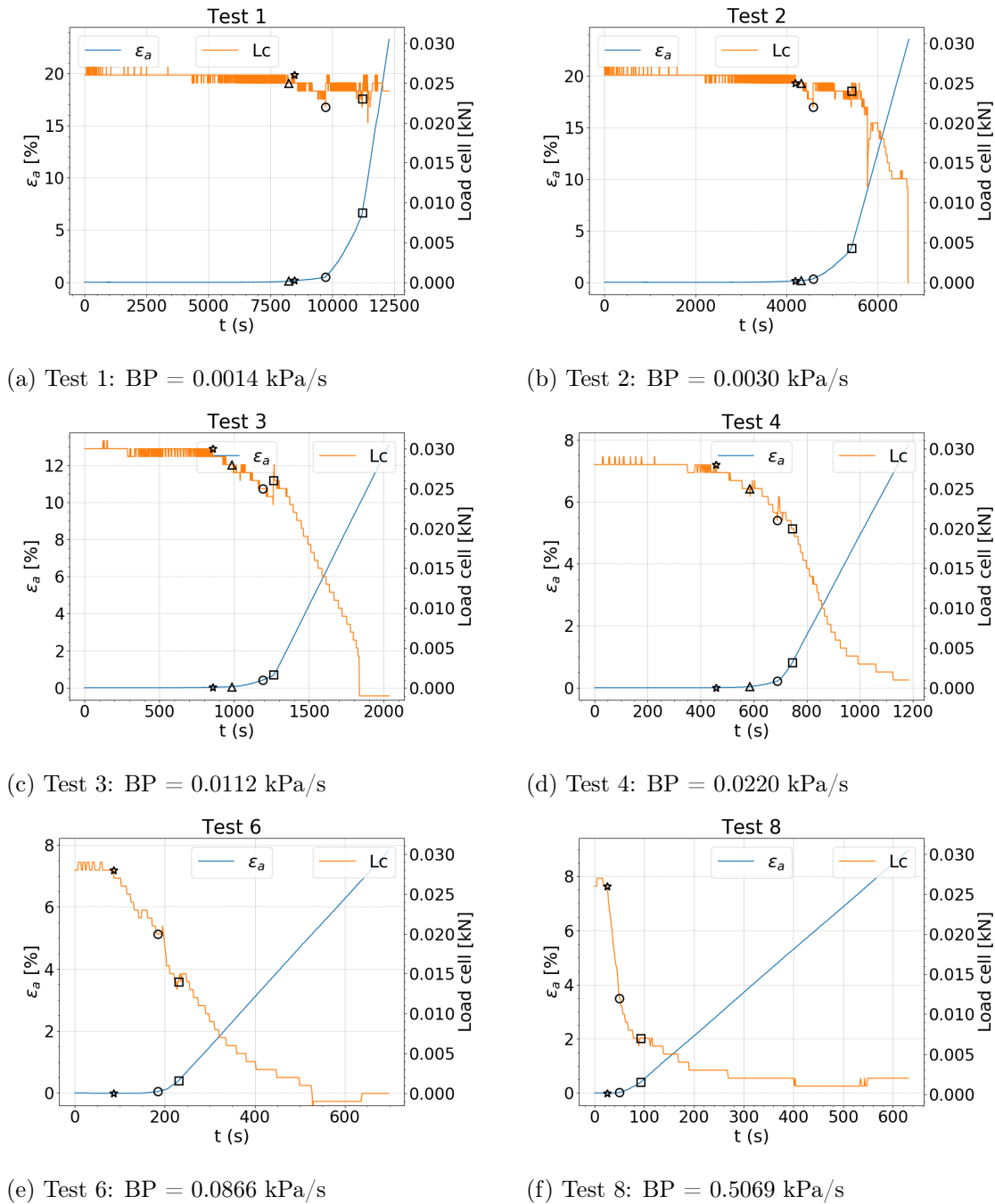


Figure 5.8: Axial strain and load cell (Lc) versus time of the advanced triaxial tests

5.2.5 Repeatability of the test results

The repeatability of the test results is described in appendix M and shows that the advanced triaxial tests are repeatable with the same soil, a relative density between 21% and 29% and the same initial stress conditions.

5.2.6 Anisotropically consolidated undrained triaxial test results

The results of the anisotropically consolidated undrained triaxial test are given in Appendix N. The relative density of the sample is 26% and it has a Skempton's parameter of 0.95. The results show a dilative soil behaviour. The stress path is overlapping the previous defined critical state line.

5.2.7 Onset of instability

Instability occurs when the soil cannot contain the current stress state (Lade & Yamamuro, 2011). Furthermore, instability precedes liquefaction slope failures (Molenkamp, 1989). To define the onset of instability and the soil behaviour, a distinction should be made between what is controlled by the setup, what is influenced by the accuracy of the sensors and what is the reaction of the soil. The accuracy of the measurements is discussed in appendix I. The performance of the setup and the reaction of the soil are depicted in figure 5.9.

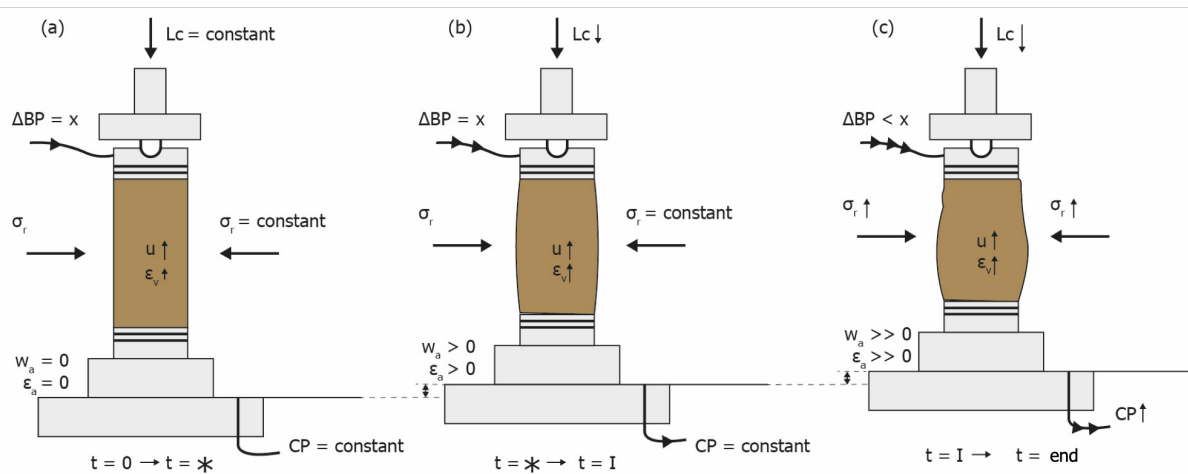


Figure 5.9: Performance of the triaxial setup depicted in three stages

During the first stage (figure 5.9 a)), the back pressure controller is injecting water with a constant velocity "x" resulting in a pore water pressure increase. The cell pressure controller is subtracting water to sustain the radial stress, which is approximately constant with a slight increase of less than 3kPa. The deviatoric stress is constant as well. The axial displacements and therefore also the axial strains are zero. The volume is increasing slightly with a constant rate because of the injection of water by the back pressure controller.

The second stage is starting when the deviatoric stress starts to drop (\star). The base of the setup is moving upwards trying to sustain the axial load, resulting in axial displacements. Axial strains are generated and the rate of volume change is increasing due to the injection of water. The cell pressure controller is subtracting more water to maintain the radial stress. The axial and volumetric strains are influenced by the load cell and back pressure controller respectively because one parameter reacts to the other.

The third stage is the stage starting at the time corresponding to the failure of the sample and the end of the test. At the end of each test, the samples are failed and wrinkles are observed in the samples, as shown in appendix O. During this stage, the back pressure is injecting more water, trying to increase the pore water pressure. The cell pressure is trying to subtract water from the cell, to go back to the initial cell pressure value. The base is moving upwards trying to go back to the initial load cell value. The volume is increasing as well as the axial strains.

Previous research shows different interpretations of defining the onset of instability. Some researchers are defining the onset of instability as the point where there is a change of volumetric dilation to contraction (Dong et al., 2016). Others are reducing the mean effective stress instead of increasing the back pressure rate and are applying a formulation of Hill's method to define the onset of instability (Zillur Rabbi, Rahman, & Cameron, 2019), while in some studies the point of rapid generation of axial strain is selected as onset point (Chu, Leong, Loke, & Wanatowski, 2012) or the point of maximum curvature in the axial strain versus time plots (Lourenço, Wang, & Chu, 2011). In this setup, the tendency of the soil to deform rapidly at instability results in a decrease in axial load, which slows down the deformation of axial strains. Therefore, the deformations are affected by the setup.

Hill's condition, based on the second-order work theory, is often used to define the instability of a material. Material is expected to be stable when the work is positive and unstable when the work is zero or negative. According to Hill's condition for triaxial tests, a dilatant behaviour of soils is always stable (Sawicki & Świdziński, 2010)-(Chu et al., 2012). Hill's condition cannot be used in this study, because there is not a change of volumetric dilation to contraction. The drop in deviatoric stress is not expected to be the point of instability, because the point of instability is often accompanied by a rapid increase in strains. While at the star the deformations start. Moreover, the maximum curvature of the axial strain versus time graphs in between the turning point of constant deviatoric stress (star) and the point of the rapid increase in axial deformation (circle) is not present as shown in figure P.1 of appendix P.

It should be taken in mind, that the above methods result in different points of onset of liquefaction as shown in previous research (Zillur Rabbi et al., 2019). More research is needed into the best method of defining the onset of liquefaction for different soils and triaxial test methods.

However, in this study, the exact point of onset of liquefaction cannot be determined. The point of onset of instability is expected to be located in between the turning point of constant deviatoric stress (star) and the point of the rapid increase in axial deformation (circle).

At the end of each test, the samples are failed and wrinkles are observed in the samples, as shown in appendix O. The point of failure cannot be determined due to the reaction of the setup.

5.3 Limitations

In previous research, similar advanced triaxial tests are often called constant shear drained tests. However, the tests in this study are neither drained nor undrained because there are volume changes and pore water pressure buildups. In some advanced triaxial tests, the cell pressure is decreased instead of the pore water pressure. This method leads to a decrease in mean effective stress as well and constant pore water pressure. Moreover, previous research showed that both methods lead to similar results (Monkul, Yamamuro, & Lade, 2011), but increasing the pore water pressure results in the development of stresses similar to the field. In liquefaction slope stability simulations, the instability is considered undrained, because of rapid displacements, while the volume is increasing in the experiments of this study. So, the drained behaviour during the test is questionable.

The triaxial test method to investigate the instability of sand under different pore water pressure increases is limited. One of the limitations is the decrease in axial load. The feedback of the load cell transducer is used to control the height of the base. A rapid increase is prevented because the required axial stress and the rate of axial strain cannot be imposed simultaneously at the top of the sample. A technique that avoids this prevention of rapid increase is by using a dead load which is connected to the top of the sample by a hanger as reported by Gajo (2000) (Gajo, Piffer,

& De Polo, 2000). The axial load will be maintained by the dead load, but an area correction during the test cannot be applied.

The area correction is applied after the test, during the data analysis. However, the change in the area during the test is assumed to be of no hindrance for the development of rapid failure, because the instability occurred at relatively low axial strains. Another correction that could be applied is membrane penetration, which was considered not to be significant for fine sand with a diameter of 0.11 mm (Monkul et al., 2011).

Another questionable point is the sample preparation method and the homogeneity of the sample. The samples are prepared by wet pluviation. This technique was demonstrated to initiate the soil response and fabric of undisturbed samples (Vaid & Sivathayalan, 2000). Moreover, the laboratory sand was also used in the liquefaction tank tests. De Jager (2018) stated that a slope in the liquefaction tank fails when the porosity is larger than 0.468 (De Jager, 2018), which is the case for the samples in this study. However, the homogeneity of the sample structure is not investigated. This can be done with computerized tomography techniques which would be an advice to investigate further. The homogeneity of the pore water pressure distribution seems to be fine because the back pressure measurements at the top are similar to the pore water pressure at the bottom. However, boundary effects, bulging of samples and other deformations could lead to non-uniform stress distributions.

Generalization of the test results should be done with care because the findings of the experimental study are limited to preloaded Geba sand samples. To generalize the test results, this study can be compared with previous studies that have an identical method or additional tests can be done with different types of sand and initial stress conditions.

5.4 Conclusions on experiments

The experimental study answers the sub-question: "What is the soil response to the hydraulic triggering in triaxial experiments?". The hydraulic triggering in the triaxial experiments is simulated by an increase in back pressure leading to an increase in pore water pressure. At the start of the test, the mean effective stress is decreasing while the deviatoric stress is constant. After a certain time, the deviatoric stress starts to drop and axial deformations are developed. This time is dependent on the rate of back pressure increase. The drop starts at lower deviatoric stresses for higher back pressure rates. Figure 5.3 predicts an asymptotic behaviour of the stress ratio at which the deviatoric stress drops for increasing pore water pressure rate. The drop in deviatoric stress is located at the start of axial deformations. The onset of instability is linked to the deformations. Therefore it is expected instability occurs also at lower mean effective stresses for higher pore water pressure rates.

The axial load is decreasing that leads to the prevention of rapid deformations. So, the load cell is slowing down the deformation. Therefore, the exact point of onset of instability cannot be determined. It is expected that the onset of instability is located in between the drop of deviatoric stress and the first point of formation of rapid strains.

6 | Implications for the field

The implications are listed in this chapter. They describe the relevance of the findings to the case study and the differences between the case study and the experiments that should be kept in mind.

Critical region

Finite element simulations in Plaxis 2D are used for the determination of the critical region inside a submarine slope. A region close to the bed, in between the toe and the centre of the slope, is selected to be the critical region (figure 6.1). This region is increasing in depth for steeper slopes from a 1:5 ratio to a 1:2 ratio. Based on these findings, the soil close to the bed, in between the toe and the centre, is expected to be critical in the field as well. The soil in this region is more prone to become unstable. Therefore, it is likely that the liquefaction slope failures are initiated here. Moreover, a local instability could initiate its surroundings to get unstable as well. At this moment Rijkswaterstaat is inspecting the whole slope, while this research suggests focussing on the part close to the sloping bed between the toe and the centre. Alternative maintenance methods could be based on this finding. For instance, installing hydraulic structures that aim to decrease the flow velocities magnitude or frequency above the critical zone. Another example is placing vertical drains to decrease the buildup of excess pore water pressures.

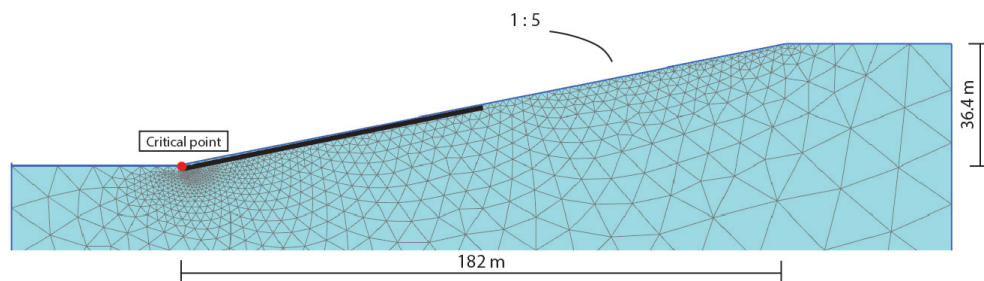


Figure 6.1: The critical region of a submarine slope with ratio 1:5 indicated by a black area and a critical point in red

Rate of pore water pressure fluctuation

The maximum rate of pore water pressure fluctuation is determined by Plaxis2D for multiple combinations of frequency and amplitude of the water pressure at the bed. This rate of buildup of pore water pressure might occur in the field for the selected combinations. The results show that higher amplitudes and higher frequencies result in a faster increase in pore water pressure. An investigation into the statics of the probability of the selected combinations of amplitude and frequency to occur in the field is recommended. Moreover, field measurements of the water pressure at the sloping bed between the toe and the centre of the slope would give more reliable results. This could be the next step of investigating the triggering mechanism of the liquefaction flow slides close to the barrier.

There are a few differences between the model of Plaxis2D and the field for obtaining the maximum rate of pore water pressure buildup. First of all, the homogeneity of the soil plays a role. The soil in Plaxis2D is modelled as one layer, while the in situ soil consists of multiple layers and the soil properties are heterogeneous and spatially variable. This inhomogeneity could lead to weaker and stronger zones within the soil. Characteristics of these weaker zones are a low relative density, relatively low strength and relatively high pore water pressures. A liquefaction slope failure is expected to be initiated in a weaker zone. To locate these zones, cone penetration tests can be done at the scour holes.

Second, the soil in the field consists of sand with alternating clay layers. The flow of pore water pressure is following the path of the least resistance. Therefore, the water will be expelled through the sand layers and clay layers will lengthen the drainage path that could lead to an increase in pore water pressure buildup. At this moment, the clay layers are slowing down the scour hole formation. However, it could be possible that the presence of the clay layers results in an even larger excess pore water pressure buildup which contributes to the probability of slope failure.

Furthermore, the water flow is simplified as a time-dependent harmonic fluctuation that is constant in space. Whereas the velocity measurements near the barrier show a more complex velocity profile (Broekema et al., 2018), which leads to inhomogeneity of the water pressures at the bed as well.

Instability and failure

Instability precedes liquefaction slope failures (Molenkamp, 1989). The triaxial tests showed that higher rates of pore water pressure increase lead to instabilities at lower effective stresses. Because instabilities precede liquefaction slope failures (Molenkamp, 1989), it is expected that soil with a more rapid increase of pore water pressure increase is more sensitive to liquefy. The triaxial samples all liquefied at the end of the test. The failure cannot be compared with the field, due to the effects of boundaries in the triaxial setup and due to the controllers that are trying to keep the pressures constant, but the drop in deviatoric stress can be compared.

Drop in deviatoric stress

The results of the advanced triaxial tests show a decrease in stress ratio at which the deviatoric stress starts to drop for an increase in the rate of the pore water pressure buildup (figure 5.3). The drop of deviatoric stress is representing the start of axial deformations. It is expected that the stress ratio of this drop versus pore water pressure rate is descending to an asymptote. The graph of figure 5.3, can predict when the start of the drop in deviatoric stress could occur with this setup, so the results can be extrapolated to more field conditions.

However, the triaxial setup cannot fully mimic what is happening in the field. Therefore the differences in the triaxial setup and the field are discussed and the effects on the findings of this research are presented.

The triaxial test represents one point inside a slope (figure 6.1). Whereas this slope represents a scour hole slope close to the Eastern Scheldt barrier. The triaxial tests can predict the soil behaviour of points at approximately 1 meter distance from the bed. The test results can be extrapolated to other points within the critical region that have similar stress states and mean effective stresses. The findings of the soil behaviour of this point can be expanded to a zone with similar relative shear stresses. This zone is indicated by a black line and it is discussed in

4.1.4 as well. The triaxial tests show that higher rates of pore water pressure increase result in deformations and instability at higher mean effective stresses. So, this is also expected for other points within the zone presented in figure 4.1.4.

A difference between the triaxial test stresses and the stresses in the field is the orientation of the principal stresses. Figure 6.2 and figure 6.3 of model 1 show the direction of principal stresses. At certain points inside the slope, the principal stress directions are the same as a triaxial compression test. Other points can be represented by extension tests or simple shear tests. However, in the triaxial tests of this study, the principal stress direction is 0° while the selected point inside the slope encounters a rotation of principal stresses during erosion. The principal stress direction at the start of increasing the pore water pressure should be 74.5° according to the Plaxis model 1. The critical state line of extension tests and compression tests differ. Therefore, it is expected that the instability line differs as well for different orientations of principal stresses. The influence of the direction of principal stresses could be investigated by a hollow cylinder triaxial test.

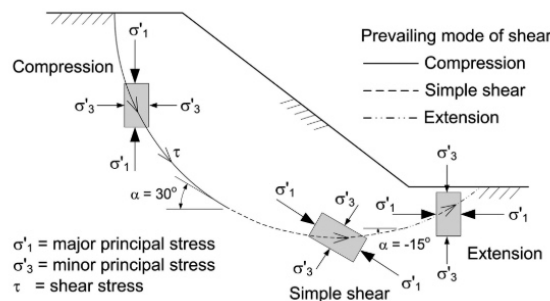


Figure 6.2: Rotation of principal stresses in triaxial tests (Sadrekarimi, 2014)

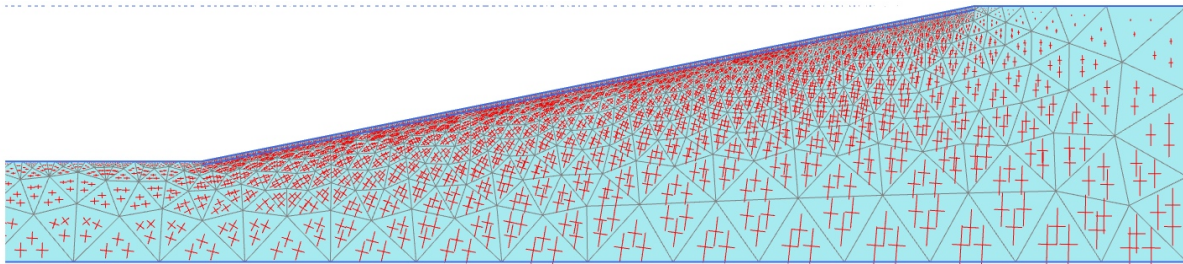


Figure 6.3: Rotation of principal stresses observed in Plaxis 2D model 1

A limitation of this research is that one effect of the currents on the soil is investigated, which is the fluctuation of water pressure. This fluctuation is simulated in the triaxial tests by a linear increase. Other effects of the currents on the soil are the generation of shear stresses within the soil and the fluctuation of total stresses. These effects are not simulated in the triaxial tests. The shear stresses in the soil are expected to increase the deviatoric stresses resulting in a stress state that is positioned closer to the critical state line and an earlier instability. To investigate the influence of the generation of shear stresses inside the soil and the fluctuation of the total stresses, the relation to the currents need to be investigated. This can be done by fieldwork tests and cyclic triaxial tests. All in all, one effect of the influence of the currents on the soil response is investigated, in other words, this research is one step in the direction of a better understanding of the initiation of liquefaction slope failures near the Easter Scheldt barrier.

7 | Conclusions and recommendations

Five sub-questions, provided in the introduction chapter of this report are answered. This chapter summarizes the conclusions of the sub-questions, followed by an answer to the main research question and the recommendations.

7.1 Conclusions

Sub-questions

What are the soil properties of a submarine slope near the Eastern Scheldt barrier and what is the slope geometry before failure?

The soil near the barrier consists mainly out of sand with grain sizes ranging from fine to medium coarse. The available density measurements show that there are locations where the porosity of the sand is relatively high in comparison with other locations. This confirms the presence of loose sand which is prone to liquefaction. Besides the relatively low-density locations, recently sedimented soils are generally loose as well. The sand layers are alternated by clay layers that are slowing down the development of a scour hole with depth resulting in an expansion of the scour hole in lateral direction. It follows that the geometry of the scour hole slopes is complex and that a critical combination of slope ratio and slope height is unlikely. This is supported by an investigation into the bathymetry data of past slope failures. It shows an average slope ratio of less than 1:5 for slopes before failure of which a part over at least 5 meters has relatively steep slope ratios (1:3 and 1:2). Moreover, the bathymetry data deduced that some slopes with a relatively steep angle did not fail (yet). However, the exact submarine slope geometry at the initiation of failure cannot be determined with the available bathymetry data which is gathered two times a year.

Which part of the slopes is more prone to become unstable (critical regions)?

The region below a sloping bed with a slope ratio of 1:5 (vertical:horizontal) close to the surface, where the mean effective stress is relatively low, is considered critical because the relative shear stress is relatively high in this area. The part from toe to centre of the sloping bed of this critical region is expected to be more prone to instability due to the presence of a larger area of high relative shear stresses. Similar results were observed for slopes with a 1:3 and 1:2 slope ratio. However, the region which is more prone to instability was located more towards the centre of the slope instead of the toe.

What is the range of water pressure accumulation at the bed due to the water flow?

Previous research into the current velocity profile of the Eastern Scheldt barrier area showed a slight increase in velocity with scour hole depth. Therefore, the velocity measurements (ADCP) at the deepest measurement location were analysed to define the water pressure accumulation at the bed. A formulation of the White-Colebrook type of formula and an empirical correlation of bed shear stress and water pressure is applied to define a first approximation of the order of magnitude of water pressures at the bed. However, an averaged flow velocity is applied to define the water pressure while the extreme values are expected to be significant for initiating instabilities. Because of that and due to the complexity of the velocity profiles the range of water pressure was increased in this research. The water pressure was assumed to be constant in space,

although this is not the case in the field. However, for a first indication of the water pressures at the bed, this approximation is sufficient.

What are the stress conditions of a point inside the critical region?

The Cambridge stress parameters of points inside the critical region from toe to centre of the slope at 1 meter below the bed were considered to be relatively similar. A point close to the toe of the 1:5 slope was selected to investigate further. The stress history of this point can be divided into a sedimentation stage and an unloading stage. During sedimentation, the mean effective stress and deviatoric stress are following the lateral earth pressure line. When scour formation starts, the stresses of the selected point will decrease to a position just below the lateral earth pressure line in a Cambridge stress path plot.

The pore water pressure increase at this point was determined by a 1-dimensional Plaxis finite element model and resulted in an increase of excess pore water pressure for all preselected water pressure ranges. The maximum rate of this excess pore water pressure increase appears at the highest pore water magnitude and highest frequency.

What is the soil response to the hydraulic triggering in triaxial experiments?

The hydraulic triggering can be simulated by increasing the back pressure, leading to a pore water pressure increase and a decrease in mean effective stress. The axial load starts to drop when the sample starts to deform axially. This drop appears earlier in time and at lower stress ratio's ($\eta = q/p'$) for increasing back pressure rates. Moreover, this drop influences the rate of axial deformation, which interferes the determination of the onset of instability. The volumetric strains are increasing resulting in an increasing void ratio. The triaxial tests are reproducible but generalization of the test results should be done with care because the findings are limited to Geba sand samples with a specific stress history and relatively low effective stresses during the back pressure change phase.

Main research question

What is the effect of water pressure fluctuations caused by the flow (hydraulic triggering) on the soil response of loose sand in submarine slopes close to the Eastern Scheldt storm surge barrier?

The water pressure at the bed generates excess pore water pressures inside a submarine slope close to the barrier. The rate of increase of the excess pore water pressure affects the stability of a soil element because triaxial tests showed that higher pore water pressure rates result in earlier developments of deformation at lower stress ratios. It is expected that the water flow leads to liquefaction. One of the reasons for this expectation is that excess pore water pressures are generated and liquefaction slope failures occur due to pore water pressure buildup. Another reason is that higher flow velocities in combination with higher frequencies lead to instabilities at lower stress ratios and liquefaction failures are preceded by instabilities. Furthermore, the liquefaction flow slides are probably initiated in the critical zone which is located close to the sloping bed in between the toe and the centre of the slope.

7.2 Recommendations

The recommendations for further research are listed in this section. First of all, a field measurement campaign is suggested to gain more insight into the water pressures at the bed. At this moment, Rijkswaterstaat is planning to take field measurements of the water pressures at the bed near the Eastern Scheldt barrier. Taking simultaneous velocity and water level measurements would be interesting to be able to link the water pressures to the velocity data. To give a better

approximation on the range of frequencies of the water pressure change, measurements with a logging time of seconds is recommended. Furthermore, it is suggested to take the measurements at the bed close to the zone in between the toe and centre of the slope. Besides water pressures at the bed, pore water pressures inside the slope are also recommended, which can be done by piezometers. These measurements could give more insight into the water flow inside the soil.

To improve the test results, some adjustments to the triaxial test setup are advised. One of the adjustments is changing the axial load into a dead load to be able to sustain constant axial stress. This dead load can be connected to the sample by a hanger which was done by Gajo (2000) (Gajo et al., 2000). Another adjustment would be the application of a high-speed acquisition system. When a dead load is applied, the propagation of axial strain will increase. Instability could occur within seconds, therefore a system that can measure every 0.1 seconds would be advised. Furthermore, a more accurate measurement of the axial strains can be done by adding an internal LVDT triaxial cell. The last adjustment is more related to the experimental program and to the behaviour of the soil after the onset of instability. As discussed before, instability is, most of the time, related to undrained behaviour. However, the triaxial tests in this study are continuously drained. So, a system with a build-in detection of the onset of instability, which could be rapid deformation, should be applied which could switch the conditions to undrained at the same time as the onset of instability is detected.

Furthermore, the triaxial test experiments could be continued. Interesting tests would be investigating the effects of the initial state on the soil behaviour to constant deviatoric stress triaxial tests with increasing back pressure. Furthermore, the influence of the direction of principal stresses on the test results can be investigated with hollow cylinder triaxial tests. Moreover, test with different types of soil and different relative densities are advised.

In addition to these tests, an investigation into the methods of defining the onset of instability is also needed. At this moment, different methods for defining the onset of instability are applied in previous research, which led to different results. A possibility of defining the onset of liquefaction of a triaxial sample is by investigating the energy transfer from potential to kinetic energy during instability.

Another recommendation is linking the triaxial test results to a numerical simulation of liquefaction slope instability or by linking the tests to larger-scale tests as liquefaction tank tests. By combining these tests, a better prediction can be done to the soil behaviour in the field.

References

- Atkinson, J. (1993). *An introduction to the mechanics of soils and foundations*. Berkshire: McGraw-Hill Book Company Europe.
- Been, K., Jefferies, M. G., & Hachey, J. (1991). The critical state of sands. *Géotechnique*, 41(3), 365–381. doi: 10.1680/geot.1992.42.4.655
- Brinkgreve, R. (2018a, December). *Lecture notes behaviour of soils and rocks 16 - hardening soil*. University of technology Delft.
- Brinkgreve, R. (2018b, December). *Lecture notes behaviour of soils and rocks 21 - parameter determination*. University of technology Delft.
- Broekema, Y., Labeur, R., & Uijttewaal, W. (2018). Observations and analysis of the horizontal structure of a tidal jet at deep scour holes. *Journal of Geophysical Research: Earth Surface*. doi: 10.1029/2018JF004754
- Chu, J., Leong, W. K., Loke, W. L., & Wanatowski, D. (2012). Instability of loose sand under drained conditions. *Journal of Geotechnical and Geoenvironmental Engineering*, 138(2), 207–216. doi: 10.1061/(ASCE)GT.1943-5606.0000574
- De Kleine, M., Vanhögen-Peeters, L., & Marges, V. (2012). *Deelrapportage Databeheer en Monitoring*. doi: 1206907-004-GEO-0003
- De Jager, R. (2018). *Assessing liquefaction flow slides: Beyond empiricism* (Unpublished doctoral dissertation). Delft University of Technology.
- Desrues, J. (2004). Tracking strain localization in geomaterials using computerized tomography. *X-ray CT for Geomaterials*, 15–41.
- Detert, M., Jirka, G., Jehle, M., Klar, M., Jähne, B., Köhler, H., & Wenka, T. (2004). Pressure fluctuations within subsurface gravel bed caused by turbulent open-channel flow. *Proceedings of river flow*, 1, 695–701.
- Dinoloket. (2014). *Ondergrondgegevens*. Retrieved from <https://www.dinoloket.nl/ondergrondgegevens>
- Dong, Q., Xu, C., Cai, Y., Juang, H., Wang, J., Yang, Z., & Gu, C. (2016). Drained instability in loose granular material. *International Journal of Geomechanics*, 16(2). doi: 10.1061/(ASCE)GM.1943-5622.0000524
- Gajo, A., Piffer, L., & De Polo, F. (2000). Analysis of certain factors affecting the unstable behaviour of saturated loose sand. *Mechanics of Cohesive-frictional Materials*, 5, 215–237. doi: 10.1002/(sici)1099-1484(200004)5:3<215::aid-cfm92>3.3.co;2-z
- Google Earth Pro 7.3.2. (2019, March). *Oosterscheldekering in zeeland 51°37'45.82''n, 3°43'5.44''o*. Retrieved from <https://www.google.com/maps/@51.62049,3.74925,19839m/data=!3m1!1e3> (Accessed on 09-12-2019)
- Head, K., & Epps, R. (2014). *Manual of soil laboratory testing, volume 3 - effective stress tests* (Vol. 3) (No. 3). Whittles Publishing.
- Janssen, H., van Kuijk, E., Saathof, K., Liek, G., Vereeke, S., Saman, K., ... Steenepoorte, K. (2017). *Voortgangsrapportage BBT 2016* (Tech. Rep.). Rijkswaterstaat.
- Janssen, H., van Kuijk, E., Saathof, K., Liek, G.-J., Vereeke, S., Saman, K., ... Steenepoorte, K. (2018). *Voortgangsrapportage BBT 2017* (Tech. Rep.). Rijkswaterstaat.
- Jefferies, M., & Been, K. (2016). *Soil liquefaction: a critical state approach*. CRC press.
- Koppejan, A., Van Wamelen, B., & Weinberg, L. (1948). Coastal flow slides in the Dutch province of Zeeland. Delft.
- Krapfenbauer, C. (2016). *Experimental Investigation of Static Liquefaction in Submarine Slopes* (Unpublished doctoral dissertation). ETH Zurich.
- Lade, P. V., & Yamamuro, J. A. (2011). Evaluation of static liquefaction potential of

- silty sand slopes. *Canadian Geotechnical Journal*, 48(2), 247–264. Retrieved from <http://www.nrcresearchpress.com/doi/abs/10.1139/T10-063> doi: 10.1139/T10-063
- Lourenço, S., Wang, G., & Chu, J. (2011). Aspects of sand behaviour by modified constant shear drained tests. *Environmental Earth Sciences*, 62(4), 865–870. doi: 10.1007/s12665-010-0573-8
- Maghsoudloo, A., Galavi, V., Hicks, M., & Askarinejad, A. (2017). Finite element simulation of static liquefaction of submerged sand slopes using a multilaminar model. *Proceedings of the 19th International Conference on Soil Mechanics and Geotechnical Engineering*, 801–804.
- Mathijssen, F. A. J. M., de Jager, R. R., & Hooiveld, B. J. (2015). Reliability Based Design of Dredge Sludge Depot for Mechanism Static Liquefaction. In *Geotechnical safety and risk v* (pp. 320–327). doi: 10.3233/978-1-61499-580-7-320
- Molenkamp, F. (1989). Liquefaction as an instability. *Conference Soil Mechanics Foundation engineering*, 157–163.
- Monkul, M., Yamamuro, J., & Lade, P. (2011). Failure, instability, and the second work increment in loose silty sand. *Canadian Geotechnical Journal*, 48, 943–955. doi: 10.1139/t11-013
- Muraro, S. (2019). *The deviatoric behaviour of peat: a route between past empiricism and future perspectives* (Doctoral dissertation). doi: <https://doi.org/10.4233/uuid:ffbea4e0-2e97-4d41-819d-beec42120b29>
- Nederland fietsland. (n.d.). *Afbeelding fietskaart nederland*. Retrieved from <https://www.nederlandfietsland.nl/lf-routes/ronde-van-nederland> (Accessed on 09-12-2019)
- Noriega, S. (2015). *Characterisation of Saturated Loose Sand Samples prepared by Fluidization* (Tech. Rep.). Delft: Delft University of Technology. Retrieved from <http://repository.tudelft.nl/>
- Olson, S. M. (2001). *Liquefaction Analysis of Level and Sloping Ground Using Field Case Histories and Penetration Resistance, PhD Thesis* (Doctoral dissertation, University of Illinois at Urbana-Champaign). doi: 10.16953/deusbed.74839
- Owen, G., & Moretti, M. (2011). Identifying triggers for liquefaction-induced soft-sediment deformation in sands. *Sedimentary Geology*, 235(3-4), 141–147. doi: 10.1016/j.sedgeo.2010.10.003
- Plaxis. (2019a). *Plaxis 2D Reference Manual 2019* (Tech. Rep.). Author.
- Plaxis. (2019b). *Plaxis material models manual 2019* (Tech. Rep.). Author.
- Projectteam OSK Rijkswaterstaat. (2014). *Herbeschouwing bodembescherming en herijking faalkans Oosterscheldekering* (Tech. Rep.). Rijkswaterstaat.
- Raaijmakers, T., van Velzen, G., Hoffmans, G., Bijlsma, A., Verbruggen, W., & Start, J. (2012). *Stormvloedkering Oosterschelde: Ontwikkeling ontgrondingskuilen en stabiliteit bodembescherming - Deelrapportage Ontgrondingen* (Tech. Rep.). Deltares.
- Rees, S. (2013). *Part one: Introduction to triaxial testing prepared* (Tech. Rep. No. 1). Retrieved from www.gdsinstruments.com
- Rijkswaterstaat. (n.d.). *Ontwerpnota stormvloedkering Oosterschelde, boek 2: de waterbouwkundige werken*.
- Rijkswaterstaat. (2013). *Beheer Oosterscheldekering nader bekeken* (Tech. Rep.). Author.
- Sadrekarami, A. (2014). Effect of the mode of shear on static liquefaction analysis. *Journal of Geotechnical and Geoenvironmental Engineering*, 140(12), 04014069.
- Sawicki, A., & Świdziński, W. (2010). Modelling the pre-failure instabilities of sand. *Computers and Geotechnics*, 37, 781–788. doi: 10.1016/j.compgeo.2010.06.004
- Schanz, T., & Vermeer, P. (1998). On the stiffness of sands. *Géotechnique*, 48, 383–387.
- Silvis, F. (1985). *Statistische analyse zettingsvloeiingen* (Tech. Rep.). Delft: Delft Soil mechanics laboratory.

- Steenepoorte, K., Weijers, J., Janssen, H., de Wilde, D., Schog, K., Lievense, P., . . . Saman, K. (2012). *Voortgangsrapportage BBT 2012* (Tech. Rep. No. december). Rijkswaterstaat.
- Stoutjesdijk, T., Mastbergen, D., & De Groot, M. (2012). *Stormvloedkering Oosterschelde: Ontwikkeling ontgrondingskuilen en stabiliteit bodembescherming - Deelrapportage Hellingsinstabiliteit* (Tech. Rep.). Deltares. doi: 1206907-004-GEO-0003
- Stoutjesdijk, T. P., de Groot, M. B., & Lindenberg, J. (1998). Flow slide prediction method: influence of slope geometry. *Canadian Geotechnical Journal*, 35, 43–54. doi: 10.1139/t97-068
- Uijtewaal, W., & Labeur, R. (2019, October). *Lecture notes fluid mechanics - weerstand in open waterlopen*. University of technology Delft.
- Vaid, Y., & Sivathayalan, S. (2000). Fundamental factors affecting liquefaction susceptibility of sands. *Canadian Geotechnical Journal*, 37, 592–606. doi: 10.1139/t00-040
- Van den Ham, G. A., & Stoutjesdijk, T. P. (2014). *Overzicht state of the art kennis zettingsvloeiingen en bestorting* (Tech. Rep.). Deltares.
- van Velzen, G., Raaijmakers, T., & Hoffmans, G. (2015). Scour development around the Eastern Scheldt storm surge barrier-field measurements and model predictions. In L. Cheng, S. Draper, & H. An (Eds.), *Scour and erosion: Proceedings of the 7th international conference on scour and erosion, perth, australia* (pp. 693–704). London: CRC Press Taylor & Francis Group. Retrieved from <http://ascelibrary.org/doi/book/10.1061/9780784411476> doi: 10.1016/j.ijheatmasstransfer.2014.11.077
- Visser, T. (1986). *Ontwerpnota stormvloedkering Oosterschelde: Totaalontwerp en ontwerpfilosofie - Deel 2*. Rijkswaterstaat.
- Vollmer, S., & Kleinhans, M. G. (2007). Predicting incipient motion, including the effect of turbulent pressure fluctuations in the bed. *Water Resources Research*, 43(5), 1–16. doi: 10.1029/2006WR004919
- Wilderom, M. (1979). *Resultaten van het vooroeveronderzoek langs de Zeeuwse stromen* (Tech. Rep.). Vlissingen: Rijkswaterstaat.
- Yoshimine, M., Robertson, P., & Fear Wride, C. (1999). Undrained shear strength of clean sands to trigger flow liquefaction. *Canadian Geotechnical Journal*, 36, 891–906. doi: 10.1139/t99-047
- Zillur Rabbi, A., Rahman, M., & Cameron, D. (2019). Critical state study of natural silty sand instability under undrained and constant shear drained path. *International Journal of Geomechanics*, 19(8), 1–13. doi: 10.1061/(ASCE)GM.1943-5622.0001462

A | Background

A.1 Triaxial compression test

The failure of a soil sample under shear can be investigated with a triaxial compression or extension test. Triaxial tests subject cylindrical soil samples to radial stresses and a change in axial stresses or axial displacements. The tests can be load-controlled or strain-controlled.

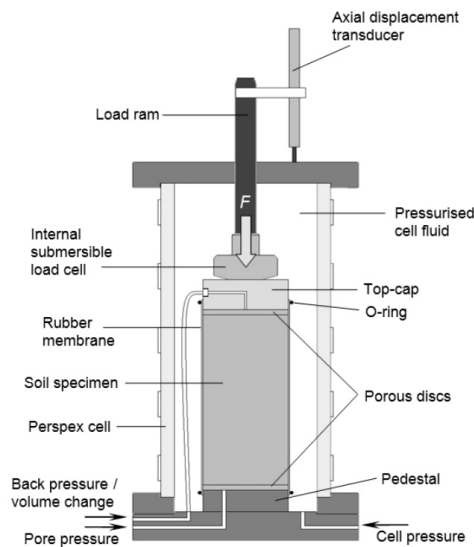


Figure A.1: A general triaxial set-up (Rees, 2013)

The triaxial setup is shown in figure A.1. An undisturbed or remolded soil sample is located inside a cylindrical transparent cell filled with water. The sample is enclosed in a rubber membrane which is connected to the top-cap and base by o-rings. The three principal stresses (σ_1 , σ_2 and σ_3) are applied and controlled during a triaxial test. In triaxial compression tests the horizontal principal stresses (σ_2 and σ_3) are equal to the radial stress (σ_r): $\sigma_r = \sigma_2 = \sigma_3$. The radial stress is controlled by the cell pressure controller. This stress is applied by pressurizing the cell fluid and is normally kept constant during loading. The pore water pressure within the sample is controlled by the back pressure controller. The pore pressure (u) measured at the bottom of the sample is equivalent to the back pressure, which is controlled at the top. An axial load (F_a [N]) is applied at the top cap. Dividing this load by the area of the sample results in the axial stress which is the major principal stress (σ_1). During a test, the load, cell pressure and back pressure are controlled and the time, radial stress, cell volume, back pressure, back volume, load cell, axial displacement and pore water pressure are measured.

A.2 Mechanical behaviour of saturated sands

The mechanical behaviour of saturated sands depends on the volumetric and deviatoric stress-strain properties of the soil. These properties can be investigated with triaxial tests. The triaxial

samples will fail when the soils are loaded just beyond the maximum shear stress that the soil can sustain (Atkinson, 1993). The results of the triaxial tests of saturated sand under undrained and drained conditions are shown in figure A.2 (a)-(c) and figure A.2 (d)-(f) respectively. The soil behaviour is strongly dependent on the density of the soil. The tendency of soil to dilate or contract depends on among others the density and whether the sand is loaded in drained or undrained conditions. In this section, first, the stress path is described followed by the critical state and steady state. Afterwards, a distinction is made between undrained behaviour of sands and drained behaviour of sands for different initial densities varying from a very loose state to a dense state. The sand samples are normally consolidated to equal effective stress. The instability line is discussed at the end of this section.

Stress path

The stress state between the initial and final stage can be graphically presented in a stress path plot (e.g. Cambridge stress path plot). The three principal effective stresses (σ_1, σ_2 and σ_3) are used in a Cambridge stress path plot with on the y-axis the deviatoric stress (q) and on the x-axis the mean total stress (p) for a total stress path plot or mean effective stress (p') for an effective stress path plot. The slope of the stress path of the drained compression triaxial tests has a ratio of 3 on 1. The mean total stress (p) is:

$$p = \frac{\sigma_1 + \sigma_2 + \sigma_3}{3} \quad (\text{A.1})$$

and the mean effective stress (p') is:

$$p' = \frac{\sigma'_1 + \sigma'_2 + \sigma'_3}{3} \quad (\text{A.2})$$

In triaxial compression tests the horizontal principal stresses (σ_2 and σ_3) are equal to the radial stress: $\sigma_r = \sigma_2 = \sigma_3$ and the major principal stress is equal to the axial stress (σ_a), which gives:

$$p = \frac{\sigma_1 + 2\sigma_3}{3} = \frac{\sigma_a + 2\sigma_r}{3} \quad (\text{A.3})$$

and in terms of effective stress is:

$$p' = \frac{\sigma'_1 + 2\sigma'_3}{3} = \frac{\sigma'_a + 2\sigma'_r}{3} \quad (\text{A.4})$$

The deviatoric stress is defined by:

$$q = \sigma'_1 - \sigma'_3 = \sigma_1 - \sigma_3 = \sigma_a - \sigma_r \quad (\text{A.5})$$

Critical state and steady state

The critical state is the state at which soil continues to deform at constant stress, constant void ratio and constant velocity (Jefferies & Been, 2016). According to Jefferies (2016), 20% axial strain is required to reach the critical conditions. Atkinson (1993) stated that if there are volume, pore pressure or stress changes, the critical state is not yet reached (Atkinson, 1993). The critical state is unique for every soil and therefore independent of factors such as stress path, fabric, sample preparation and initial density (Been, Jefferies, & Hachey, 1991). On the other hand, before the critical state is reached, the behaviour of the soil is dependent on these factors.

The steady state is the state at which the minimum shear stress is reached at relatively large strains. In general, the steady state is defined by using undrained tests on loose samples while the critical state is defined by drained tests on dense samples (Been et al., 1991). For sands, the steady state is equivalent to the critical state (Atkinson, 1993).

The steady state should not be confused with the quasi-steady state, which is a temporary condition that is dependent on for instance fabric and test conditions (Jefferies & Been, 2016). This quasi-steady state is reached when a phase transformation proceeds under undrained conditions at a minimum mean effective stress. The critical state is reached at the final stage.

The locus of the critical state points in a stress path plot is the critical state line. The relation of the critical state line and the critical friction angle (ϕ') in the Cambridge stress field is given by (Jefferies & Been, 2016):

$$M = \frac{6 \sin \phi'}{3 - \sin \phi'} \quad (\text{A.6})$$

With M as the angle of the critical state line:

$$\tan M = \frac{q}{p'} \quad (\text{A.7})$$

Undrained behaviour

Figure A.2 (a) gives a Cambridge stress path plot of undrained triaxial tests with the critical state line (CSL). If the soil tends to dilate or contract is shown in the pore pressure versus axial strain graphs, figure A.2 (c). During these tests the void ratio is constant, because there is no volume change.

The typical behaviour of very loose sand is given by the lines with label 'L'. During compression, a loose sand sample tends to contract, pore pressure increases with axial strain. A loose sample develops its peak strength, maximum deviatoric stress, at a relatively low axial strain. After reaching the peak strength the sample is softening. In other words, the sample loses strength with increasing axial strain. The strength at the end of the test is the steady state strength. A loose sand sample is moving towards the critical state line with the reduction of the mean effective stress and shear stress (figure A.2 (a)). The effective stress path reaches the critical state line at zero effective stress. This failure behaviour is called liquefaction failure.

Limited liquefaction failure is shown by a medium dense sample (label 'M'). After reaching a peak, the effective stress path is not descending to liquefaction but the sample is recovering. When it reaches the phase transformation point, the sample is strain hardening and the deviatoric stress and mean effective stress start to increase with an increase in axial strain.

Dense soils tend to contract at the initial stage, figure A.2 (c). Because at relatively low axial strain the pore water pressure is increasing until this pressure reaches a peak. Afterwards, the pore pressure is decreasing and eventually passing the x-axis. During this decrease, the soil has a tendency to dilate. When the effective stress path intersects the total stress path, the pore water pressure is turning negative.

Drained behaviour

The drained triaxial test results of saturated sand are given in figure A.2 (d), (e) and (f). The total and effective stress paths show straight lines and are overlapping for loose, medium and dense samples. Soils in a dense state initially reach a peak state before reaching the critical state (Atkinson, 1993), figure A.2 (e). After reaching the peak state, the dense sample is strain softening. Figure A.2 (f) gives the volumetric strain versus axial strain results. Compression has negative volumetric strain and expansion has positive volumetric strain. Dense samples contract at low axial strain and dilate after reaching the maximum deviatoric stress.

Medium dense samples have a relatively small peak in deviatoric stress and less dilative behaviour than dense samples. The strength is increasing continuously with increasing axial strain for loose samples. These samples have their maximum strength at the critical state. The volumetric strain versus axial strain graph shows a contractive behaviour (figure A.2 (f)).

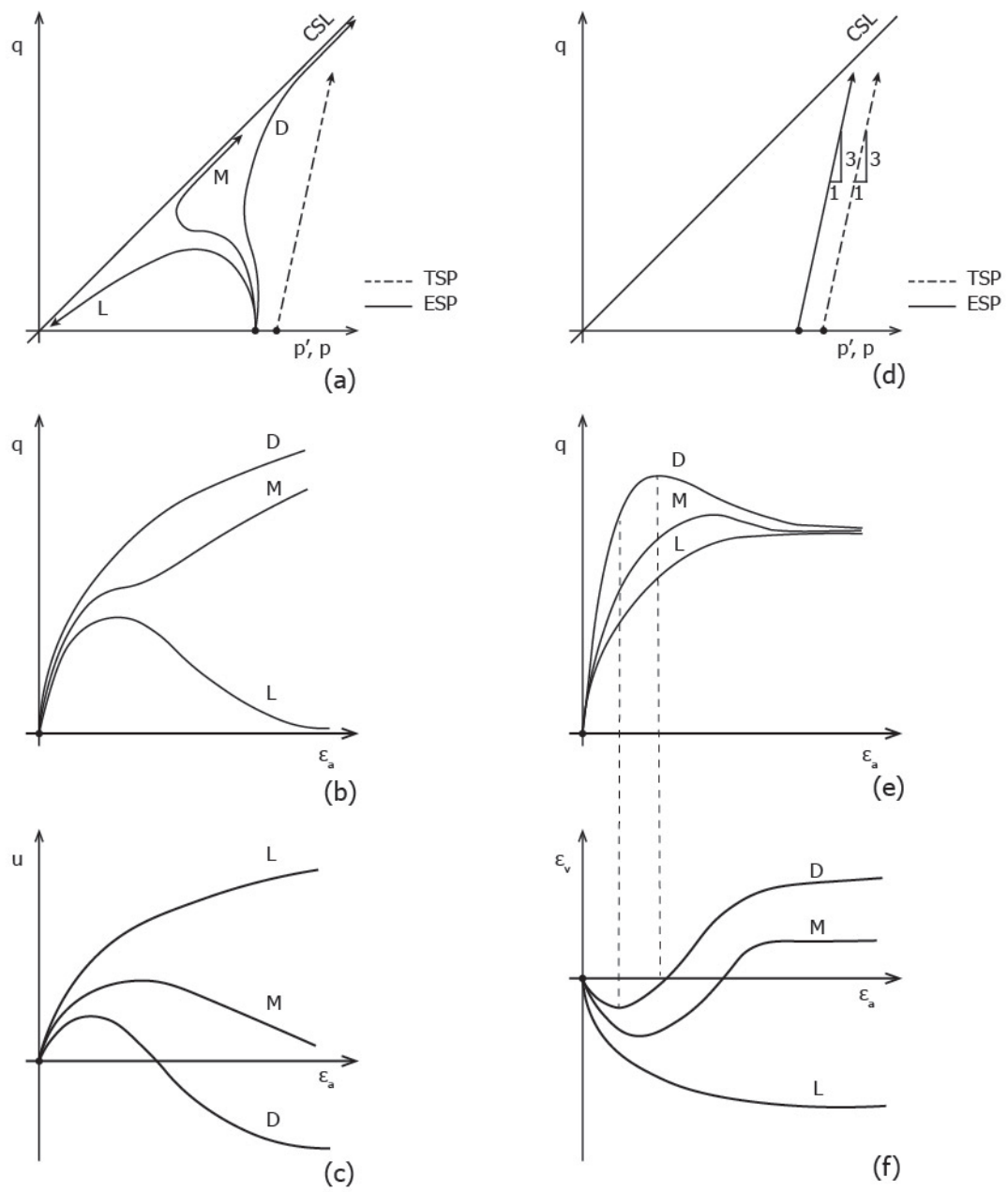


Figure A.2: Theoretical undrained (left) and drained (right) triaxial test results of saturated sands for loose (L), medium (M) and dense (D) samples, based on Baladi (1978)

B | Cone penetration test results

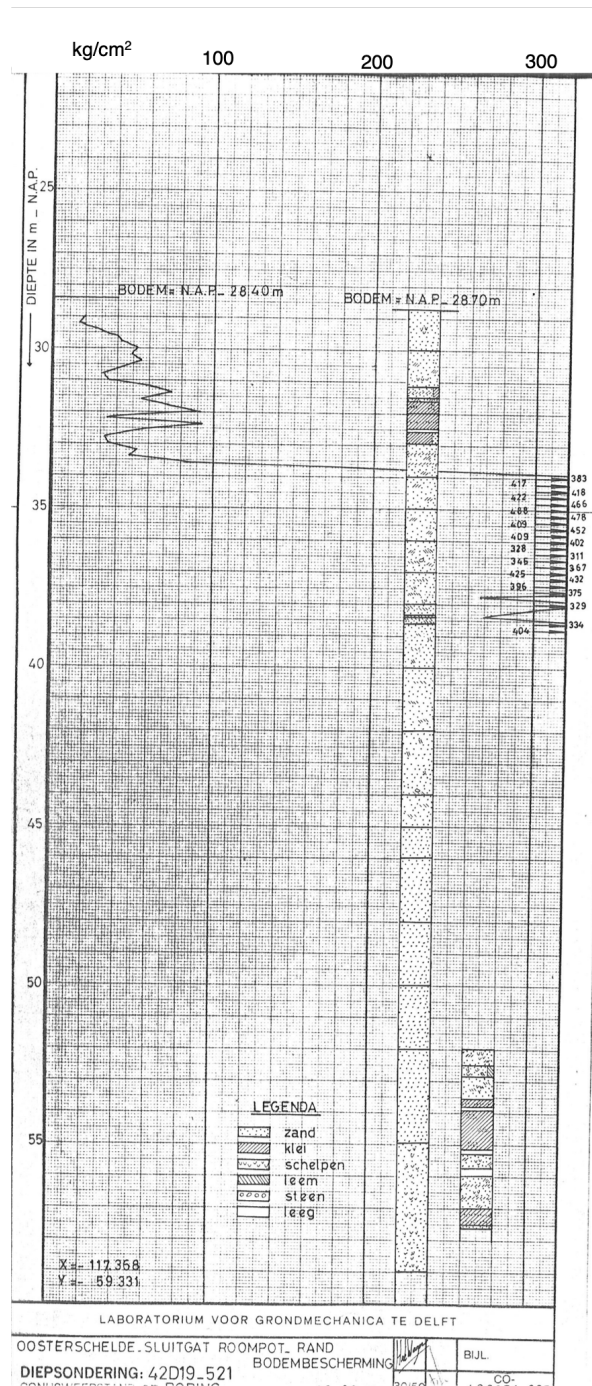


Figure B.1: Cone resistance in kg/cm² (Dinoloket, 2014)

APPENDIX B. CONE PENETRATION TEST RESULTS

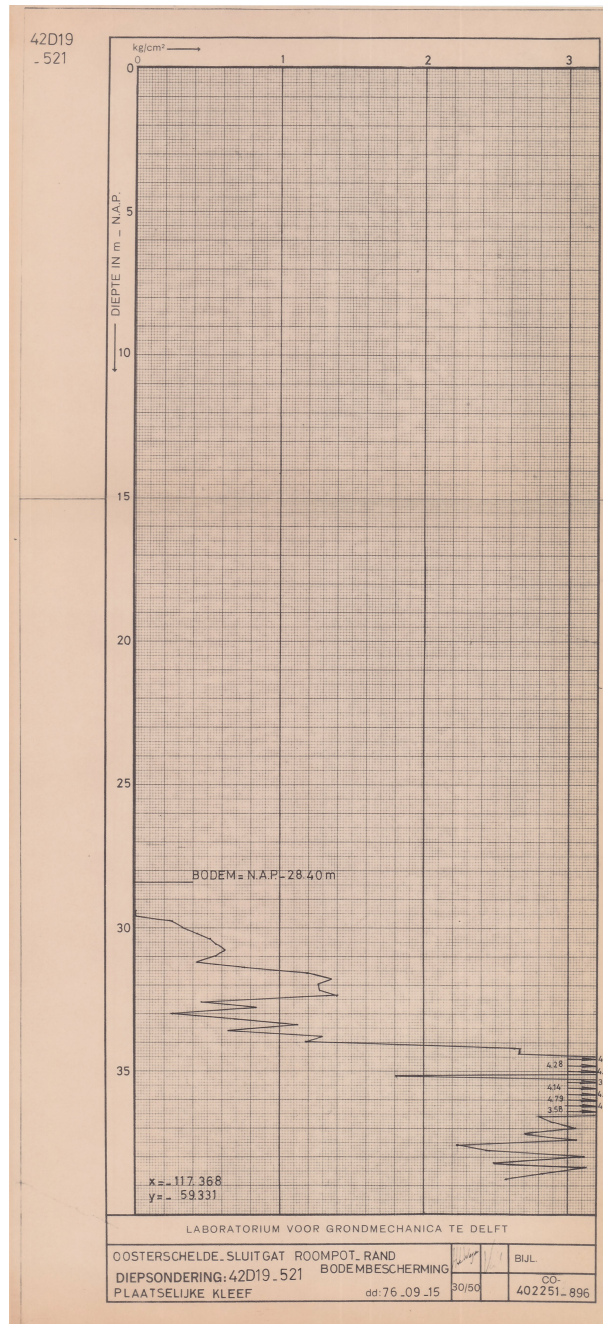


Figure B.2: Sleeve friction in kg/cm² (Dinoloket, 2014)

C | Density electrical measurements

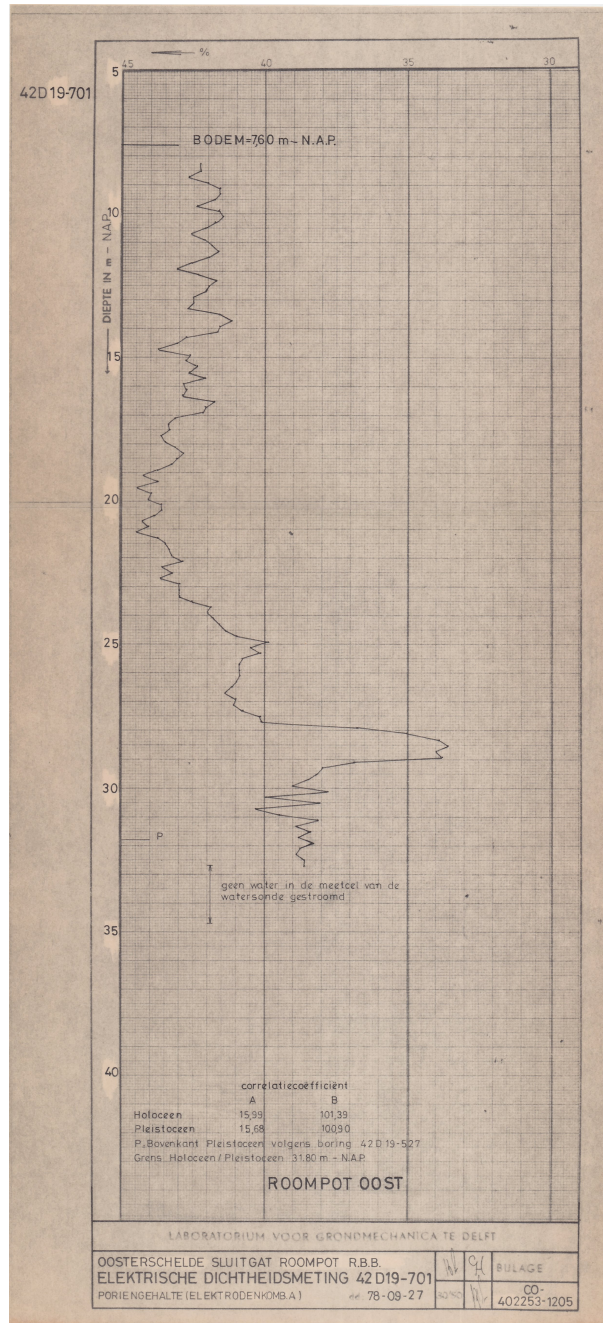


Figure C.1: Density measurement at point 1

APPENDIX C. DENSITY ELECTRICAL MEASUREMENTS

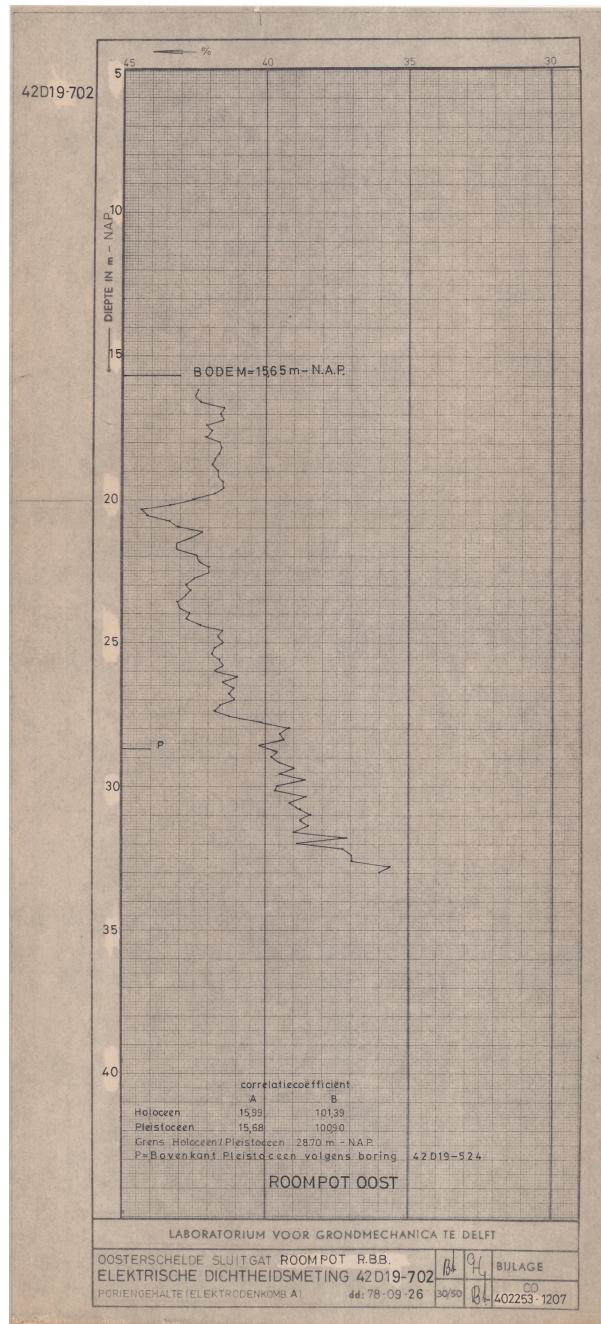


Figure C.2: Density measurement at point 2

APPENDIX C. DENSITY ELECTRICAL MEASUREMENTS

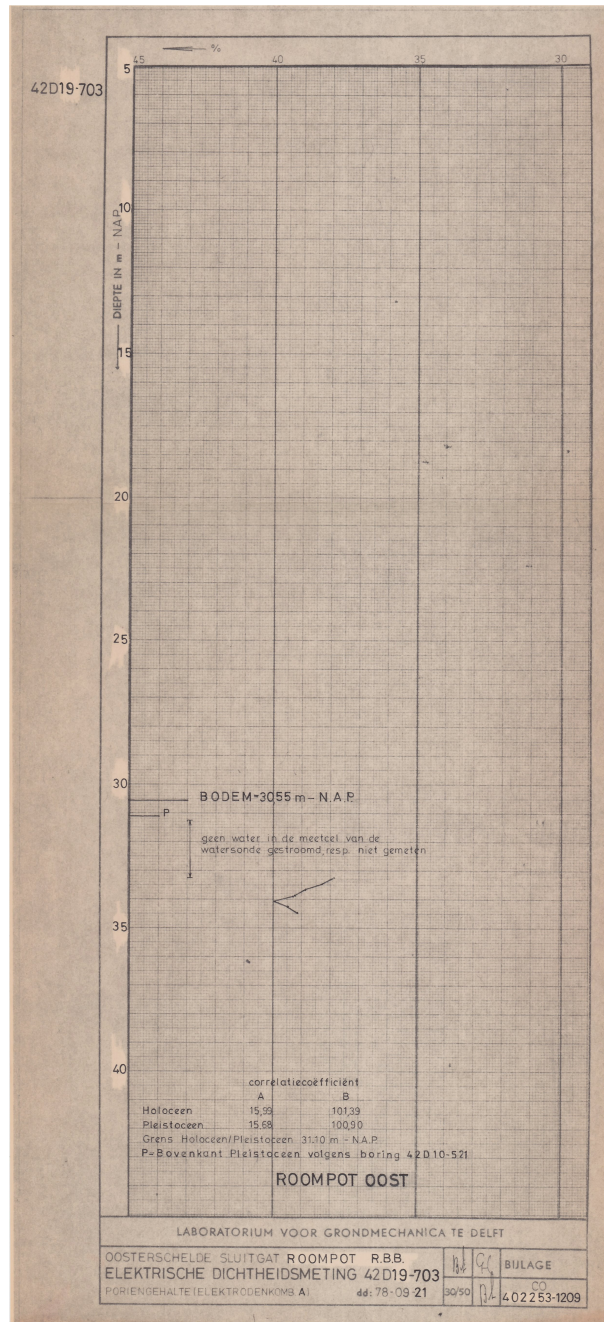


Figure C.3: Density measurement at point 3

APPENDIX C. DENSITY ELECTRICAL MEASUREMENTS

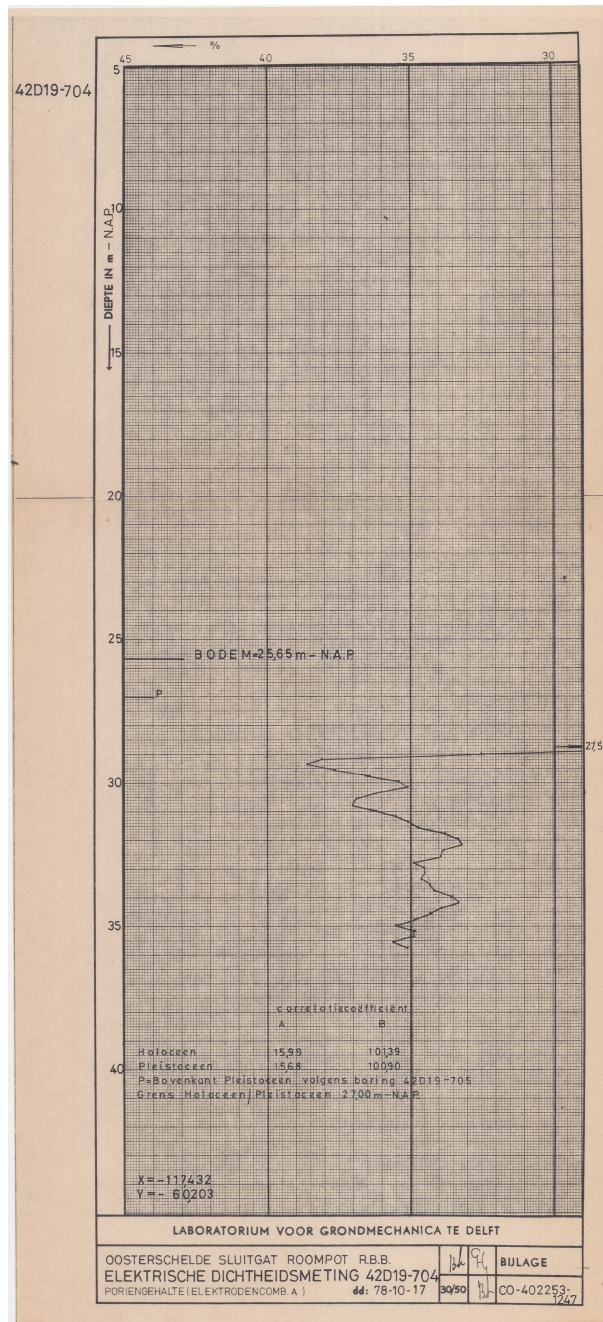


Figure C.4: Density measurement at point 4

D | Grain size distribution

The grain size distribution of the laboratory soil and the in-situ soil are presented in figure D.1. The steepness and shape of the laboratory soil grain size distribution and the in-situ soil grain size distribution are similar for most of the samples resulting in the same uniformity. Because the grain size distribution of the laboratory soil is uniform, the particle segregation is assumed to be low during triaxial sample preparation. Therefore, the samples are closer to a fully homogeneous soil which is not the case in the field, but it is important for element testing because the sample is representing one point inside the soil and the tests are reproducible.

Both soil types consist mainly out of sand (0.063-2mm) and they are uniformly distributed, except for the in-situ sample at 54.95-59.48 m-NAP. The average grain size of the laboratory sand is smaller than the in-situ sand. Therefore, the laboratory soil is expected to be a bit more prone to liquefaction. Triaxial test on in-situ sand can be done to check if this expectation is correct. Both soil types belong to the fine sands. However, the in-situ soil also contains fines. The fines content, which can significantly affect the undrained behaviour (Yoshimine, Robertson, & Fear Wride, 1999), is smaller for the laboratory sand than the in-situ sand. Clean sand is used in the triaxial experiments to avoid the complexity of fines.

The laboratory sand possess a general angular roundness. This shape is different than the shape of the sand in the field. The sand in the field is transported by the water, by the rivers or sea, and generally, this sand has a rounded shape. The laboratory sand is coming from a quarry. The reason why the laboratory sand is selected is because the sand is uniform and available in large quantities which is one of the main factors that is needed to make tests reproducible. Another reason is that this sand is used for the liquefaction tank and therefore the results of this research can be used for a comparison of the liquefaction tank results.

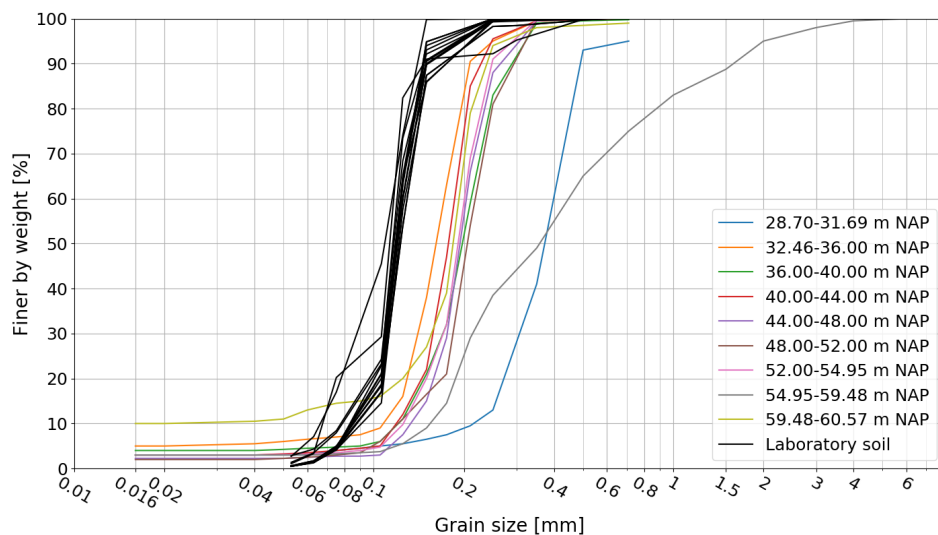


Figure D.1: Grain size diagram for the in situ and laboratory soil with the depth below NAP

E | Parameters triaxial test

The triaxial test input values, raw data and calculated parameters for analysing the triaxial results are listed in this Appendix.

E.1 Input parameters

The input parameters are the geometry parameters of the cylindrical sample.

- H_0 → Initial height (mm)
- D_0 → Initial diameter (mm)
- V_0 → Initial volume (mm³): $V_0 = 1/4 * \pi * D_0^2 * H_0$
- A_0 → Initial area (mm²): $A_0 = 1/4 * \pi * D_0^2$

E.2 Raw data

The raw data values are:

- t → Time this stage (h:m:s): Time since start of test (s) and Time since start of stage (s)
- σ_r → Radial stress (kPa): Radial pressure (kPa)
- V → Cell volume (mm³): Radial Volume (mm³)
- σ_b → Back pressure (kPa)
- V_b → Back volume (mm³)
- L_c → Load cell (kN)
- w_a → Axial displacement (mm), measured when docked and when undocked it should be calculated with (uses volume change measurement): $w_a = H_0 - (H_0((V_0 + \Delta V_b)/V_0)^{\frac{1}{3}})$
- u → Pore pressure (kPa)

E.3 Calculated parameters

- F_a → Axial force (kN), $F_a = L_c + \sigma_r A$
- ϵ_a → Axial strain (%), $\epsilon_a = (w_a/H_0) * 100$
- ΔD_{avg} → Avg. diam. change (mm): $\Delta D_{avg} = \sqrt{\frac{4A}{\pi}}$
- ϵ_r → Radial strain (%): $\epsilon_r = \frac{D_{avg}}{D_0} * 100$
- σ_a → Axial stress (kPa): $\sigma_a = \frac{F_a}{A/1000000}$
- σ'_a → Eff. axial stress (kPa): $\sigma'_a = \sigma_a - u$
- σ'_r → Eff. radial stress (kPa): $\sigma'_r = \sigma_r - u$
- q → Deviator stress (kPa): $q = \sigma_a - \sigma_r$
- A → Current area (mm²): $A = \frac{((1/4) * \pi * (D_0)^2 * H_0) + V_B}{H_0 - w_a}$
- p → Cambridge (kPa): $p = \frac{\sigma_a + 2 * \sigma_r}{3}$

- $p' \rightarrow$ Eff. Cambridge (kPa): $p' = \frac{\sigma'_a + 2 * \sigma'_r}{3}$
- $\Delta V \rightarrow$ Volume change (mm^3): $\Delta V = V_B$
- $B \rightarrow$ B-value: $B = \frac{\Delta u}{\Delta \sigma_r}$

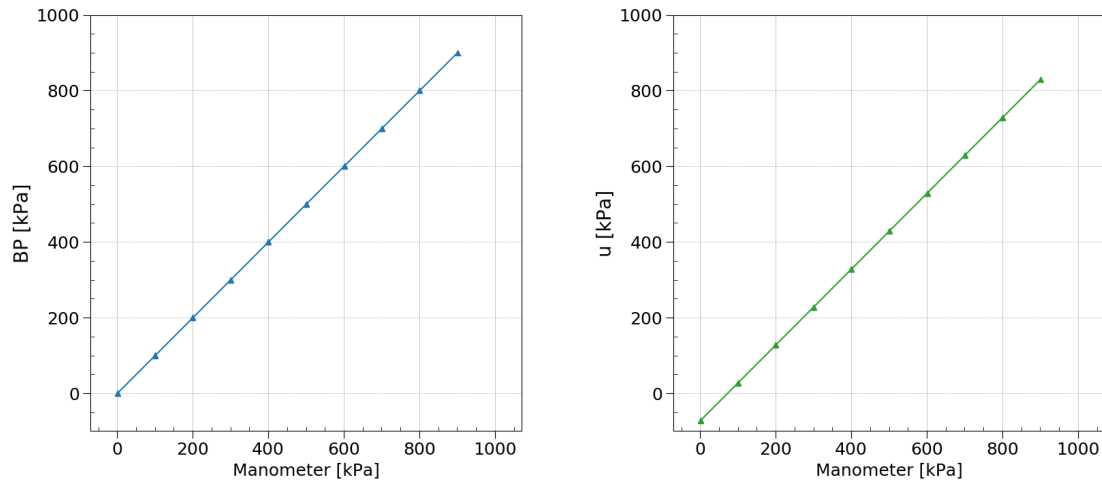
E.4 Calculated soil parameters

- $c_v \rightarrow$ Consolidation coefficient: $c_v = k / (\gamma_w * m_v)$ and $c_v = 0.848h^2 / t_{90\%}$, with h is drainage path.
- $m_{tot} \rightarrow$ Total mass: $m_{tot} = m_d + m_w$
- $V_{tot} \rightarrow$ Total volume: $V_{tot} = V_s + V_v$
- $\gamma_d \rightarrow$ Dry unit weight: $\gamma_d = \frac{m_d * g}{V_{tot}}$
- $\gamma_{sat} \rightarrow$ Saturated unit weight ($S = 1$): $\gamma_{sat} = \frac{m_{tot}}{V_{tot}} * g$
- $\gamma_s \rightarrow$ Unit weight of the aggregate soil solids: $\gamma_s = \frac{m_d}{V_s} * g$
- $G_s \rightarrow$ Specific gravity: $G_s = \frac{\gamma_s}{\frac{\gamma_{wat}}{V_v}}$
- $e \rightarrow$ Void ratio: $e = \frac{n}{1 - n} = \frac{V_v}{V_s} = \frac{G_s \gamma_w}{\gamma_d} - 1 = \frac{V_{tot}(G_s * \gamma_w)}{m_d * g} - 1$
- $n \rightarrow$ Porosity: $n = \frac{e}{1 + e} = \frac{V_v}{V_{tot}}$
- $RD \rightarrow$ Relative density: $RD = \frac{e_{max} - e}{e_{max} - e_{min}}$
 $e_{min} = 0.64$
 $e_{max} = 1.07$
- $w \rightarrow$ Water content: $w = W_w / W_s$

F | Calibration of the triaxial setup

Calibration of the triaxial controllers was conducted before performing the triaxial test. First, the pore water pressure (u) and back pressure (BP) calibration coefficients were checked by a digital manometer. Secondly, the offsets of the cell pressure (CP) controller, back pressure controller and pore water pressure sensor were determined. Thirdly, the deformability of the triaxial cell and connections was checked.

The calibration coefficients of 0.9997 and 1.0014 for the back pressure and pore water pressure respectively are accepted for the triaxial tests.



(a) Back pressure:
 $y = 0.9997x - 0.7592, R^2 = 1$

(b) Pore water pressure:
 $y = 1.0014x - 72.943, R^2 = 1$

Figure F.1: Calibration of the back pressure controller and pore water pressure sensor with a digital manometer including the formulas of the trend line and coefficient of determination

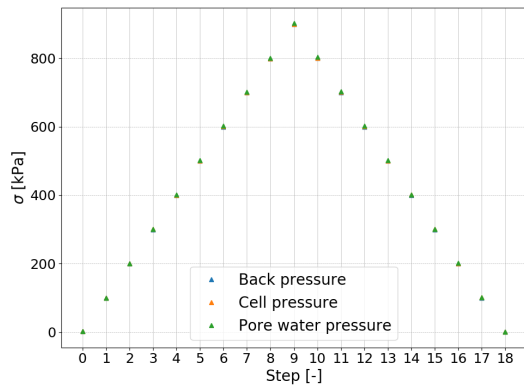
The offsets of the controllers and pore water pressure sensor were determined by filling the cell halfway with water, which is halfway the sample height. The readings of the back pressure, cell pressure and pore water pressure sensors were set to zero and equal to:

- BP: -4.5 kPa
- CP: 55.6 kPa
- PWP: 68.5 kPa

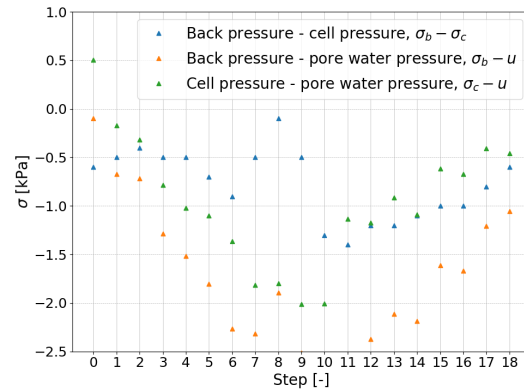
After this step, the controllers and sensor were connected to the triaxial cell filled by water and the back pressure was increased in steps of 100 kPa starting from 0 kPa (step 0). When 900 kPa (step 9) was reached, the back pressure was decreased to 0 (step 18) by applying the same step size. The differences of pressure readings are shown in figure F.2. The back pressure calibration coefficient is closer to 1.0000, therefore the additional offsets of the pore water pressure sensor and cell pressure controller were determined by their differences with the back pressure controller. It is assumed that the deformability of the back pressure tube is negligible. However, when the calibration coefficient of the pore water pressure was closer to 1.0000 than selecting this sensors

for defining the differences and additional offsets would be preferable. The additional offsets can be determined by applying the differences of figure F.2b for the pressure ranges that will be applied in the triaxial tests. However, in this study the average differences between the back pressure and cell pressure and back pressure and pore water pressure readings are applied to define the final offsets:

- offset BP: -4.5 kPa
- offset CP: $55.6 + -0.8 = 54.8$ kPa
- offset PWP: $68.5 + -1.7 = 66.8$ kPa



(a) The imposed BP and overlapping CP and PWP readings



(b) Differences between BP, CP en PWP readings

Figure F.2: Determination of the offsets and deformability of the triaxial setup

G | Isotropically consolidated drained and undrained test results for low confining pressure

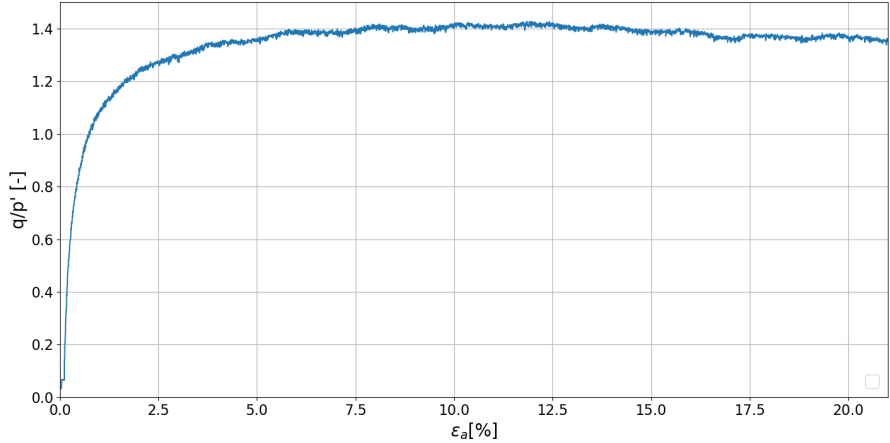


Figure G.1: Consolidated drained triaxial test results: normalised deviatoric stress versus axial strain for low effective confining pressure ($p' = 14$ kPa)

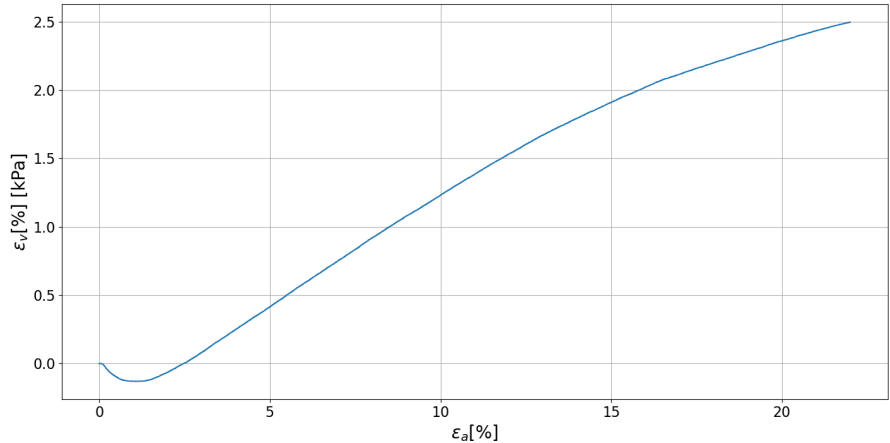


Figure G.2: Consolidated drained triaxial test results: volumetric strain versus axial strain for low effective confining pressure ($p' = 14$ kPa)

APPENDIX G. ISOTROPICALLY CONSOLIDATED DRAINED AND UNDRAINED TEST RESULTS FOR LOW CONFINING PRESSURE

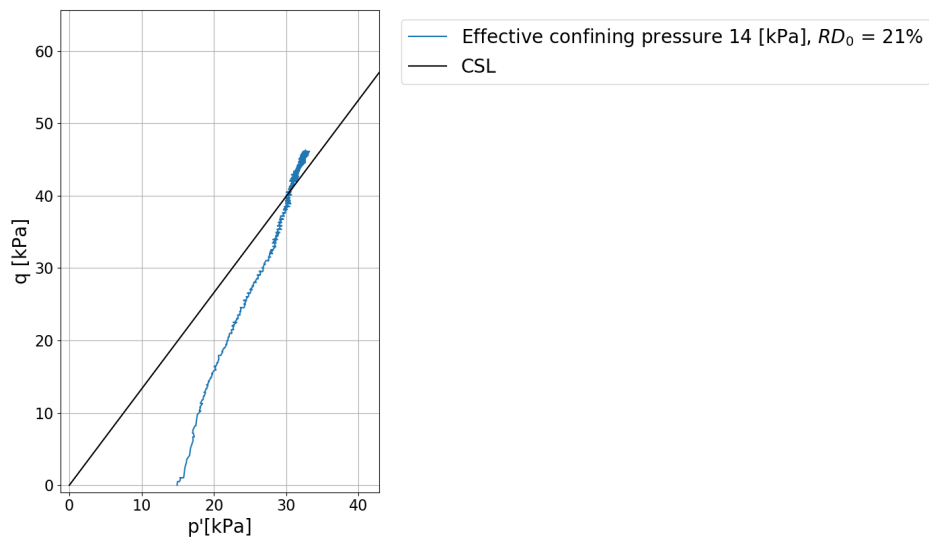


Figure G.3: Consolidated drained triaxial test results: effective stress path for low effective confining pressure ($p' = 14$ kPa) with critical state line (CSL)

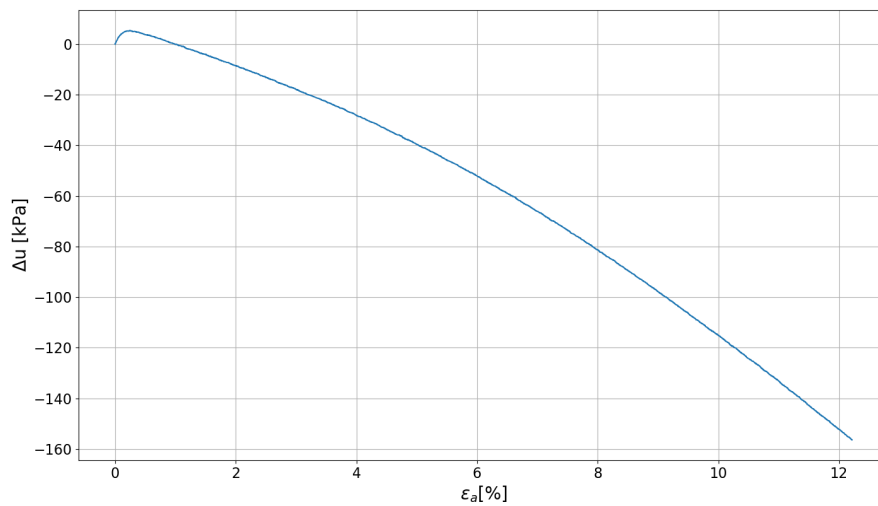


Figure G.4: Consolidated undrained triaxial test results: excess pore water pressure versus axial strain for low effective confining pressure ($p' = 14$ kPa)

APPENDIX G. ISOTROPICALLY CONSOLIDATED DRAINED AND UNDRAINED TEST RESULTS FOR LOW CONFINING PRESSURE

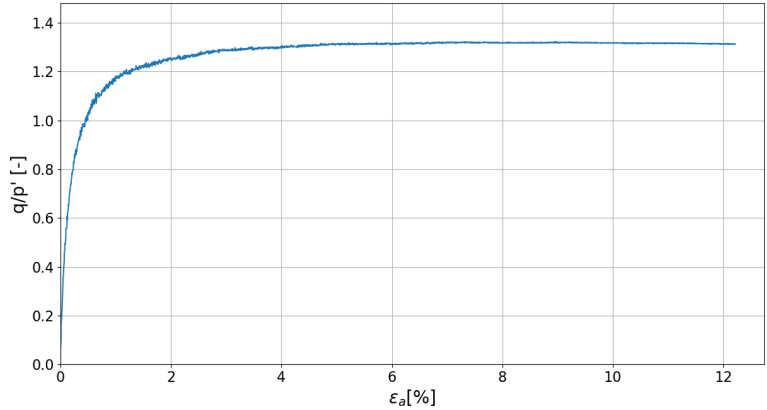


Figure G.5: Consolidated undrained triaxial test results: normalised deviatoric stress versus axial strain for low effective confining pressure ($p' = 14$ kPa)

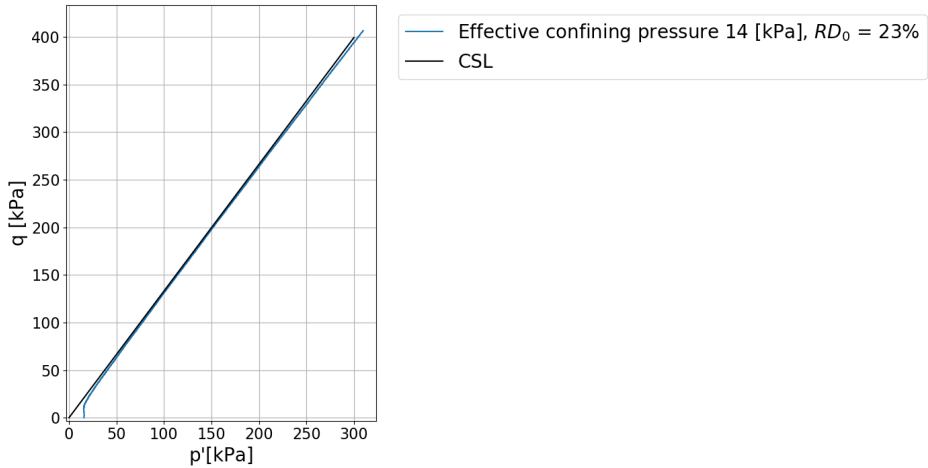
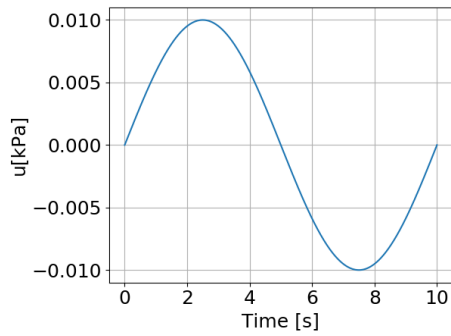


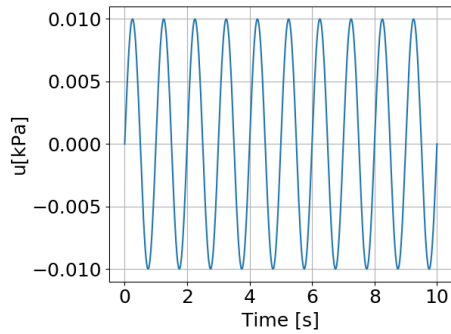
Figure G.6: Consolidated undrained triaxial test results: effective stress path for low effective confining pressure ($p' = 14$ kPa) with critical state line (CSL)

H | Excess pore water pressure results

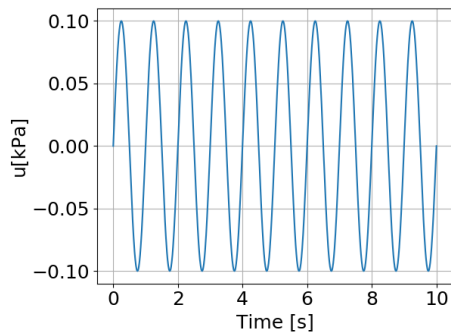
The excess pore water pressure for different combinations of amplitude and period of the harmonic head at the bed are depicted in this appendix.



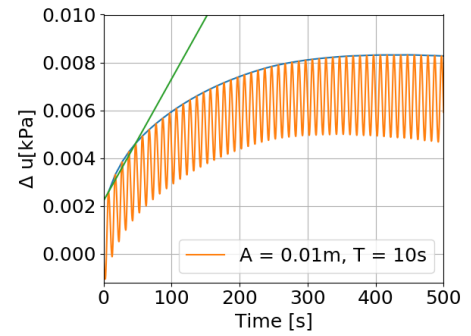
(a)



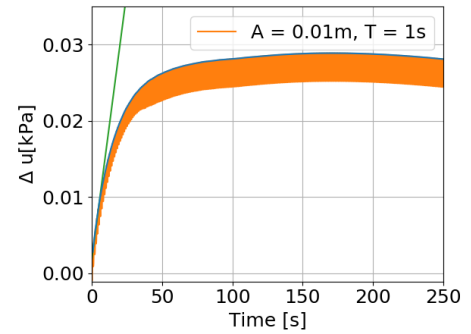
(c)



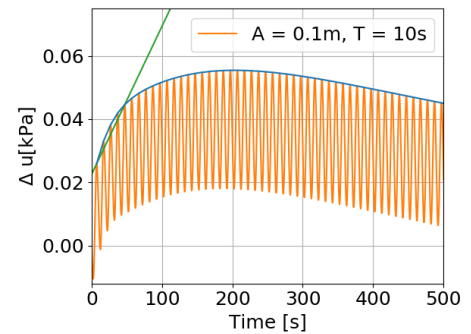
(e)



(b)

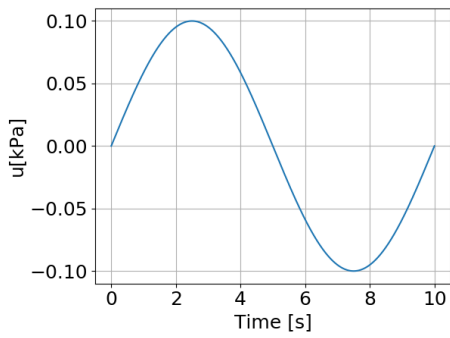


(d)

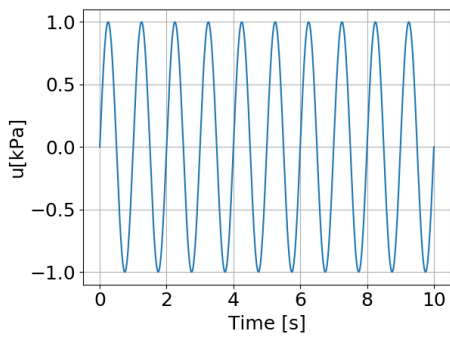


(f)

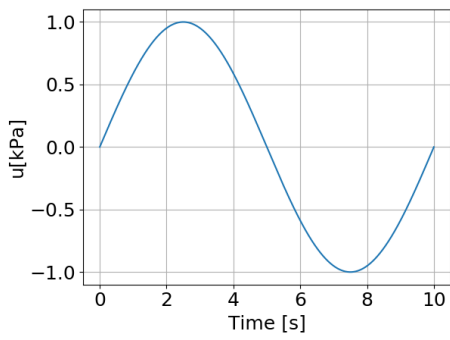
APPENDIX H. EXCESS PORE WATER PRESSURE RESULTS



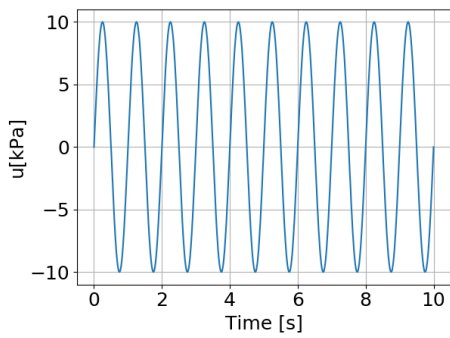
(g)



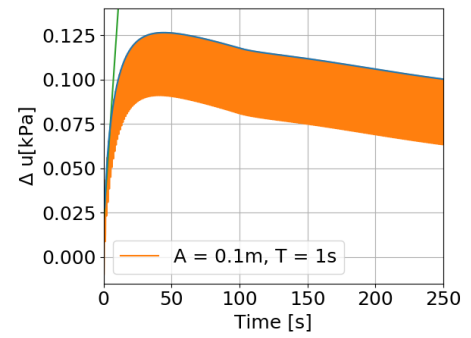
(i)



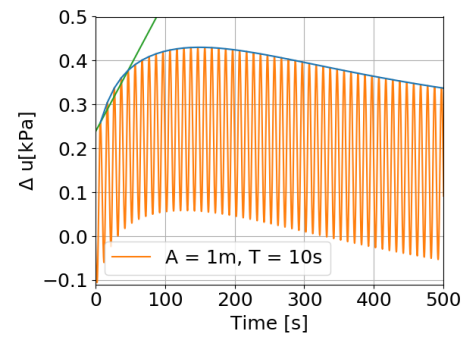
(k)



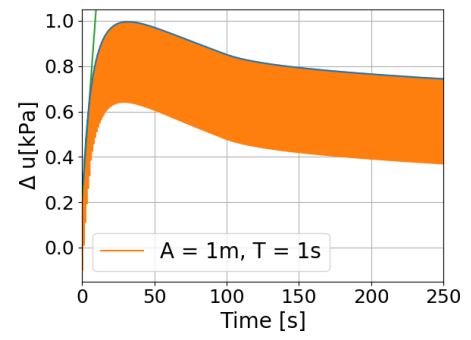
(m)



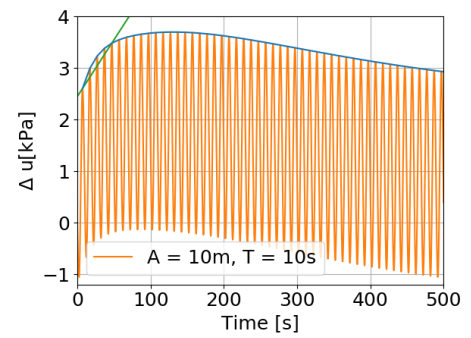
(h)



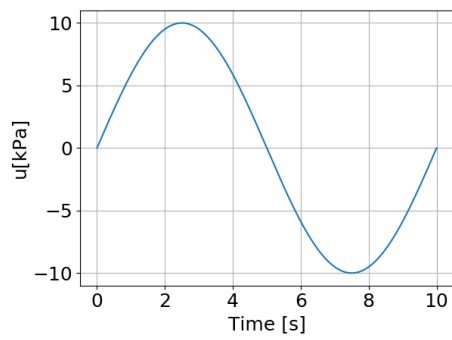
(j)



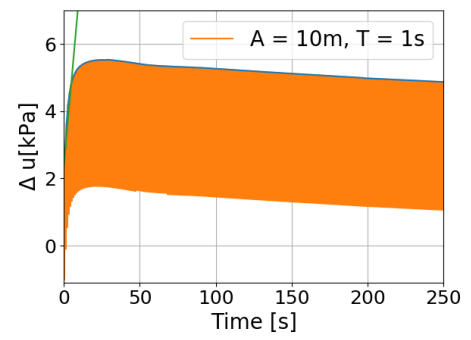
(l)



(n)



(o)



(p)

Figure H.1: The rate of excess pore water pressure build up for every combination of amplitude and period for the harmonic head at the bed

I | Uncertainties

The uncertainties of the measured parameters and initial parameters of the triaxial tests are listed in table I.1. The uncertainties of the back pressure sensor, cell pressure sensor and load cell sensor are defined by GDS instruments which is 1% of the maximum capacity. The maximum capacity is 1MPa for the controllers and 1kN for the load cell sensor. The uncertainty of the back pressure volume controller is 300mm³ as reported by Muraro (2019). The LVDT uncertainty is assumed to be 0.5mm in which tilting of the sensor is taken into account. Furthermore, the uncertainties for the dimensions of the sample are 1mm and 0.5mm for the height and diameter respectively. In this research multiple parameters are calculated with the measurements and initial parameters as input values. The uncertainties of these calculated parameters are defined by a normal random number generator with a standard deviation (σ_{std}) of a third of the uncertainty of table I.1. The uncertainty is assumed to be equal to 3σ . So the distribution of the measured and initial parameters is assumed to be normal. The mean is assumed to be the measured value. Arrays of a 100.000 normal distributed random numbers are used to calculate the parameters of table I.1. The probability density function of the deviatoric stress is given in figure I.1. All in all, the uncertainty depends on the selected values, so for every data point the uncertainty differs.

Uncertainties of the triaxial test measurements and initial conditions				
Parameter	Symbol	Value (μ)	Uncertainty (3σ)	Unit
Back pressure	σ_{BP}	599.4	1	kPa
Pore water pressure	u	599.2	1	kPa
Radial stress (cell pressure)	σ_r	615.5	1	kPa
Load cell	L_c	0.026	1	kN
Back pressure volume	V_{BP}	1231	300	mm ³
Axial displacement (LVDT)	w_a	1.8	0.5	mm
Initial sample height	H_0	103.9	1	mm
Initial diameter sample	D_0	49.4	0.5	mm

Table I.1: Uncertainties of the triaxial test measurement and initial conditions with its mean value based on test 1

Uncertainties of the calculated triaxial test parameters				
Parameter	Symbol	Exp. value	Uncertainty (\pm)	Unit
Initial area	A_0	1920.1	38.8	mm^2
Initial volume	V_0	199439.5	4146.5	mm^3
Volume	V	200670.6	4147.4	mm^3
Area	A	1942.1	13.6	mm^2
Diameter change	D_{avg}	0.28	0.13	mm
Axial strain	ε_a	1.74	0.48	%
Radial strain	ε_r	0.57	0.25	%
Volumetric strain	ε_v	0.62	0.15	%
Axial force	F_a	1.221	0.025	kN
Axial stress	σ_a	628.9	1.2	kPa
Effective axial stress	σ'_a	29.7	1.5	kPa
Effective radial stress	σ'_r	16.3	1.4	kPa
Deviatoric stress	q	13.4	0.6	kPa
Mean total stress	p	620.0	1.0	kPa
Mean effective stress	p'	20.8	1.4	kPa

Table I.2: Table of the uncertainties of the calculated triaxial test parameters with the expected value based on normal distributed input parameters of table I.1 and the equations in appendix E

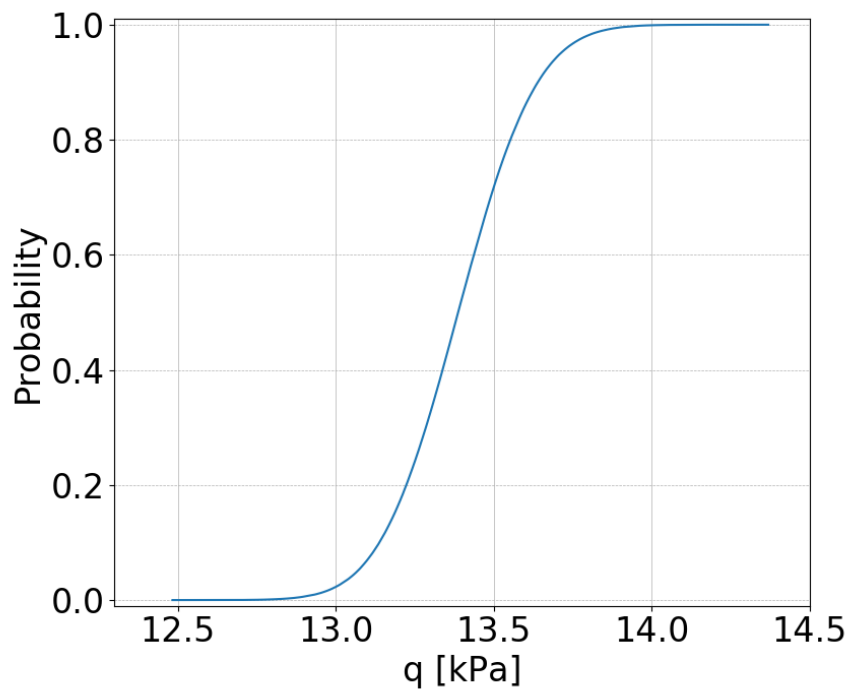


Figure I.1: Cumulative density function of the deviatoric stress in kPa

J | Graphs difference back pressure and pore water pressure versus time

The differences in back pressure and pore water pressure are plotted versus time in figure J.1. It looks like the differences have a wave shape with a period of approximately 600 seconds. Another trend of the difference in back pressure and pore water pressure versus time could not be found. The differences are larger for test 2 and test 6. A reason for this could be an inaccurate offset of the back pressure controller or pore water pressure sensor.

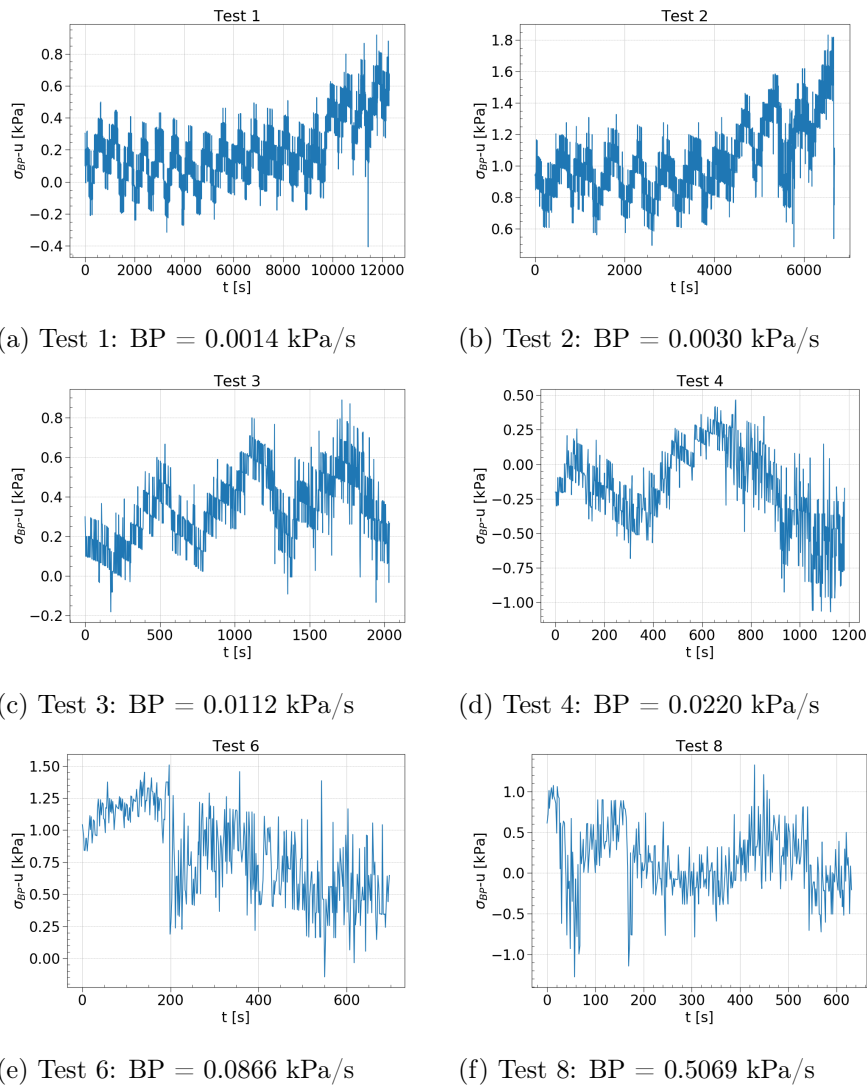


Figure J.1: The difference between the back pressure and pore water pressure versus time of the advanced triaxial tests with increasing back pressure rate

K | Turning point: drop deviatoric stress

At the beginning of each test the deviatoric stress is slightly decreasing. An example of this decrease is given in figure K.1. This decrease is caused by the area correction which is calculated by the volume change. The area correction is not implemented in the settings of the triaxial setup but applied in the data analysis. The drop in deviatoric stress due to the area correction is relatively small. For this reason, it is not taken into account for the selection of the point at which the deviatoric stress starts to drop. The deviatoric stress, without the area correction, is equivalent to the load cell measurements. Therefore, the load cell data is used to obtain the point at which the deviatoric stress drops. The load cell data is divided by its initial value (L_{c0}) and plotted versus time in figure K.2. The deviatoric stress is fluctuating constantly. This fluctuation is a result of the settings of the controllers which work by a feedback loop system. The steps of the load cell measurements are approximately 0.038kN, which is equal to the tolerance of the load cell sensors (1N) divided by initial load cell measurement. The star point is selected just before the load cell does not recover to the initial value anymore. The time corresponding to this point is expected to be the time at which the deviatoric stress starts to drop.

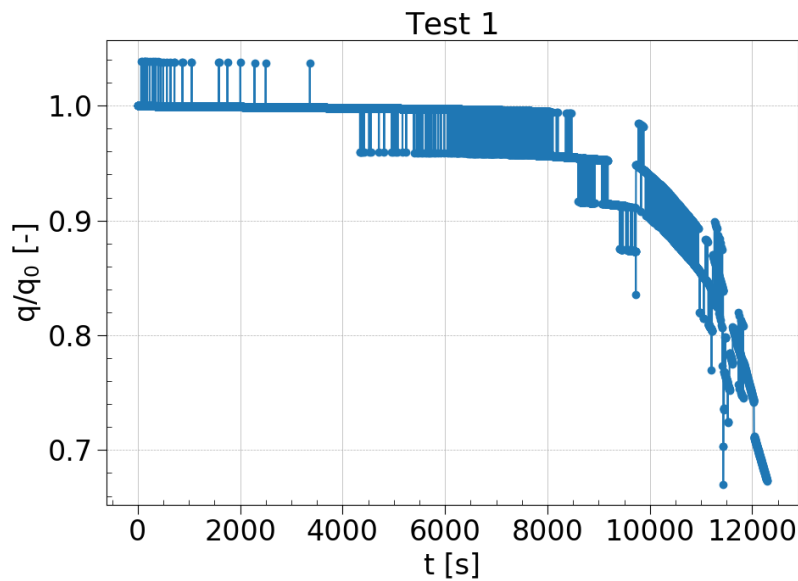
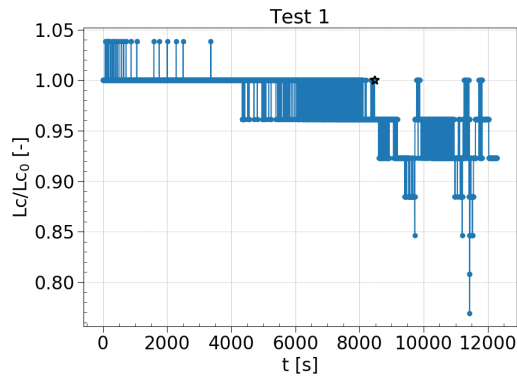
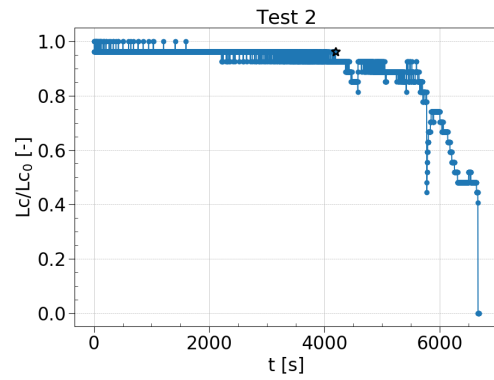


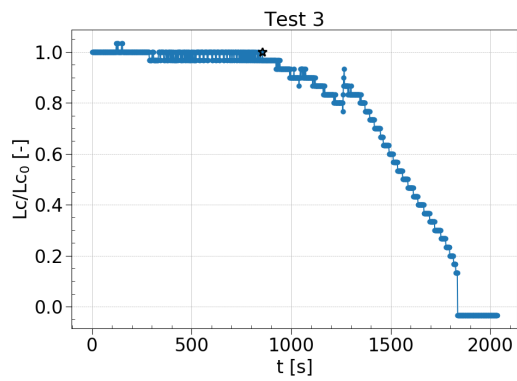
Figure K.1: Normalised deviatoric stress plots versus time of the advanced triaxial tests for test 1



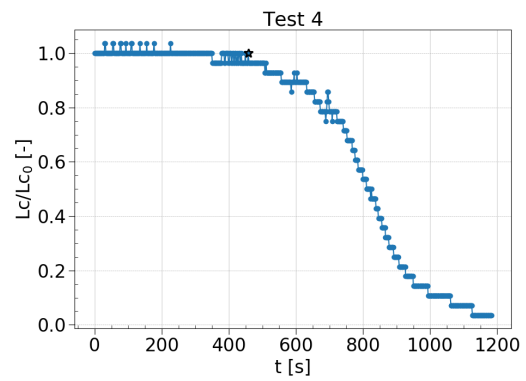
(a) Test 1: BP = 0.0014 kPa/s



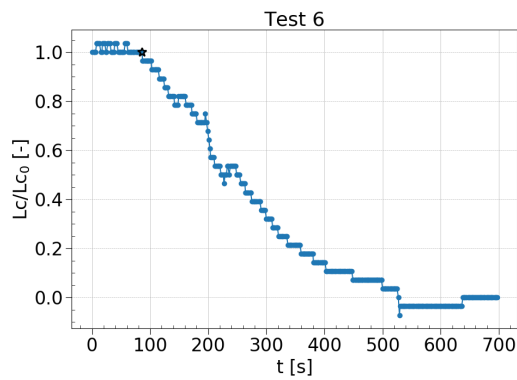
(b) Test 2: BP = 0.0030 kPa/s



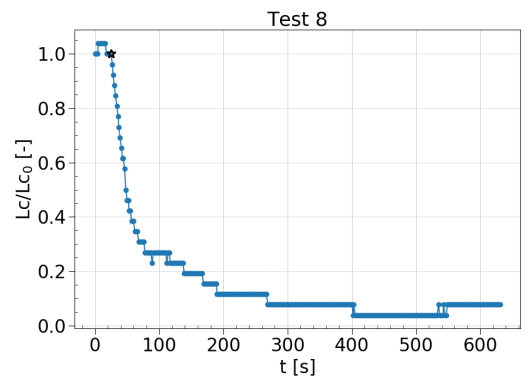
(c) Test 3: BP = 0.0112 kPa/s



(d) Test 4: BP = 0.0220 kPa/s



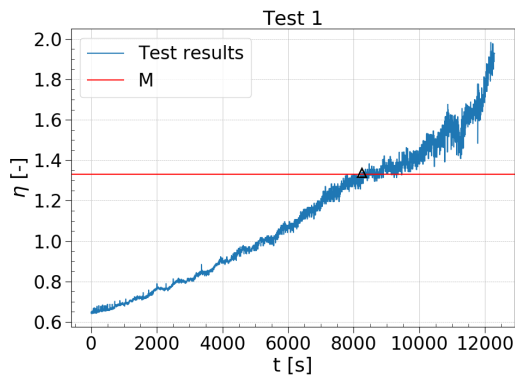
(e) Test 6: BP = 0.0866 kPa/s



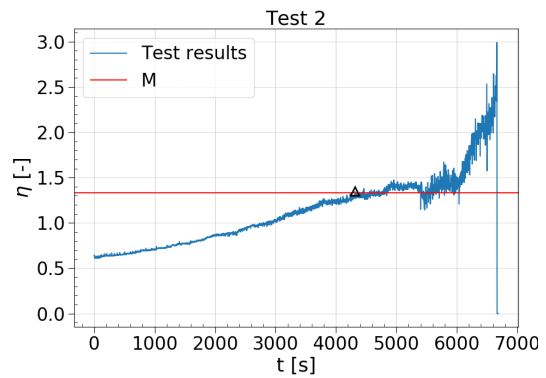
(f) Test 8: BP = 0.5069 kPa/s

Figure K.2: Normalised deviatoric stress plots versus time of the advanced triaxial tests to determine the point at which the deviatoric stress starts to drop

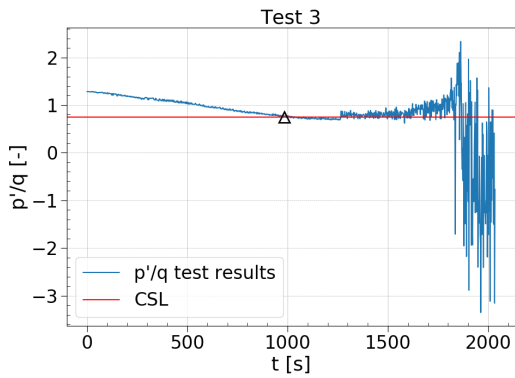
L | Stress ratio of the advanced triaxial tests



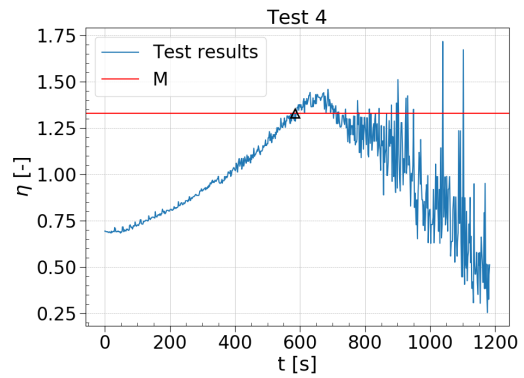
(a) Test 1: BP = 0.0014 kPa/s



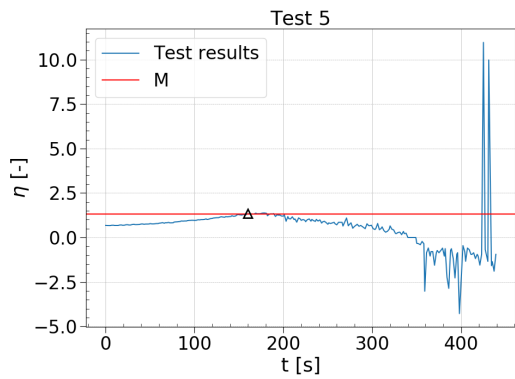
(b) Test 2: BP = 0.0030 kPa/s



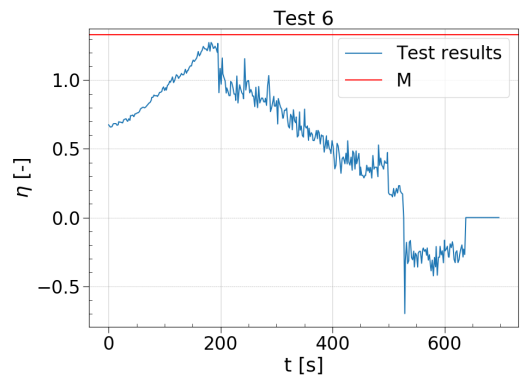
(c) Test 3: BP = 0.0112 kPa/s



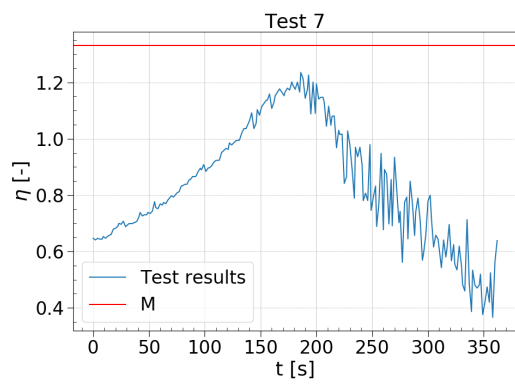
(d) Test 4: BP = 0.0220 kPa/s



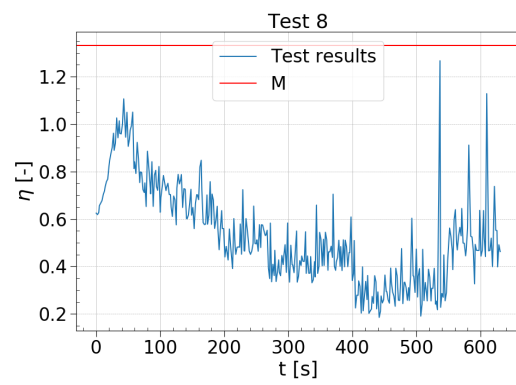
(e) Test 5: BP = 0.0866 kPa/s



(f) Test 6: BP = 0.0866 kPa/s



(g) Test 7: BP = 0.0866 kPa/s

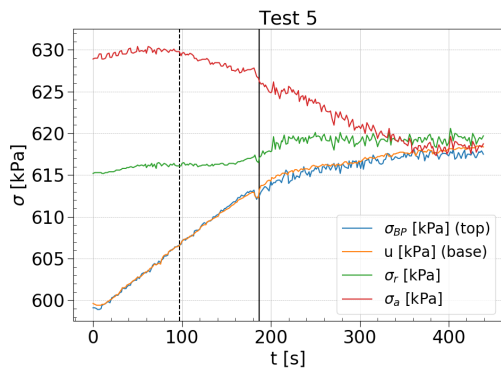


(h) Test 8: BP = 0.5069 kPa/s

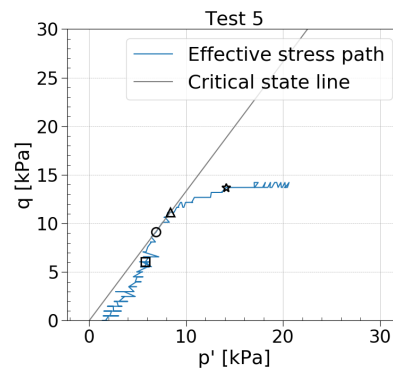
Figure L.1: Effective stress ratio (p'/q) versus time with the predefined critical state stress and the point of reaching the CSL indicated by a triangle for advanced triaxial tests

M | Repeatability advanced triaxial tests

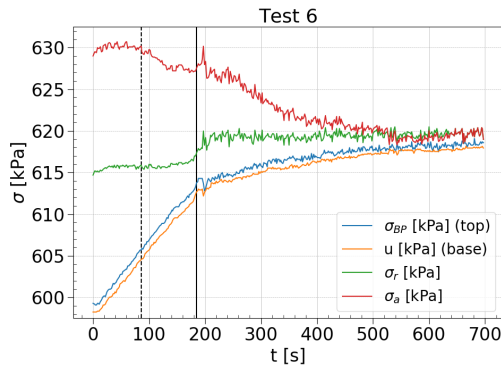
The stresses versus time and the stress paths of test 5, 6 en 7 with a back pressure rate of 0.0866kPa/s are shown in figure M.1.



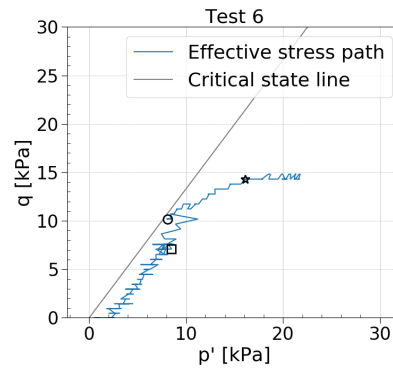
(a) Test 5: BP = 0.0866 kPa/s



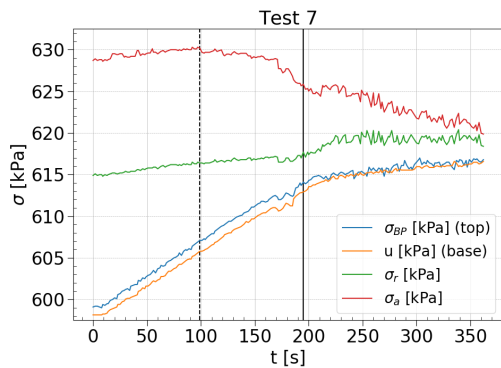
(b) Test 5: BP = 0.0866 kPa/s



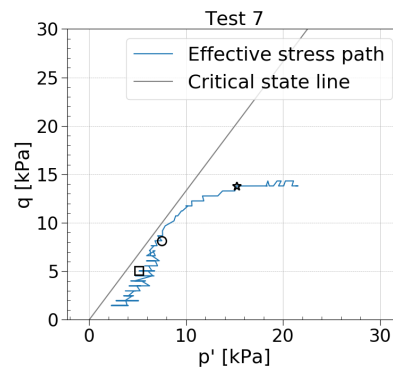
(c) Test 6: BP = 0.0866 kPa/s



(d) Test 6: BP = 0.0866 kPa/s



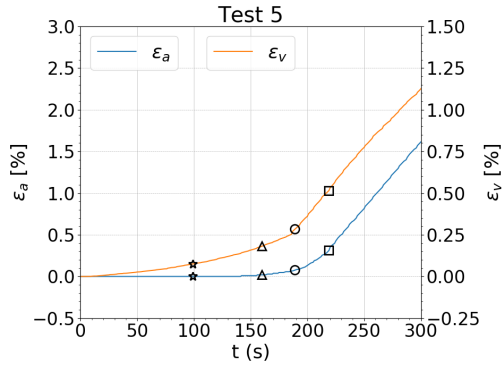
(e) Test 7: BP = 0.0866 kPa/s



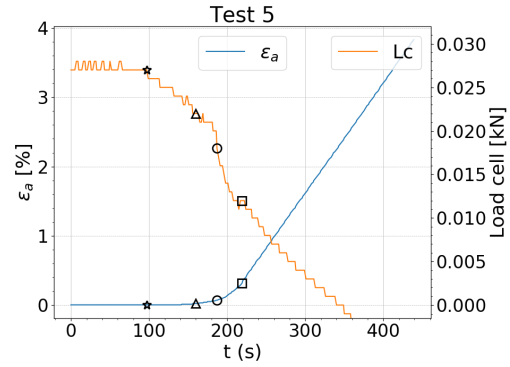
(f) Test 7: BP = 0.0866 kPa/s

Figure M.1: The back pressure, pore water pressure, radial stress and axial stress of the advanced triaxial tests with increasing back pressure rate and the effective stress path

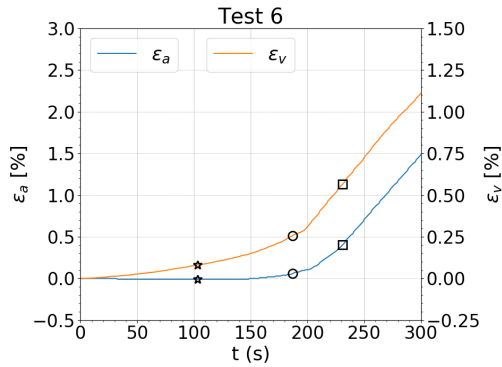
The plots are essentially the same. The differences are due to the length of the tests. Test 6 is longer than test 5 and test 7. The drop in deviatoric stress occurs around 14kPa mean effective stress. Moreover the shape of the strains versus time plots are similar as well as the amount of strain. The shape of the load cell plots differ, this is due to the differences in the x-axis.



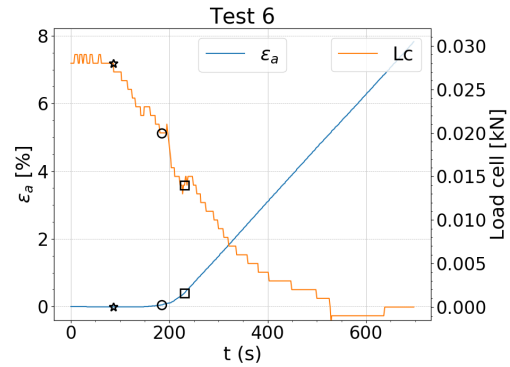
(a) Test 5: BP = 0.0866 kPa/s



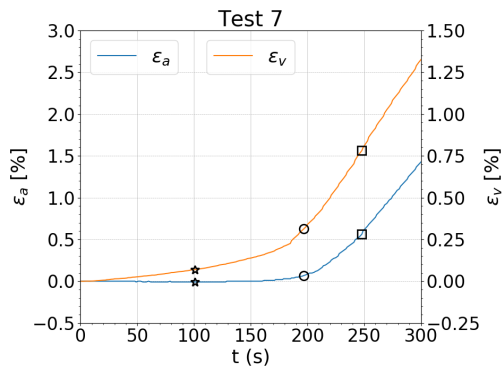
(b) Test 5: BP = 0.0866 kPa/s



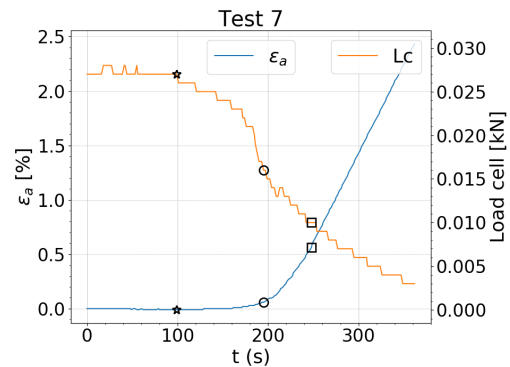
(c) Test 6: BP = 0.0866 kPa/s



(d) Test 6: BP = 0.0866 kPa/s



(e) Test 7: BP = 0.0866 kPa/s



(f) Test 7: BP = 0.0866 kPa/s

Figure M.2: Axial strain, volumetric strain and load cell versus time

N | Anisotropically consolidated undrained triaxial test results

The results of the anisotropically consolidated undrained triaxial test are given in figure N.1 - N.3.

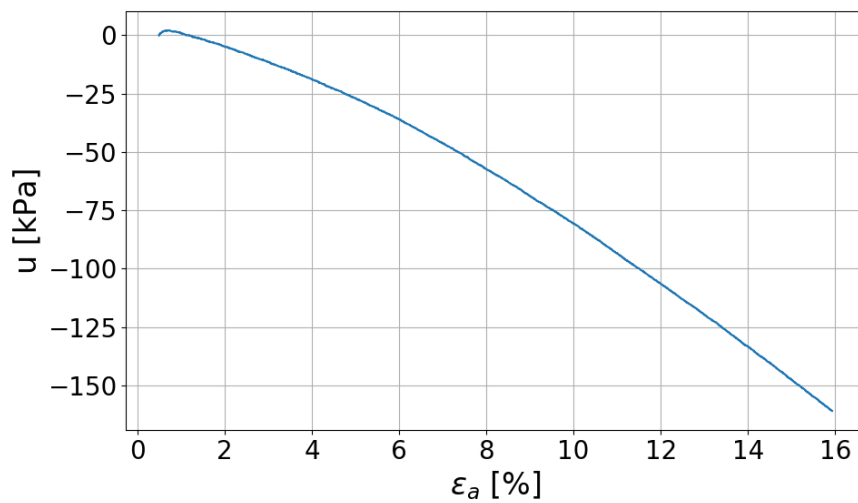


Figure N.1: Anisotropically consolidated undrained triaxial test: pore water pressure versus axial strain for $K_c=0.48$ ($q = 14.8$ kPa and $p' = 618.8$ kPa)

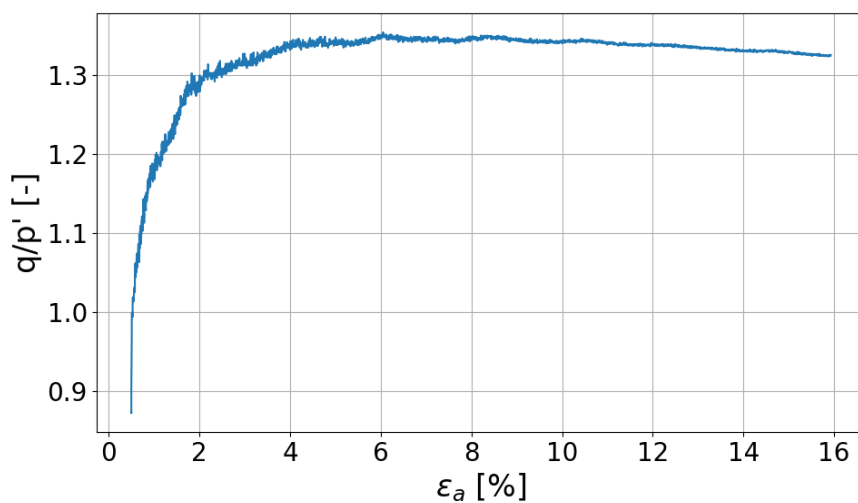


Figure N.2: Anisotropically consolidated undrained triaxial test: normalised deviatoric stress versus axial strain for $K_c=0.48$ ($q = 14.8$ kPa and $p' = 618.8$ kPa)

APPENDIX N. ANISOTROPICALLY CONSOLIDATED
UNDRAINED TRIAXIAL TEST RESULTS

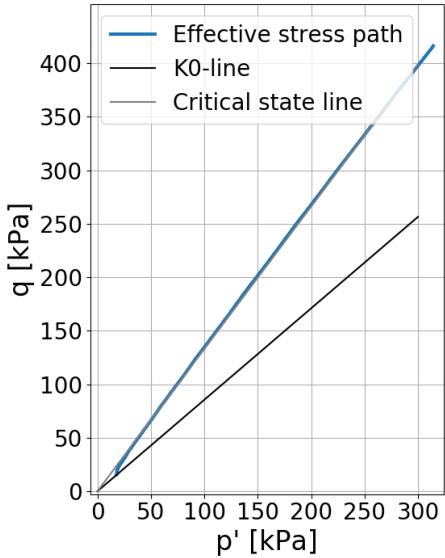
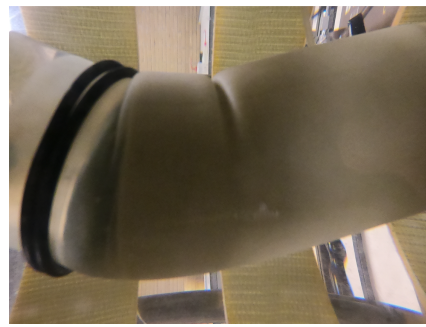


Figure N.3: Anisotropically consolidated undrained triaxial test: effective stress path for $K_c=0.48$ ($q = 14.8$ kPa and $p' = 618.8$ kPa)

O | Observed instabilities triaxial tests



(a) Test 1: BP = 0.0014 kPa/s



(b) Test 2: BP = 0.0030 kPa/s



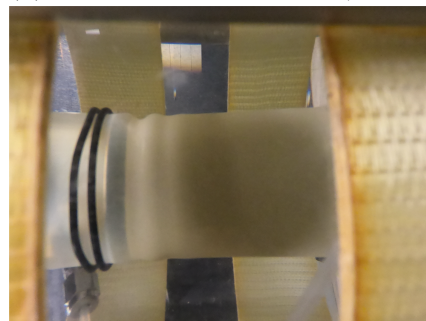
(c) Test 3: BP = 0.0112 kPa/s



(d) Test 4: BP = 0.0220 kPa/s



(e) Test 5: BP = 0.0866 kPa/s



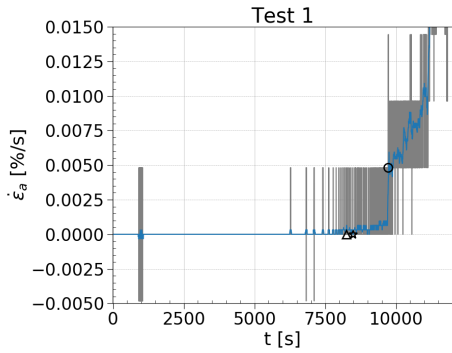
(f) Test 6: BP = 0.0866 kPa/s



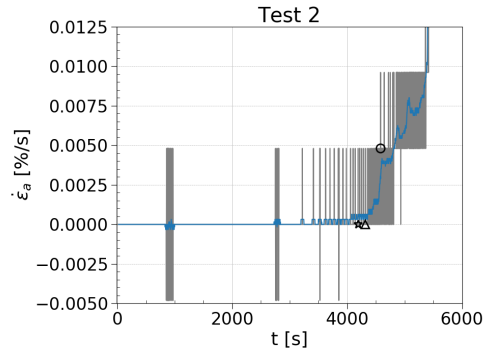
(g) Test 8: BP = 0.5069 kPa/s

Figure O.1: Instability at the end of the back pressure change triaxial tests

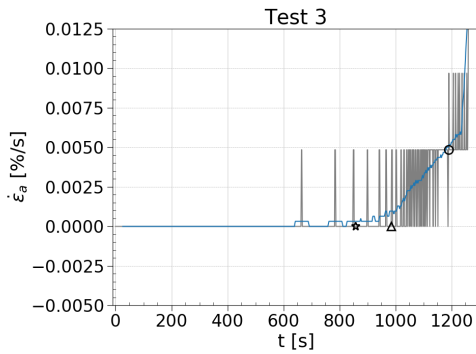
P | Zoomed on the axial strain results



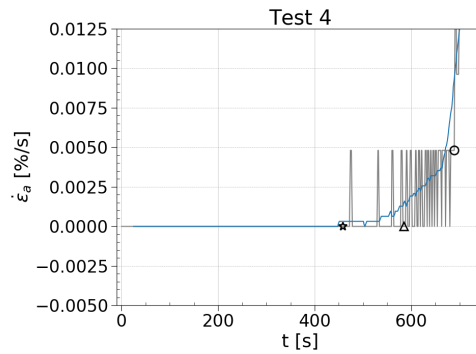
(a) Test 1: BP = 0.0014 kPa/s



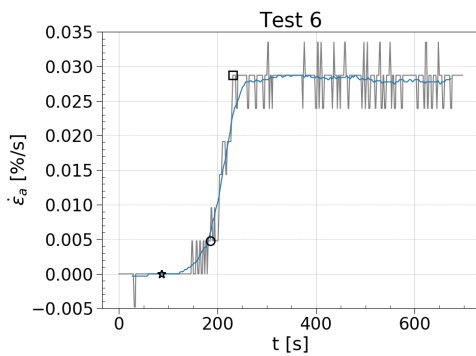
(b) Test 2: BP = 0.0030 kPa/s



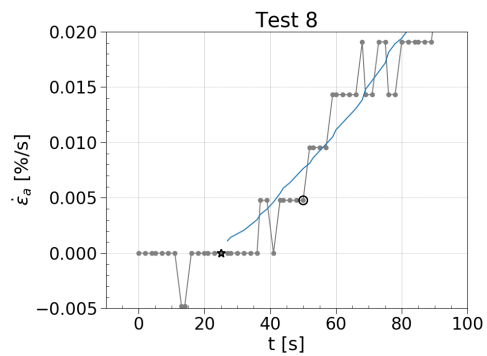
(c) Test 3: BP = 0.0112 kPa/s



(d) Test 4: BP = 0.0220 kPa/s



(e) Test 6: BP = 0.0866 kPa/s



(f) Test 8: BP = 0.5069 kPa/s

Figure P.1: Axial strain versus time with moving average in blue, zoomed on the start of decreasing deviatoric stress and first and first point of rapid increase